

https://dspace.org/

Bis(Indazole-imine) ligands for gold(III): towards new scaffolds for metal-based topoisomerase inhibitor

Moseki, Kebuile

2021

https://hdl.handle.net/10539/32469

Downloaded from a DSpace repository. https://dspace.org/

Bis(Indazole-imine) Ligands for Gold(III): Towards New Scaffolds for Metal-Based Topoisomerase Inhibitors

Submitted in fulfillment of the requirements for the degree of

Master of Science

By

Kebuile Moseki

BSc (Honours) (University of the Witwatersrand)



WITS
UNIVERSITY

December 2020

School of Chemistry

University of the Witwatersrand

Johannesburg

Declaration

I declare that this Dissertation is my own, unaided work. It is being submitted for the Degree of Master of Science at the University of the Witwatersrand, Johannesburg. It has not been submitted before for any degree or examination at any other University.

This Dissertation does not contain other persons' data, pictures, graphs, or other information unless specifically acknowledged as being sourced from other persons.

This Dissertation does not contain other persons' writing unless specifically acknowledged as being sourced from other researchers. Where other written sources have been quoted, then:

a) Their words have been re-written but the general information attributed to them has been referenced.

b) Where their exact words have been used, then their writing has been placed in italics and inside quotation marks and referenced.

This Dissertation does not contain text, graphics, or tables copied and pasted from the Internet unless specifically acknowledged, and the source being detailed in the Dissertation and the References section(s).

This Declaration is enforced for all research dissertations emanating from research conducted in the Bioinorganic Research Laboratory at the University of the Witwatersrand.

Signed: ____ 

Kebuile M. Moseki

On this _20_day of _July_2021 in_Springs

I hereby certify that this is correct.

Signed:  _____

Prof. Orde Q. Munro (Supervisor)

Acknowledgements

Firstly I would like to acknowledge my supervisor Prof. Orde Munro for his consistent guidance and unlimited support throughout my MSc studies. Prof has been nothing but the best! And I dearly thank him for that. His love and passion for his work made me desire to work hard and not to disappoint him. I truly appreciate the level of knowledge and wisdom that he carries and I pray that God continues to bless him. I also want to thank Prof Munro and the National Research Fund (NRF) for financial support.

I would also like to acknowledge the following individuals:

- Dr. Cathryn Slabber for her assistance with biochemical experiments and for making sure that the laboratory ran smoothly.
- Mr. Mark Blow for being the helping hand when I was clueless and also reassuring me that I could always go to him for help.
- Mr. Delbert Botes and Prof Munro for assisting me with single-crystal X-ray data collection.
- Dr. Angelique Blanckenberg who organized for me the TeamViewer software during the national COVID-19 lockdown so that I could access my work from campus while working from home.
- Wits Bioinorganic group as a whole.
- My friends, Masego, Dineo, and Tebogo for their support throughout my studies.
- Fortune Nhlanhla, a very special someone, for always being a shoulder to cry on.
- My family for their love and support.

Special Acknowledgements

I would like to extend my special acknowledgments to Dr. S. Saha who is supervised by Prof M. Kaur under the Cell Biology group at WITS; for his assistance with the cytotoxicity assay. I got the opportunity to work alongside Dr. Saha to learn and understand the MTT assay method. My biggest contribution was to prepare samples and solutions for the experiment. Without his assistance, this work would have not been possible. I, therefore, appreciate his consistent efforts and guidance.

Abbreviations

Arg	Arginine
ASN	Asparagine
ATP	Adenosine triphosphate
Au (III)	Au(III)
Au_2O_3	Gold(III) Oxide
$[Bu_4N][AuCl]$	Tetrabutylammonium Tetrachloroaurate(III)
$[Bu_4N]Cl$	Tetrabutylammonium Chloride
Cisplatin	Diamminedichloroplatinum(II)
Cl^-	Chloride ion
Co(II)	Cobalt(II)
CpG	Cytosine Phosphate Guanine
CPT	Camptothecin
CSD	Cambridge Structural Database
CTDNA	Calf Thymus Deoxyribonucleic Acid
DCM	Dichloromethane
DFT	Density Functional Theory
DMF	Dimethylformamide
DMSO	Dimethyl Sulfoxide
DNA	Deoxyribonucleic acid
DNMT	DNA methyltransferase
EB	Ethidium Bromide
E. coli	*Escherichia coli*
EDTA	Ethylenediamine Tetraacetic Acid
EMSA	Electrophoretic Mobility Shift Assay
FDA	Food and Drug Administration
Fe(III)	Iron(III)
FQ	Fluoroquinolones
FTIR	Fourier Transform Infrared
GGA	Generalized Gradient Approximation
Glu	Glutamine
Gyr A	Gyrase A
$H[AuCl_4]$	Hydrogen tetrachloroaurate(III)
HEK-293	Human Embryonic Kidney-293
HF	Hartree Fock

HOMO	Highest Occupied Molecular Orbital
HPLC	High-Performance Liquid Chromatography
HPV	Human Papilloma Virus
$K[AuCl_4]$	Potassium tetrachloroaurate(III)
LAG	Liquid assisted grinding
LDA	Local density approximation
LMCT	Ligand-to-Metal Charge Transfer
LUMO	Lowest Occupied Molecular Orbital
MDA-MB-231	M.D. Anderson Metastasis Breast cancer-231
MCF-7	Michigan Cancer Foundation-7
Mg (II)	Magnesium(II)
$MgSO_4$	Magnesium sulphate
Mn(II)	Manganese(II)
MO	Molecular Orbital
MTT	3-(4,5-dimethylthiazol-2-yl)-2,5-diphenyltetrazolium bromide
$Na[AuCl_4]$	Sodium tetrachloroaurate(III)
NCI	National Cancer institute
Ni(II)	Nickel(II)
NOC	Nicked open Circular
PBS	Phosphate-Buffered Saline
Pd(II)	Palladium(II)
NMR	Nuclear Magnetic Resonance
Pd(II)	Palladium(II)
Pt (II)	Platinum(II)
RMSD	Root-Mean-Square Deviation
SC	Supercoiled
TD-SCF	Time-Dependent Self-Consistent Field
TNBC	Triple-Negative Breast Cancer
Topo I/II	Topoisomerase I/II
Tyr	Tyrosine
UV	Ultra-violet
XC	Exchange correlation

Contents

Declaration 2

Acknowledgements 3

Abbreviations 4

Contents 6

List of Figures 10

List of Tables 15

Abstract 16

Chapter 1 18

Literature Review 18

1.1. General introduction 18

1.2. Cancer treatment 22

1.3. Drug resistance 24

1.4. Metallodrugs used for cancer treatment 25

1.5. Drug-resistant bacterial infections 27

1.6. DNA Topoisomerases 28

1.6.1. General introduction 28

1.6.2. DNA topoisomerase I 29

1.6.3. DNA topoisomerase II 31

1.7. Topoisomerase I and II inhibitors 32

1.7.1. Topoisomerase I inhibitors 33

1.7.2. Topoisomerase II inhibitors 36

1.7.3. Topoisomerase II catalytic inhibitors 37

1.8. Metallodrugs as topoisomerase inhibitors 38

1.9. AIM 40

1.10. Objectives 42

1.11. References 43

Chapter 2 47

Experimental Section 47
2.1. General Methods 47
2.1.1. Solvents and Reagents 47
2.1.2. Analytical techniques 47
2.1.2.1. Nuclear magnetic resonance (NMR) spectroscopy 47
2.1.2.2. Ultraviolet-visible (UV-vis) spectroscopy 47
2.1.2.3. Fourier-transform infrared (FTIR) spectroscopy 47
2.1.2.4. High-resolution mass spectroscopy (HRMS) 48
2.1.2.5. X-ray crystallography 48
2.1.3 DNA binding studies 48
2.1.3.1. Gel electrophoresis 48
2.1.3.2. Viscometry 49
2.1.4. Biological studies 49
2.1.4.1. Cell culturing 49
2.1.4.2. Sub-culturing of cells 49
2.1.4.3. Cell stocks 49
2.1.4.4. Revival of stocks 50
2.1.4.5. Cell counting with trypan blue exclusion assay 50
2.1.4.6. Cell plating 50
2.1.4.7. Growth inhibition with MTT assay 51
2.2. Synthesis and Characterization of Ligands 52
2.3. Synthesis of Metal Salt Precursor 56
2.4. Synthesis and Characterization of Metal Chelates 57
2.5. DFT simulations 60
2.6. References 60
Chapter 3 61
Synthesis and Spectroscopic Characterization 61
3.1. Synthesis 61
3.1.1. Synthesis of bis(indazole-imine) ligands 62
3.1.2. Metallation of ligands 64
3.2. Spectroscopic characterization 68

3.2.1. IR spectroscopy: Results and discussion 68

3.2.2. Results and discussion: UV-vis spectroscopy 71

3.2.3. NMR - Results and discussion 72

3.2.4. Mass spectroscopy of ligands and Au(III) chelates 77

3.3. References 79

Chapter 4 80

X-ray Crystallography and DFT Simulations 80

4.1. Introduction 80

4.2. X-ray crystallography of Au(III) chelates 80

4.2.1. X-ray crystallography of $[Au(PrIndz)]Cl\cdot 3H_2O$ and $[Au(PrIndz)][AuCl_4]\cdot CH_3CN$ 81

4.2.2. X-ray crystallography of $[Au(PrMe_2Indz)][PF_6]\cdot CH_3CN$ 84

4.2.3. X-ray crystallography of $[Au(PrOHIndz)]PF_6\cdot DMSO$ 86

4.3. Crystal structure analysis of $[BuN_4][AuCl_4]$ 88

4.4. Conclusion 89

4.5. Density Functional Theory (DFT) Simulations 90

4.5.1. Computational objectives 92

4.5.2. Computational studies of Au(III) chelates 92

4.5.2.1. DFT-calculated geometries 92

4.5.2.2. DFT-calculated IR spectra 95

4.5.2.3. DFT calculated electronic spectra 98

4.5.2.4. Results for NMR calculations 103

4.6. Conclusions 106

4.7. References 107

Chapter 5 108

Biological studies 108

5.1. Introduction 108

5.2. Electrophoretic Mobility Shift Assay (EMSA) 109

5.3. Titration absorbance spectroscopy 111

5.4. Viscometry 114

5.5. Whole-cell cytotoxicity 116

5.6. Conclusion 119

5.7. References 120

Chapter 6 122

Conclusions and Future Work 122

Appendices 126

Appendix A 126

Appendix B 129

Appendix C 130

Appendix D 131

Appendix E 133

Appendix F 136

List of Figures

Figure 1.1: Point mutation (a) on a nucleic acid sequence showing the substitution of thymine on the original sequence by cytosine, rendering a mutated sequence. Translocation mutation (b) demonstrating the swapping of DNA segments between chromosomes.[6] 19

Figure 1.2: Epigenetic changes illustrated. DNA methyltransferase (DNMT) transfers two methyl groups to CpG sites of separate DNA strands to form fully methylated double-stranded DNA.[7] 20

Figure 1.3: Chemical structures of platinum-based metallodrugs: cisplatin, carboplatin, oxaliplatin, nedaplatin, and lobaplatin.[16] 25

Figure 1.4: Chemical structure of auranofin.[18] 26

Figure 1.5: Crystal structure of *E.coli* DNA Topo I, showing different domains that it comprises of.[32] Reproduced from X-ray structure coordinates of Protein Data Bank (PDB) entry 1ECL. 30

Figure 1.6: Crystal structure of yeast DNA Topo II enzyme bound to the DNA.[38] Reproduced from X-ray structure coordinates of Protein Data Bank (PDB) entry 3FOE. 32

Figure 1.7: Å X-ray structure of Topo I-DNA ternary complex bound to topotecan. (a) shows the overall structure, topotecan (blue) is shown in space-filling mode bound into the intercalation binding pocket at the center of the DNA and protein, the DNA molecule is shown in white and the ribbon representation of a protein is shown in yellow. (b) the chemical structure of topotecan. (c) shows a close-up view of the drug in the enzyme's active site; grey bonds show the hydrophobic interaction, green bonds show the π-interactions between topotecan and DNA bases, hydrogen bonds are shown in blue.[42] Reproduced from X-ray structure coordinates of PDB entry 1T8I. 35

Figure 1.8: 2.16 Å crystal structure of etoposide-bound stabilized cleavage complex.[22] Reproduced from X-ray structure coordinates of PDB entry 3QX3. 37

Figure 1.9: Organic Topo I inhibitors (camptothecin, topotecan, and irinotecan) and Topo II inhibitors (etoposide, teniposide, aclarubicin, and sobuzoxane).[39] 38

Figure 1.10: Structures of known cytotoxic Au(III) chelates: a) auranofin[18], b_1) [Au(4-glucosyl-TPP)]Cl, b_2) [Au(TMPyP]Cl_5,[20] c) $AuCl_2(HL_4)$ amides[43], d) Au(III) macrocycles[29]. The latter two Au(III) systems are proven Topo I and Topo II inhibitors. 40

Figure 1.11: Chemical structures of novel bis(indazole-imine) ligands to be chelated to Au(III) ion in this project. 41

Figure 1.12: The Figure demonstrates a) the novel target Au(III) chelate and b) Au(III) macrocycle (a known cytotoxic Au(III) chelate). Based on the similarities in the directly-coordinated groups to Au(III) for the two classes of compound, we expect the target

compound to possibly interact with DNA through intercalative interaction and could potentially also catalytically inhibit Topo I. Part b) of the figure is taken from Ref. 29. 42

Figure 3.1: a) Photograph of the homogenous yellow powder formed after grinding the starting materials using a pestle and mortar. b) Photograph of the orange fiber-like crystals of one of the Au(III) bis(indazolide-imine) chelates in a crystallization tube. 65

Figure 3.2: a) Photograph of the fine orange crystalline powder of a typical [Au(L)][PF_6] salt, where L = bis(indazolide-imine), after recrystallization in acetonitrile. b) Photograph of a crystalline red powder of the propyl-bridged Au(III) chelate with the undesirable [$AuCl_4$]$^-$ counterion, [Au(PrIndz)][$AuCl_4$]. 66

Figure 3.3. Superimposed IR spectra of H_2PrMe_2Indz and [Au($PrMe_2Indz$)]PF_6 indicating their characteristic signals which prove their successful synthesis. 68

Figure 3.4: Superimposed IR spectra of $H_2PrOHIndz$ and [Au(PrOHIndz)]PF_6 indicating characteristic signals which prove their successful synthesis. 69

Figure 3.5: A pyrrole-type macrocyclic ligand and Au(III) chelate comparable to bis(indazole-imine) ligands and Au(III) chelates reported in this work.[6] 70

Figure 3.6: Electronic spectra of a) H_2PrMe_2Indz and b) [Au($PrMe_2Indz$)]PF_6 in 10% DMSO-water at 298 K. 71

Figure 3.7: Assigned ^{1}H NMR spectrum of H_2PrMe_2Indz in DMSO at 300 K. 74

Figure 3.8: Assigned ^{1}H NMR spectrum of [Au($PrMe_2Indz$)]PF_6 in DMSO at 300 K. 75

Figure 3.9: Assigned ^{13}C NMR spectrum of H_2prMe_2Indz in DMSO at 300 K. 76

Figure 3.10: Assigned ^{13}C NMR spectrum of [Au($PrMe_2Indz$)]PF_6 in DMSO at 300 K. ... 77

Figure 3.11: Mass spectrum of $H_2PrOHIndz$ showing its mass peak at 347.16 *m/z*. Another peak at 219.12 *m/z* represents the $C_{11}H_{14}N_4O$ fragment of $H_2PrOHIndz$. 78

Figure 3.12: Mass spectrum of [Au(PrOHIndz)]PF_6 showing its mass peak at 541.10 *m/z*. 78

Figure 4.1: Thermal ellipsoid view of the X-ray structure of [Au(PrIndz)]Cl·$3H_2O$ and [Au(PrIndz)][$AuCl_4$]·CH_3CN rendered at the 50% probability level. Hydrogen bonds, selected atom labels, and interaction distances (Å) are shown for [Au(PrIndz)]Cl·$3H_2O$. 82

Figure 4.2: View of the centrosymmetric π–π dimers formed by the cations in the triclinic X-ray structure of [Au(PrIndz)]Cl·$3H_2O$. The model is rendered in ball and stick format; solvate water molecules and chloride ions have been omitted for clarity. 83

Figure 4.3: Thermal ellipsoid view (50% probability surfaces) of the X-ray structure of [Au($PrMe_2Indz$)][PF_6]·CH_3CN showing the cation and closest positions for the anion and solvent molecule. Selected atoms have been labeled. Only the major component (ca.

60%) of the disordered hexafluorophosphate(V) ion is shown and all H atoms are drawn as spheres of an arbitrary radius. 84
Figure 4.4**:** View of the cation stack in the crystal structure of [Au(PrMe$_2$Indz)][PF_6]·CH_3CN with the symmetry-unique inter-planar spacings (Å) illustrated. 84
Figure 4.5: View of the short intermolecular contacts (Å) with a distance less than the sum of the van der Waals radii of the interacting atoms minus 0.10 Å ($d_{vdw} < \{r_1 + r_2\} - 0.1$).85
Figure 4.6: Labelled view of the X-ray structure of [Au(PrOHIndz)]PF_6·2DMSO. Thermal ellipsoids are rendered at the 30% probability level. Only the ordered DMSO molecule is shown and was included in the final model. 86
Figure 4.7: Illustration of the π-stacking between cations in the crystal lattice of [Au(PrOHIndz)]PF_6·2DMSO..... 87
Figure 4.8: X-ray crystal structure of [BuN_4][$AuCl_4$] analyzed at 173.15 K. The illustration on the left side shows unconventional C-H···Cl hydrogen bonds between the cation and the PF_6^- anion in the structure [$AuCl_4$]$^-$. 89
Figure 4.9: The least-squares fit for the DFT-calculated structure (blue) and the X-ray structure (orange) of [Au(PrMe$_2$Indz)]PF_6. The RMSD value is also indicated with the structure. 93
Figure 4.10: [Au(L1)]PF_6 ([12,13-dihydro-14H-6,9:17,20-diepimino[1,6]diazacyclo-heptadecino[12,13-β] quinoxalinato]gold(III) hexafluorophosphate(V).[7] 94
To verify that the geometry optimization outcome was a true minimum on the global potential energy surface, vibrational frequencies were computed. The calculated IR spectral frequencies were compared with the calculated IR spectral frequencies. Figure 4.11 below shows the superimposed calculated and experimental IR spectra for [Au(PrMe$_2$Indz)]PF_6 as a representative of the Au(III) chelates reported herein.. See Appendix E for the DFT-calculated IR spectrum of [Au(PrOHIndz)]PF_6. 95
96
Figure 4.11: Superimposition of DFT-calculated and experimental IR spectra. The calculated 96
IR spectrum has been scaled to match the experimental spectrum. The scale factor of 1 was used. 96
Figure 4.12: A plot showing the correlation between the experimental and DFT-calculated IR frequencies for [Au(PrMe$_2$Indz)]PF_6. 97
Figure 4.13: Superimposition of DFT-calculated (red) and experimental (black) UV-vis spectra for [Au(PrMe$_2$Indz)]PF_6 in DMSO. The spectra were normalized to an absorbance range of 0-1 before plotting. 99

Figure 4.14: Image displaying molecular orbitals involved in most of the electronic transitions of [Au(PrMe$_2$Indz)]PF$_6$. Only the LUMO+1 orbital has σ-symmetry, all the other orbitals are mostly π-symmetry. 100
Figure 4.15: The plot of DFT-calculated transitions for [Au(PrMe$_2$Ind)]PF$_6$. 103
Figure 4.16: Labeling scheme for [Au(PrMe$_2$Indz)]PF$_6$. 104
Figure 4.17: Plots showing a correlation between experimental and DFT-calculated chemical shifts for the H^1 NMR (a) and ^{13}C NMR spectra of [Au(PrMe$_2$Indz)]PF$_6$. 105
Figure 5.1: Electrophoretic mobility shift assay of a) [Au(PrMe$_2$Indz)]PF$_6$ and b) [Au(PrOHIndz)]PF$_6$ with pUC57 plasmid DNA. All gel electrophoresis experiments were carried out using hand-cast 1.25% agarose gels dissolved in 1x TAE buffer. 50 ng of DNA was added per lane and gels were run at a voltage of 65 V at 37 °C. Ethidium Bromide solution was used to stain the gels for 30 minutes. 110
Figure 5.2: Sequential absorption spectra of [Au(PrMe$_2$Indz)]PF$_6$ in the presence and absence of ctDNA. The experiment was performed in 0.100 M pH 7.0 TRIS-HCl Buffer with 10% DMSO at 37 °C. 111
Figure 5.3: Non-linear least-squares fit of the Hill function to the spectroscopic data at 333 nm for the titration of [Au(PrMe$_2$Indz)]PF$_6$ with ctDNA at 37 °C. 113
Figure 5.4: Viscosity plots showing the change in viscosity with increasing concentration of test compounds and controls. Viscosity is represented as a specific viscosity $((\eta - \eta_0/\eta_0)^{1/3})$. Data are shown for EB (well-known intercalator), Hoechst 33258 (well-known groove binder), and [Au(PrMe$_2$Indz)]PF$_6$ and [Au(PrOHIndz)]PF$_6$. 115
Figure 5.5: Plot of cell survival (%) as a function of drug/compound concentration measured via the MTT assay method. For each compound, data from two independent experiments are shown and each point represents the average measured from three independent cell colonies (wells). 117
Figure 6.1. Bis(indazole-imine) ligands and Au(III) chelates synthesized in this work. ... 122
Figure A1: ^{1}H NMR spectrum of H$_2$PrIndz. 126
Figure A2: ^{13}C NMR spectrum of H$_2$PrIndz. 126
Figure A3: ^{1}H NMR spectrum of H$_2$PrOHIndz. 127
Figure A4: ^{13}C NMR spectrum of H$_2$PrOHIndz. 127
Figure A5: ^{1}H NMR spectrum of [Au(PrOHIndz)]PF$_6$. 128
Figure A6: ^{13}C NMR spectrum of [Au(PrOHIndz)]PF$_6$. 128
Figure B1: Beer-Lambert law curves for H$_2$PrIndz at 281nm (right) and 300 nm (left). R^2 gives the correlation coefficient while the slope affords the molar absorptivity constant. 129

Figure B2: Beer-Lambert law curves for H_2PrMe_2Indz at 281nm (right) and 300 nm(left). R^2 gives the correlation coefficient while the slope affords the molar absorptivity constant. 129
Figure B3: Beer-Lambert law curves for $H_2BuIndz$ at 281 nm (right) and 300 nm (left). R^2 gives the correlation coefficient while the slope affords the molar absorptivity constant.129
Figure B4: Beer-Lambert law curves for H2PrOHIndz at 280 nm (right) and 300 nm (left). R^2 gives the correlation coefficient while the slope affords the molar absorptivity constant. 130
Figure C1: Mass spectrum of $H_2PrIndz$. 130
Figure C2: Mass spectrum of $H_2BuIndz$. 130
Figure C3: Mass spectrum of $H_2PrOHIndz$. 131
Figure D1: IR spectrum of $H_2PrIndz$. 131
Figure D2: IR spectrum of $H_2BuIndz$. 132
Figure E1: Image displaying molecular orbitals involved in most of the electronic transitions of [Au(PrOHIndz)]PF_6. 133
Figure E2: The least-square fit for the DFT-calculated structure (orange) and the X-ray structure (blue) of [Au(PrOHIndz)]PF_6. 134
Figure E3: DFT-calculated IR spectrum of [Au(PrOHIndz)]PF_6. 134
Figure E4: DFT-calculated ^{1}H NMR spectrum of [Au(PrOHIndz)]PF_6. 135
Figure E5: DFT-calculated UV-vis spectrum of [Au(PrOHIndz)]PF_6. 135
Figure F1: Sequential absorption spectra of [Au($PrMe_2Indz$)]PF_6 in the presence and absence of ctDNA. The experiment was performed in 0.100 M pH 7.0 TRIS-HCl Buffer with 10% DMSO at 37 °C. 136
Figure F2: Non-linear least-squares fit of the Hill function to the spectroscopic data at 333 nm for the titration of [Au(PrOHIndz)]PF_6 with ctDNA at 37 °C. 136

List of Tables

Table 1.1: Recent FDA-approved anticancer drugs.[12] 23

Table 3.1. NH and C=N stretching frequencies for bis(indazole-imine) ligands. 69

Table 3.2: C=N and C=C stretching frequencies of bis(indazole-imine) ligands and Au(III) chelates compared with data for macrocyclic bis(pyrrolide-imine) ligands and Au(III) chelates. 70

Table 3.3: Wavelengths and extinction coefficients for absorption band maxima of bis(indazole-imine) ligands and Au(III) chelates at maximum absorbance peaks. 72

Table 3.4: ^{1}H NMR chemical shifts (ppm) of H_2PrMe_2Indz and $[Au(PrMe_2Indz)]PF_6$ in .. 73

DMSO at 300 K..... 73

Table 3.5: ^{13}C NMR chemical shifts of H_2PrMe_2Indz and $[Au(PrMe_2Indz)]PF_6$ in DMSO at 300 K. 75

Table 4.1: Crystal data for bis(indazolide-imine) Au(III) chelates. 80

Table 4.2: Selected bond lengths and bond angles describing the coordination sphere of $[Au(PrIndz)]^+$ for $[Au(PrIndz)]Cl\cdot 3H_2O$. 83

Table 4.3: Selected bond lengths and bond angles of $[Au(PrMe_2Indz)][PF_6]\cdot CH_3CN$ representing its coordination sphere. 85

Table 4.4: Selected bond lengths and bond angles of $[Au(PrOHIndz)]PF_6$ describing its coordination sphere. 87

Table 4.5: Comparison between bond lengths and both angles of the DFT-calculated and X-ray structure of $[Au(PrMe_2Indz)]PF_6$. 94

Table 4.6: Comparison of the DFT-calculated geometry optimization data of $[Au(PrMe_2Indz)]PF_6$ with similar Au(III) chelate [Au(L1)] PF6.[7] 95

Table 4.7: Comparison of IR data between the DFT-calculated and X-ray structure of $[Au(PrMe_2Indz)]PF_6$. 97

Table 4.8: Comparison of the DFT-calculated IR vibrational frequencies $(cm-1)$ for $[Au(PrMe_2Indz)]PF_6$ and $[Au(L1)]PF_6$. 98

Table 4.9. The main DFT-calculated transitions and assignments for the cation of $[Au(PrMe_2Indz)]PF_6$ in a DMSO solvent continuum.* 102

Table 4.10: Experimental and DFT-calculated 1H and 13C NMR chemical shifts for $[Au(PrMe_2Indz)]PF_6$. 104

Table 5.1. The binding constants (K_a) of Au(III) chelates and Ru(II) complexes. 113

Table 5.2: Cytotoxicity data (IC_{50} values) for Au(III) chelates and cisplatin against MDA-MB 231, MCF-7, and HEK-239 cancer cell lines. Estimated standard uncertainties are given in parentheses. 118

Abstract

The purpose of this work was to synthesize and characterize several novel bis(indazole-imine) ligands suitable for chelating gold(III), thereby contributing to the development of a new library of square-planar Au(III) complexes with the potential ability to target DNA and consequently potential application as anticancer agents. Four bis(indazole-imine) ligands were synthesized and characterized by proton and carbon-13 NMR, FTIR, UV visible, and mass spectrometry.

The structures of the ligands possess two indazole rings connected by diamine bridges. The ligands, however, are varied structurally through changing the length of the diamine bridge and the substituent on the diamine bridge. The length of the diamine bridge was varied such that the first ligand had a propyl chain with a short notation: H_2PrMeIndz, the second ligand had a dimethyl group on the propyl chain and was notated H_2PrMe_2Indz, the third ligand had a hydroxy group (H_2PrOHIndz), while the fourth had a butyl chain (H_2BuIndz). Among these ligands, only the dimethyl and the hydroxy-bridged ligands (H_2PrMe_2Indz and H_2PrOHIndz) chelated successfully to the Au(III) metal ion forming square-planar Au(III) chelates: $[Au(PrMe_2Indz)]PF_6$ and $[Au(PrOHIndz)]PF_6$. These salts were also fully characterized by ^{1}H and ^{13}C NMR, UV-vis, FTIR and MS.

During metal coordination, the indazole NH acts as a proton donor and the imino nitrogen acts as a proton acceptor which results in deprotonation of two NH protons forming +1 charged chelates of the general type [Au(L)]+. The two successfully synthsised Au(III) chelates ($[Au(PrMe_2Indz)]PF_6$ and $[Au(PrOHIndz)]PF_6$) were studied by X-ray crystallography. Both chelates had a d^8 electronic configuration and a square-planar geometry. The average Au-$N_{indazole}$ and Au-N_{imine} bond lengths were 1.99 Å and 2.01 Å, respectively and the average $N_{indazole}$-Au-$N_{indazole}$ and N_{imine}-Au-N_{imine} angles measured 90.01° and 89.73°, respectively.

Density functional theory (DFT) simulations were performed. The simulations were carried out for geometry optimizations, electronic transitions, NMR spectral data, as well as vibrational spectra. Overall, the DFT simulations produced accurate results that correlated well with experimental results. Geometry optimization data revealed a good correlation between the DFT-calculated and the X-ray structure with low RMSD values (when compared with the X-ray structures) indicating that the DFT calculations were accurate.

A comparison between the experimental and the calculated UV-vis data showed that DFT calculations consistently overestimated the band energies. However, there was still a good correlation between the intensities and the frequencies of the simulated and experimental spectra. The proton and carbon-13 NMR shielding tensors were calculated and the chemical shifts were compared to the experimental chemical shifts. In most cases, the calculated chemical shifts were overestimated with slight percentage differences for both proton and carbon-13 NMR.

Three DNA binding studies, namely gel electrophoresis, viscometry, and UV-vis absorption, were conducted to determine the binding mode of the Au(III) chelates. Gel electrophoresis and UV-vis absorption studies were consistent with each other as they both suggested a possibility of two binding modes which are intercalation and groove binding. Viscosity measurements, however, suggested intercalation as the main binding mode.

The Au(III) chelates were screened against two human breast cancer cell lines, MDA-MB-231 and MCF-7, and one normal human cell line, HEK-293. [Au($PrMe_2$Indz)]PF_6 proved to be more selective towards the two breast cancer cell lines compared with [Au(PrOHIndz)]PF_6. [Au(PrOHIndz)]PF_6, however, displayed greater cytotoxicity than cisplatin against both breast cancer cell lines.

Chapter 1

Literature Review

1.1. General introduction

Mammalian cells operate by a delicate molecular network that modulates important cellular processes such as cell differentiation, cell death, and cell proliferation. Interference with this network may transform normal cells into cancerous cells. Cancer is, therefore, a group of related diseases distinguished by uncontrolled cell division, cell growth, and the spread of a mass of cells forming a principal tumor that invades and affects nearby tissues.[1] Through metastasis, cancer cells travel and affect other regions of the body. Metastatic cancer contributes 90% of cancer mortality worldwide.[1] Cancer remains a life-threatening disease, with 13% of global death, mostly influenced by aging in most developed countries.[1] Theoretically, whilst cancer can arise in persons of every age, cancer cases and deaths most commonly occur in aging individuals, especially persons older than 65 years. This is due to factors such as accumulation of mutations, long term exposure to mutagens and carcinogens as well as long lifespan.[2]

The human body consists of trillions of cells which makes it likely for cancer to begin anywhere in the body.[3] At their normal states, cells grow and divide to make new cells required by the body. At certain stages, cells grow old or become damaged leading to cell death and new cells replacing them. The development of cancer, however, makes this process abnormal such that old and damaged cells survive when they are supposed to die and more cells arise when they are not required. Additional cells grow uncontrollably to form a tumor (mass of cells). As the tumor grows bigger, cancer cells free of the solid tumor body travel through blood vessels or lymph systems to form new tumors in other parts of the body.[3] Such tumors are described as malignant. In contrast to a malignant tumor, benign tumors do not invade adjacent tissues; this makes it easier for them to be removed and not grow back.[3]

Cancer is generally caused by certain alterations to the genetic material; these alterations can be internal, external, or inherited. Internal factors include genetic mutations, epigenetics factors, and addition or loss of DNA.[4]

Genetic mutation can occur by point mutation or translocation mutation. In point mutation (Figure 1.1a) one DNA base is changed thus changing the codon that causes the incorporation of an incorrect amino acid into a growing protein chain. This may result in cancer if the intended protein partakes in cell proliferation like a tumor suppressor protein.[4] In translocation mutation (Figure 1.1b), DNA segments may be swapped between chromosomes producing a new protein from fusion or loss of DNA sequences leading to loss of proteins (proto-oncogenes) corresponding to the original DNA sequences which may result in tumorigenesis. Addition and loss of genetic material may occur during replication and repair, whereby a wrong DNA base is accidentally added or removed from a DNA sequence.[4] The effect of this mutation is similar to that of point mutation as it can completely change the codon reading frame thus producing a defective protein that is going to participate in the control of cell growth.[4,5]

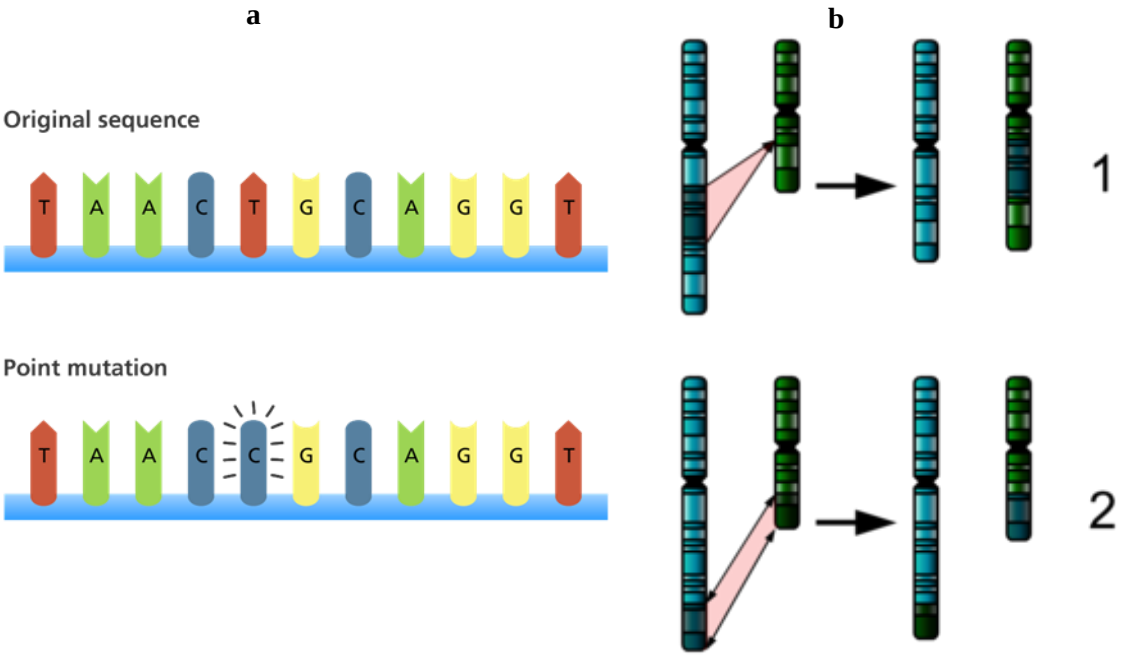

Figure 1.1: Point mutation (a) on a nucleic acid sequence showing the substitution of thymine on the original sequence by cytosine, rendering a mutated sequence. Translocation mutation (b) demonstrating the swapping of DNA segments between chromosomes.[6]

Epigenetic changes are mechanisms that modulate gene expression without changing the DNA sequence. Epigenetic information gives instructions on when, where, and how the genetic information should be utilized; it is channelled in the cell through methylation of the C5 region of pyrimidine cytosine of cytosine phosphate guanine (CpG) dinucleotides in the gene promoter. This methylation involves the transfer of two methyl groups to separate DNA strands to form fully methylated double-stranded DNA as illustrated in Figure 1.2.[4]

Changes in gene expression are triggered by the interaction of control proteins (e.g. methyl-CpG binding protein 2) with methylated regions on the genes. Processes triggered by epigenetic modifications include DNA repair, transcriptional expression, chromatin regulation, X-chromosome inactivation, imprinting, and genomic stability.[4,5]

Cancer cells are characterized by modified methylation patterns whereby hypomethylation and hypermethylation (region-specific) tend to be consistent in almost all cancer cell lines. When hypermethylation occurs within a tumor suppressor gene promoter, gene expression may be suppressed thus rendering the cell growth advantage corresponding to that of mutations and deletions. Contrarily, overexpression and tumorigenesis may come about from extensive hypomethylation within the promoter of an oncogene.[4,6] As this area is advancing in research more gene types including viral genes associated with tumor oncogenes and tumor suppressor genes are believed to be regulated by epigenetic information.[4,5]

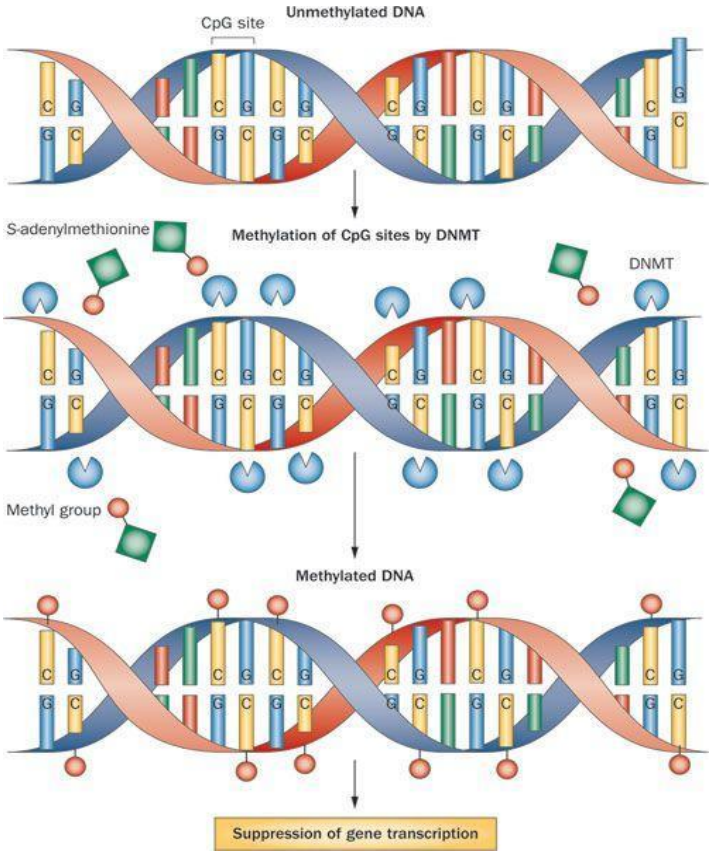

Figure 1.2: Epigenetic changes illustrated. DNA methyltransferase (DNMT) transfers two methyl groups to CpG sites of separate DNA strands to form fully methylated double-stranded DNA.[7]

External factors that may cause cancer include viruses, bacterial infection, chemicals, radioactivity as well as electromagnetic radiation. The association between viruses and cancer was first discovered in 1911 by Peyton Rous after he clearly illustrated that the filtrate from cells which only contained the *Rous Sarcoma virus* could transmit cancer from one bird to another. Since then, many different types of viruses have been associated with many cancer types.[4] The most common examples being human papillomavirus (HPV) which is linked to cervical cancer and Epstein-Barr virus linked to Burkitt's lymphoma.[4,8]

The bacterial infection that is linked to cancer includes the *Helicobacter pyroli* strain of bacteria, which finds its habitat in some individual's stomachs and eventually causes peptic ulcers. This bacterial infection is also linked to high risks of stomach cancer development. The mechanism by which this bacterium causes cancer remains unclear. The use of antibiotic therapy kills the infection and reduces the risk of cancer.[4,8,9]

Chemicals that cause cancer are found in the environment, diet occupation, and lifestyle. For example, cigarette smoke is associated with lung cancer, polycyclic aromatic hydrocarbons, on the other hand, are associated with colon cancer, and are found in overly cooked/burned food.[4,8] Preservatives used in meat and fish such as nitrites and nitrates may become carcinogenic by forming amines after degradation by bacteria in the stomach; these carcinogens are known as *aflatoxin* and are also found in low concentration in peanut butter due to fungus that infects peanuts during farming.[4] Other organic cancer-causing agents such as tarry deposits from coal fires can get into contact with the skin thus causing cancer over time.[4] More recently it was discovered that vinyl chloride used in the plastic industry is responsible for angiosarcoma of the liver. Some cancer-causing inorganic compounds include minerals and dust such as asbestos which has been linked to peritoneal and pleural cancers resulting from physical damage to chromosomes.[4]

The association between cancer and radioactivity became clear after World War II in Japan, 1945, after the atomic bomb explosions in Hiroshima and Nagasaki. The accident caused widespread contamination of the food chain and led to a variety of different cancers in populations exposed to the radiation.[4] Exposure of DNA molecules to α or β particles and γ- or X-rays may damage DNA through fragmentation by forming free radicals.[10] It has also been hypothesized that children residing near the power station stand a higher risk of suffering from a brain tumor and leukemia.[4]

Furthermore, it has also been reported that the accumulation of radon gas (a radioactive gas) from granite can endanger the lives of people living in houses built from granite material. When inhaled, radon gas invades the bloodstream and transports radiation to all the tissues.[4,8] So far, the types of electromagnetic radiation that have been well observed to cause tumourigenesis are those with greater energy and frequency in the electromagnetic spectrum such as X-rays, γ-rays as well as ultraviolet (UV) radiation. Radio waves and microwaves have recently been thought to have the potential to cause cancer.[4,10]

1.2. Cancer treatment

This section gives an overview of cancer and how it occurs from different factors human beings are exposed to. Different treatment options have been implemented to combat cancer. These treatments are prescribed to patients depending on the type of cancer they have and its stage of advancement.

Several types of cancer treatment available include surgery, radioactivity, chemotherapy, hormonal therapy, and other newer methods such as targeted therapy and immunological therapy. Treatments can be used singly or in combination depending on the condition of the patient.[3] Radiotherapy is the most common cancer treatment type used; it focuses on local body areas instead of treating the whole body, to avoid harming too many healthy cells. It involves the use of high-frequency X-rays to shrink and kill cancer cells at their early development stage and also stops them from regrowing. The mechanism involves breaking the DNA molecules within cells eventually causing cell death.[3,11] Radiotherapy treatment for one cancer, however, can also cause second cancer at a later stage. This is one disadvantage and the long-term side effect of this kind of treatment. The effect however differs for everyone and depending on the amount of radiation used and the area treated, some people may have high risk whereas others may have less severe risk. Another type of radiation treatment uses radioactive substances that are administrated through the mouth or veins. These substances travel throughout the body and collect at the side of the tumor to destroy cells.[3]

Although surgery is a cancer treatment method, it can also be used to diagnose and prevent cancer. This treatment type works by surgically removing small localized tumors; complex surgeries, which involve removing large tumors from the body, however, complications may arise because the more complex the surgery the higher risks of side effects.[11] Supplementary treatments such as chemotherapy and radiotherapy can be used in combination with surgery to completely kill the tumor.[11]

Chemotherapy means using chemicals to treat disease, it is the treatment of interest in this project and a well-known common treatment type used to kill cancer cells.[3] Unlike other treatment types, chemotherapy works throughout the body even away from the actual tumor; in this way, it can simply destroy cancer or limit its growth. Its use after surgery and radiotherapy minimizes the chances of cancer coming back.[11] Chemotherapy involves a variety of anticancer drugs and just like other treatment methods, anticancer drugs may have undesired side effects such as damage to normal fast-growing cells, as they have characteristics of cancer cells.

Normal tissues that are likely to be affected include hair follicles, bone marrow cells as well as cells in the mouth, reproductive system, and digestive system.[11] Hence worldwide there is increasing research interest into new anticancer drugs with reduced side effects and increased activity. Over the past years, a large number of compounds have been investigated in laboratories worldwide and have shown impressive anticancer activity. Newer drugs, however, tend to have more advantages than old ones due to improved properties. Table 1.1 shows recent FDA (Food and Drug Administration) approved drugs, year of approval as well as their biological targets.[12]

Table 1.1: Recent FDA-approved anticancer drugs.[12]

List of newly approved drugs and their targets		
Drug	**Year of approval**	**Biological target**
Crizotinib	2011	ALK; MET
Ipilimumab	2011	CTLA4
Ruxolitinib phosphate	2011	JAK1;JAK2
Vandetanib	2011	EGFR; PTK6; TEK; VEGFA
Vemurafenib	2011	BRAF
Pertuzumab	2012	ERBB2
Axitinib	2012	FLT1; FLT4; KDR
Bosutinib	2012	BCR-ABL
Cabozantinib	2012	KDR;MET;RET
Carfilzomib	2012	PSMB1; PSMB10; PSMB2; PSMB5; PSMB8; PSMB9
Enzalutamide	2012	AR
Ponatinib hydrochloride	2012	BCR-ABL
Regorafenib	2012	RET; FLT1; KDR; FLT4; KIT; PDGFRA; PDGFRB; FGFR1; FGFR2; TEK; DDR2; NTRK1; EPHA2; RAF1; BRAF; MAPK11; FRK; ABL1
Vismodegib	2012	SMO
Ziv-aflibercept	2012	PGF; VEGFA; VEGFB
Dabrafenib	2013	BRAF; LIMK1, NEK11; RAF1; SIK1
Trametinib	2013	MAP2K1; MAP2K2
Obinutuzumab	2013	MS4A1
Ado-tratuzumab emtansine	2013	ERBB2
Afatinib	2013	EGFR; ERBB2; ERBB4;
Ibrutinib	2013	BTK
Pomalidomide	2013	CRBN
Idelalisib	2014	PIK3CD
Belinostat	2014	HDAC1; HDAC2; HDAC3; HDAC6
Ceritinib	2014	ALK
Pembrolizumab	2014	PDCD1
Ramucirumab	2014	KDR
Lanreotide	2014	SSTR2; SSTR5
Blinatumomab	2014	CD19; CD3D
Nivolumab	2014	PDCD1
Olaparib	2014	PARP1; PARP2; PARP3

Although the ideal characteristics of anti-cancer drugs are selectivity and cytotoxicity to cancer cells. Cancer cells may develop resistance towards anticancer drugs over time and become less effective. This is one of the challenges faced by most anti-cancer drugs. The following section elaborates more on drug resistance and its cause; knowledge in this concept could serve as a crucial step to finding new drugs with a different mechanism of action from the current ones.

1.3. Drug resistance

Drug resistance is a tolerance of diseases to pharmaceutical treatment.[13] It was first discovered when certain bacteria exhibited resistance to antibiotics; later the same kind of resistance was observed in cancer. Cancer can be fairly treated using traditional cancer therapies (chemotherapy, radiotherapy, surgery, radioactivity, etc.). However, over time it develops resistance to treatment thus demanding advancement of research and development of new treatment.[13] Drug resistance is considered to be the key cause of cancer treatment failure and can occur either intrinsically or during treatment.[14]

Drug inactivation is one of the causes of drug resistance. This concept stems from the fact that many cancer drugs need to undergo a series of activation to render their effect.[14] Drug inactivation processes involve a series of mechanisms during which the drug interacts with different molecules and proteins in vivo. As a result of these interactions, the drug can be permanently altered, degraded, or even complexed to other compounds leading to its inactivation which in turn exerts resistance.[14]

Drug resistance can also occur through the alteration of a drug target. Every drug has a specific molecular target in vivo, and alterations (mutations and modification of the expression level) to this target can lead to resistance. One example is observed in anticancer drugs that specifically target topoisomerase II (Topo II).[13] This protein functions to remove DNA supercoils and tangles during DNA synthesis; whereby the DNA forms a transient complex with it. To stop the synthesis, anticancer drugs stabilize the DNA-protein complex thus damaging DNA and terminating DNA synthesis. For instance, a mutation in the Topo II gene results in certain cell lines becoming resistant to it.[13] In addition to these causes, other mechanisms such as drug efflux, decrease influx, cell death inhibition, and altered target expression has also been reported to cause drug resistance.[13,14]

1.4. Metallodrugs used for cancer treatment

Medicinal chemistry is a growing field of research in terms of the development of metal-based compounds used as drugs. Interest in metal-based compounds as anticancer drugs stems from their wide range of coordination numbers, geometries, and kinetic properties which render them characteristics of a drug that none of the organic compounds possess.[15] The successful discovery of cisplatin was the first introduction of metallodrugs into cancer chemotherapy, and this triggered massive interest in investigating other metallodrugs as anticancer drugs.

Cisplatin (Figure 1.3) uses the Pt(II) cation to covalently bind to deoxyribonucleic acid (DNA) at the N-7 of either adenine (A) or guanine (G) in the GG and AG DNA sequence to form cross-links. It is the cellular pathways activated through cisplatin binding and the adducts between cisplatin and DNA that result in transcription inhibition, replication arrest, cell-cycle arrest, and eventually apoptosis.[16] Cisplatin, however, regardless of its chemotherapeutic activity, caused undesired side effects in patients leading to second-generation platinum drugs: carboplatin, oxaliplatin, nedaplatin, and lobaplatin (shown in Figure 1.3) were designed to reduce the drawbacks of cisplatin. The chelate effect of the five and six-membered rings was intended to reduce cytotoxicity and chemical reactivity.[16]

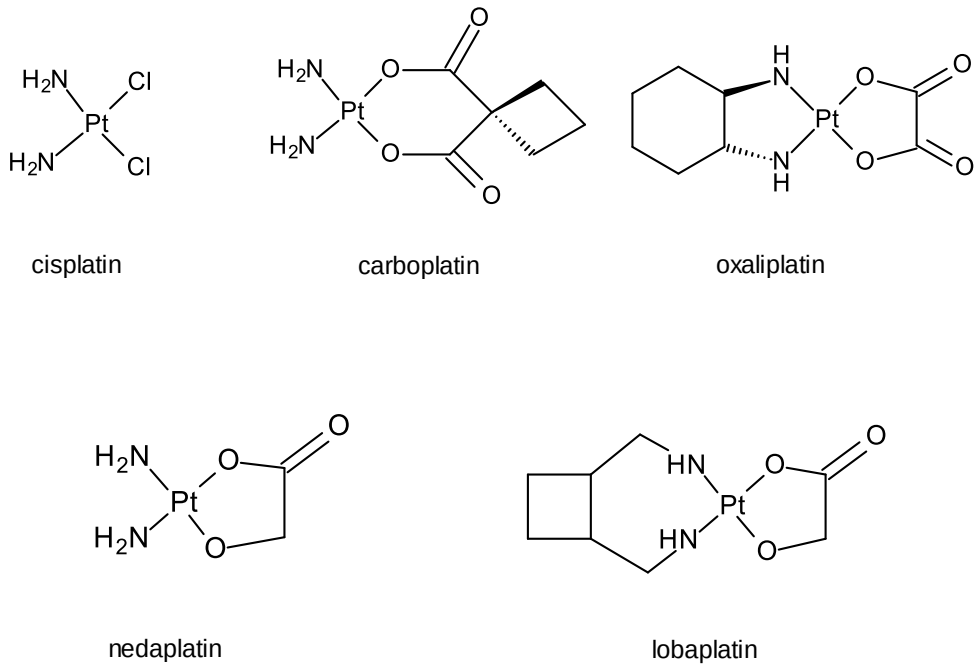

Figure 1.3: Chemical structures of platinum-based metallodrugs: cisplatin, carboplatin, oxaliplatin, nedaplatin, and lobaplatin.[16]

Although these drugs are efficient as chemotherapeutics, just like cisplatin, they also left patients with unpleasant side effects such as ototoxicity, abdomen pains, nausea, diarrhea, and neuron muscular problems. In addition, tumor cells tend to develop or acquire resistance against them thus limiting their clinical use.[15,16] The negative effects of platinum-based compounds stimulated a search into non-platinum compounds with reduced toxicity, high efficiency, and improved selectivity towards cancer cells.[17] Non-platinum compounds such as gold, iron, and cobalt-based compounds have undergone preclinical tests for which they produced promising results.[17] Hence there is a growing interest in exploring a range of non-platinum-based compounds for anticancer treatment.

Research into gold-based drugs which are of interest in this research project was triggered by the discovery of a gold-based drug, auranofin (Figure 1.4), in the mid-1980s.[18] It was used to treat rheumatoid arthritis and also showed cytotoxic effects on various cancer cell lines.
Later it was discovered that Au(III) complexes exhibit properties similar to cisplatin such as isoelectric and isostructural properties as well as the d^8 metal center.[18]

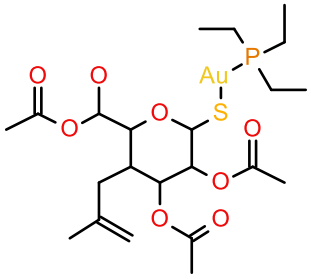

Auranofin

Figure 1.4: Chemical structure of auranofin.[18]

Although Au(III) complexes proved to be less effective than cisplatin in inhibiting cancer cells, they also demonstrated instability under physiological conditions (with other ligands) due to high redox potential which forced them to reduce to Au(I).[19,20] To prevent reduction, Au(III) complexes were chelated with σ-donor ligands which rendered them greater stability thus enabling them to be used as chemotherapeutics.[21] Consequently varieties of ligands were explored with Au(III) complexes, and are considered more attractive as they can stabilize metal centers and can also undergo π-π interactions with the DNA.[22]

In the literature, only a few cytotoxic Au(III) complexes have been proven to exhibit anticancer activity as well as good solubility and stability. Such complexes include: $[Au^{III}(damamp)Cl_2]$(dmamp = 2-(dimethylaminomethyl)phenyl, $[Au^{III}(DMDT)x_2]$ and $[Au^{III}(ESDT)x_2]$ (DMDT, N,N-dimethyldithiocarbamate, ESDT, esthylsarcosinedithiocarbamate, X = Cl or Br), $[Au^{III}m(C^{\wedge}N^{\wedge}C)_mL]^{n+}$ (m = 1-3, n = 0-3; $HC^{\wedge}N^{\wedge}CH$ = 2,6-diphenylpyridine), $[Au^{III}(bipy^c\text{-}H)(OH)[PF_6]$ [$bipy^c$-H, deprotonated 6-(1,1-dimethyl-benzyl)-2-2-bipyridine] and the $[Au^{III}(Por)]^+$ complexes (Por = porphrynpyridine) and $[Au(Por)]^+$ (Por = porphyrinato ligand).[20] Notwithstanding that, none of the non-platinum compounds has been approved for clinical use.[20,23]

1.5. Drug-resistant bacterial infections

Antibiotics play a very important role as medicine, such that they treat infections thus resulting in a drop in mortality and disease rate. Recently, relatively few new antibacterial compounds have reached clinical use while there is an increase in microbial resistance towards current antibacterial agents.[24] This is brought about challenges in the discovery of new antibacterial compounds. Application of traditional anti-bacterial agents (penicillin, cephalosporins, sulfonamides, tetracyclines) is limited by the increase in drug resistance by bacterial cells thus making infections untreatable, consequently prompting bacterial resistance which is increasingly becoming a public health threat worldwide.[24,25]

Most bacterial pathogens have become resistant to drugs, for example, two gram-negative strains of bacteria including *Acinetobacter baumannii* and *Pseudomonas aeruginosa* have become widespread in hospitals and even worse *Staphylococcus aureus* has become resistant to their traditional drug of last resort (vancomycin).[26]

In an attempt to solve this problem, programs such as New Drugs for Bad Bugs have been established to fight antimicrobial resistance.[24] Such programs involve multiple collaborative projects including academic partners as well as pharmaceutical industries to speed up the process of finding new antibacterial agents for bacterial infection resistance. So far, the only clinically approved antibiotics target is the bacterial type II topoisomerases. These enzymes facilitate genome segregation and DNA transcription in bacterial cells and are mainly targeted by an antibacterial drug called fluoroquinolones (FQs).[24]

FQs function by intercalating the DNA at two nicked sites with two molecules on either side of the doubly-nicked DNA four bases away from each other. This interaction converts the enzyme into a damaging agent by stabilizing the cleavage complex.[24]

Application of FQs is limited by the development of resistance by bacterial cells conferred commonly by a mutation in the protein target molecule. This has prompted calls for a new class of compounds to be synthesized to overcome resistance.[24] Metallodrugs such as bismuth-based compounds have been used together with antibiotics in the treatment of *Helicobacter pylori (H. pylori*) bacterial infection which can infect almost half of the population worldwide. Bacterial resistance that occurs during this treatment is suggested to occur due to antibiotic-resistant and not due to the bismuth compounds. This implies that metallodrugs have great potential to overcome bacterial resistance. *E. coli* strain has also been treated using ruthenium(II) complexes.[27]

1.6. DNA Topoisomerases

1.6.1. General introduction

DNA topoisomerases are key enzymes regulating DNA topology within the cell; this is because a typical DNA molecule (about 2 m long) is tightly packed into compact states to fit into a 6 μm diameter cell. During packing, DNA is wrapped around histone proteins to form highly condensed structures that are difficult to access during cellular processes (DNA replication and DNA transcription). DNA topoisomerases are therefore crucial in controlling DNA topology.[28]

Inhibition of DNA topoisomerases in cancer cells suppresses tumor growth; in a bacterial cell, it kills or inhibits their growth.[27] Topoisomerases are, therefore, considered the main targets for anticancer and antibacterial drugs in medicinal chemistry.[29] The first DNA proteins to be discovered were the omega protein (ω protein) and the swivelase protein; these proteins were noticed by their DNA relaxing activity.[30] The ω protein was discovered during the study of supercoiling of *Escherichia coli* (*E. coli*) in 1971.[30]

It was found to be responsible for relaxing negative supercoils. The swivelase protein, however, could relax both negative and positive supercoils. The study of these proteins established a clear understanding of the mechanism of action of proteins called topoisomerases at a later stage. Topoisomerases change the linking number of a closed DNA duplex thus changing its topology. They do this by introducing transient nick(s) in almost one of the two DNA strands which are ultimately ligated.[30]

In fact, DNA ligase requires energy to form new covalent bonds. Nonetheless, swivelase and ω protein perform ATP independent ligation. They both introduce transient single-strand breaks on the DNA strand thus storing the energy to be used later to form bonds (ligase activity).

This early understanding assisted in distinguishing the difference in two classes of DNA topoisomerase I; type IA (ω protein), type IB (swivelase). The basic mechanism revealed in swivelase and ω protein turned out to be common for all topoisomerases.[30]

Topoisomerases are classified into two broad classes: topoisomerase I and topoisomerase II (Topo I and Topo II) this is by the number of DNA strands they cleave during their activities. Topo I enzymes cleave one DNA strand while Topo II enzymes cleave two DNA strands. The two classes of topoisomerase are further divided into subclasses; Topo I have subclass IA and IB found in prokaryotic and eukaryotic cells, respectively. Topo II, however, incorporates the eukaryotic analogs (DNA Topo II) and the prokaryotic analog (DNA gyrase).[30]

The most common characteristic shared among DNA topoisomerases is the mechanistic reaction which involves tyrosine residues of the enzymes undergoing nucleophilic reaction on the DNA phosphodiester bond-forming covalent linkages between the DNA and the enzyme. Tyrosine residue forms the covalent bridge at the 3'-hydroxyl end of the open DNA for Topo I enzymes and at the 5'-hydroxyl end of the open DNA for other topoisomerases.[30]

1.6.2. DNA topoisomerase I

E. coli Topo I enzymes (type IA) were the first to be discovered, they are monomeric in structure and can resolve negative supercoils to change the linking number by a factor of 1. Moreover, they only require magnesium ion to perform their function. Overall, the structure comprises four domains as shown in Figure 1.5 below.[31] The domains encircle a large cavity designed to fit double-stranded β-form DNA. Perpendicular to the large cavity runs a cleft leading to the smaller cavity parallel to a large cavity.

The enzyme's DNA binding site can be determined by the location of the catalytic residue which is found within the C-terminal domain located on the other side of the protein.[31] The DNA molecule enters the enzyme through domain I before it progresses to domain IV, it then goes to domain II and III and eventually returns to domain II ending with domain IV. The contacts between domains I, III, and IV are noncovalent.[31]

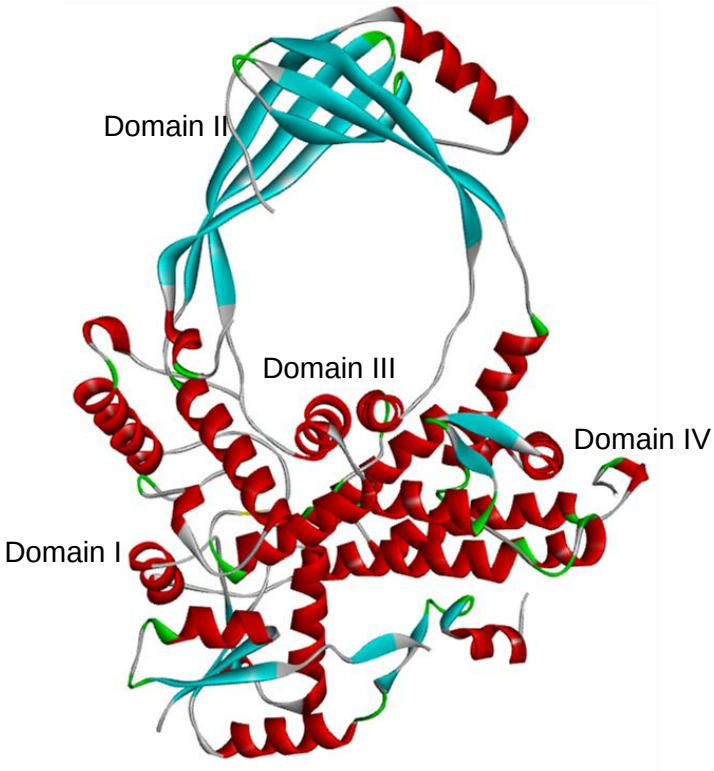

Figure 1.5: Crystal structure of *E.coli* DNA Topo I, showing different domains that it comprises of.[32] Reproduced from X-ray structure coordinates of Protein Data Bank (PDB) entry 1ECL.

Topo I operates through a single-strand passage mechanism. The catalytic tyrosine residue of the enzyme is hidden between domain I and II which makes it inaccessible to the DNA substrate. The enzyme is then obliged to undergo conformational changes to expose catalytic tyrosine residue for nucleophilic attack on the DNA.[31] These changes do not need any factor other than a divalent cation; they are therefore thought to be due to DNA contacts with the enzyme. The structure of type 1B Topo 1 (found in humans), however, has been reported to operate through the swivel mechanism also called controlled rotation instead of strand passage, during which the 5' hydroxyl end swivels around an intact strand and the DNA relaxes. This reaction does not require ATP hydrolysis or the presence of the Mg^{2+} divalent ion.[30,33]

1.6.3. DNA topoisomerase II

Topo II enzymes are capable of catalyzing several ATP-dependent reactions including relaxation of negative and positive DNA supercoils, negative supercoils of DNA, knotting and unknotting of DNA as well as catenation and decatenation of circular DNA.[34] Although the majority of Topo II enzymes prefer DNA relaxation and decatenation reactions, DNA gyrase is the only Topo II enzyme that can catalyze ATP-dependent negative supercoiling of its DNA substrate.[34] Topo II enzymes share most features except for the differences in the terminal domain.[34]

DNA gyrase was discovered in an *E. coli* extract by Howard Nash and Martin Gellert.[34] It is a heterotetrameric enzyme made up of two different subunits, DNA gyrase A protein (Gyr A) and DNA gyrase B protein (Gyr B). It has an ATP-dependent activity and operates by introducing negative supercoils to a relaxed or positively supercoiled DNA molecule.[34,35] Eukaryotic Topo II, however, is homodimeric such that its monomer is the size of an A and B subunits of gyrase enzyme fused. Their N-terminus is homologous to the B subunit and the C terminus is similar to the B subunit.[34]

As examples of Topo II enzymes, crystal structures of yeast DNA topoisomerase (Figure 1.6) and DNA gyrase have been solved and are homologous to each other. They both exhibit a cavity large enough to fit double-stranded DNA. The two structures are reported to show a high level of similarity in their secondary and tertiary structure and the difference is manifested in their quaternary structures.[30]

The catalytic mechanism of type II topoisomerase involves a two-gate mechanism where the enzyme is bound to two DNA segments: the gate segment (G-segment) where the break is formed and the transport segment (T-segment) that passes through the break. These enzymes are homodimeric and require both ATP and divalent cations (Mg^{2+}) to exhibit their full functions.[36] Their catalytic action begins with the DNA substrate recognizing the enzyme. The enzyme then binds to two DNA strands inducing ATP binding, which forms an equilibrium between cleavage and religation reactions on the G-segment.[37] This permits passage of the T-segment through the DNA gate to the C-terminal where it gets released. Strand religation and ATP hydrolysis then follow thus releasing the enzyme for another cycle of catalysis.

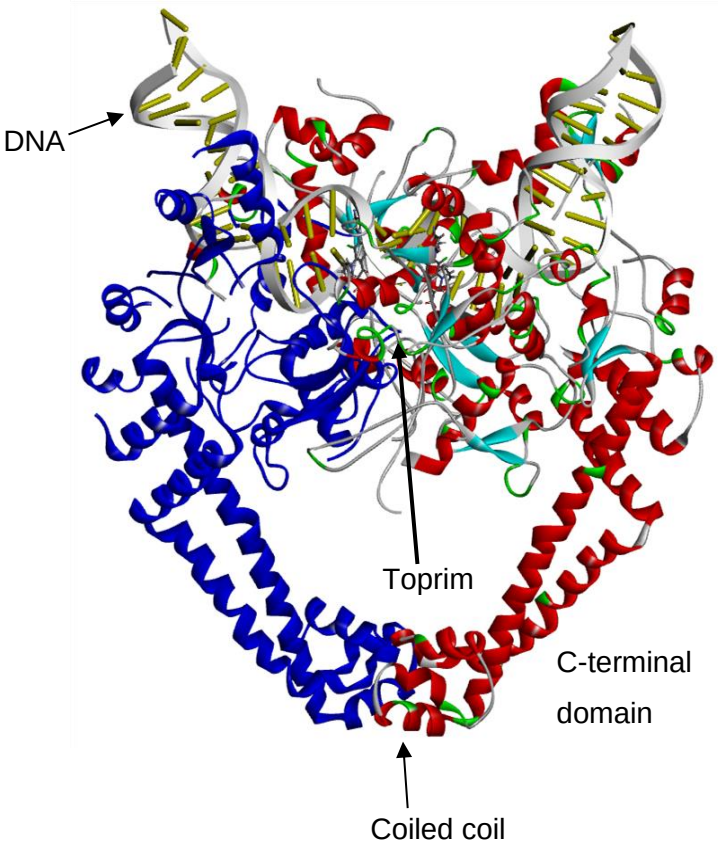

Figure 1.6: Crystal structure of yeast DNA Topo II enzyme bound to the DNA.[38] Reproduced from X-ray structure coordinates of Protein Data Bank (PDB) entry 3FOE.

1.7. Topoisomerase I and II inhibitors

Compounds that inhibit DNA topoisomerases are categorized into two groups according to their mechanisms of action: interfacial inhibitors and catalytic inhibitors, often called topoisomerase poisons and topoisomerase inhibitors, respectively.[29] Interfacial inhibitors act by blocking the enzyme from ligating cleaved DNA strands. These are the most commonly used class of topoisomerase II inhibitors.[39]

They reside at the interface between the enzyme and the DNA and physically hinder DNA ligation by the enzyme, through non-covalent contacts at the cleavage site of the enzyme-DNA complex. This leaves the DNA with permanent double-strand breaks. Consequently, cleaved DNA complexes accumulate within the cell thus overwhelming it with damage leading to cell apoptosis.[29,40]

Catalytic inhibitors, however, are a diverse group of compounds known for the following abilities: inhibition of topoisomerases from binding to DNA, inhibition of ATP binding, and lastly stabilization of the noncovalent DNA-enzyme complex. These compounds play a role as antineoplastic agents, they are also used as cardio-protectors or to enhance the activity of other compounds.[35,37]

1.7.1. Topoisomerase I inhibitors

Most Topo I inhibitors are interfacial poisons. These inhibitors prevent DNA religation through three distinct processes: 1) the binding of Topo I to a pre-formed drug-DNA complex, 2) recognition of the DNA-enzyme binary complex by the drug, and 3) the binding of the DNA to a drug-enzyme complex.[41] Interfacial inhibitors turn the enzyme into a damaging agent and are therefore called topoisomerase poisons. These compounds specifically bind to the enzyme-DNA complex in tumor cells thus inhibiting DNA religation which in turn causes the accumulation of enzyme-DNA adducts. The DNA replication fork is believed to collide with trapped enzyme-DNA adducts, creating more double-strand breaks which eventually results in apoptotic cell death.[42]

Topo I interfacial inhibitors have a planar nature, which allows them to bind between DNA base pairs next to the cleaved DNA strand.[42] These compounds have an available electron pair close to Arg364 residue which may result in drug resistance when altered. The binding of the drug to DNA is augmented by drug contact with Asn352 and Glu356 which undergo side-chain conformation to properly accommodate the drug.[42]

Camptothecin (CPT) (Figure 1.7) is an organic compound isolated from the Chinese tree, *Camptotheca acuminate,* in 1966.[19,21,41] It was the first compound to be identified as Topo I inhibitor, followed by Topo I being validated as a target for cancer therapy. Initially, chemotherapeutic use of camptothecin was limited by poor solubility and toxicity towards normal cells. The discovery of topo I as its target, however, triggered interest in searching for more soluble, less toxic, and more active compounds. As a result, camptothecin derivatives, topotecan, and irinotecan (shown in Figure 1.7 below) were discovered and are currently in clinical use.[41,42]

Topotecan is used for the treatment of small cell lung cancer and fluoropyrimidine-refractory ovarian cancer; while irinotecan is a prodrug that requires to be hydrolyzed to its active metabolite by carboxylesterase, it is used for the treatment of colorectal cancer. An X-ray crystal structure model of the Topo I-DNA complex bound to camptothecin analog, topotecan, has been reported and published.[42]

This model assisted in elucidating the structure and activity relation of camptothecin compounds, although it has not been possible to explain how other analogs operate.[42] Figure 1.6 below shows a 3.0 Å X-ray structure of ternary camptothecin bound to the topoisomerase I-DNA complex.

The figure illustrates the overall structure of the Topo I-DNA complex bound to topotecan (a), the chemical structure of topotecan (b), and a close-up view of the drug in the enzyme's active site (c). The drug compound binds through intercalation with the E-ring of the compound located very close to the active site. Lactone oxygen on C21 is positioned 4.0 Å away from the phosphodiester oxygen connecting thymidine-10 and Tyr723; it is also 3.8 Å away from the N atom of Lys532. The oxygen on the pyridine ring is shown to be 4.0 Å away from the Asn722 nitrogen side chain. The C20 hydroxyl is 3.4 Å from the Oδ1 side chain atom of Asp533, a residue known to be required for enzyme sensitivity to CPT. The closest protein-drug interaction in the CPT ternary complex structure is 2.9 Å from an N of Arg364 to a free electron pair of the B-ring N1 of CPT.[42]

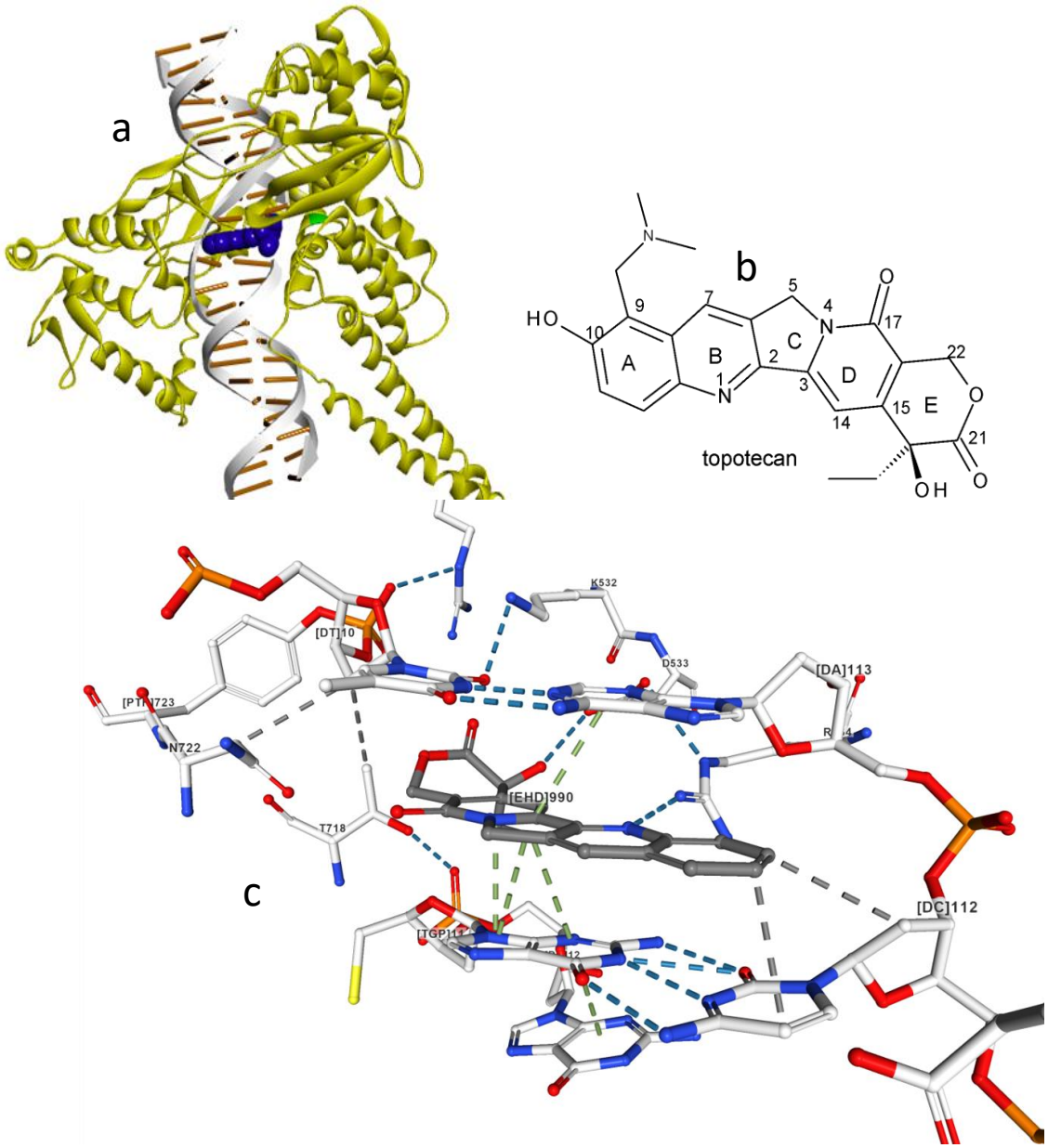

Figure 1.7: Å X-ray structure of Topo I-DNA ternary complex bound to topotecan. (a) shows the overall structure, topotecan (blue) is shown in space-filling mode bound into the intercalation binding pocket at the center of the DNA and protein, the DNA molecule is shown in white and the ribbon representation of a protein is shown in yellow. (b) the chemical structure of topotecan. (c) shows a close-up view of the drug in the enzyme's active site; grey bonds show the hydrophobic interaction, green bonds show the π-interactions between topotecan and DNA bases, hydrogen bonds are shown in blue.[42] Reproduced from X-ray structure coordinates of PDB entry 1T8I.

1.7.2. Topoisomerase II inhibitors

This category of topoisomerases consists of both interfacial and catalytic inhibitors, although interfacial inhibitors are the most commonly used class.[39] Good examples of Topo II poisons are etoposide and teniposide (shown in Figure 1.9); these compounds are derivatives of the 4-epipodophyllotoxin compound.

Etoposide is mainly used to treat testicular cancer which is resistant to other treatments; it is also used for small lung cancer, lymphomas, chronic carcinomas, malignant melanomas as well as Kaposi's sarcoma. Teniposide is used to treat lymphomas; its use, however, is less frequent compared to that of etoposide.[41] The activity of these compounds is cell cycle-dependent with a maximum peak during the S and C2 phases of mitosis.

These compounds inhibit DNA religation in two ways; first by their activation through oxidation-reduction reaction which yields a compound suitable to directly bind to the DNA; second, by preventing the release of ADP during ATP hydrolysis which completely stops its activation through oxidation-reduction to result in an active compound that binds to the DNA. The O-methylated compound (etoposide catechol) of etoposide has been reported to have the same potency as the parent molecule. This molecule is eventually oxidized to an ortho-quinone metabolite which in turn partakes in the inhibition of DNA religation.[41]

The 2.16 Å crystal structure of the etoposide-bound stabilized cleavage complex has been reported, shown in Figure 1.8, and it shows the interaction between DNA, protein, and the drug. The structure contains a duplex DNA symmetrically encircled by dimeric topo2core. It also contains two etoposide molecules on either subunit as well as six magnesium(II) ions. The cleavage complex formation is confirmed by scissile phosphates at the anticipated locations followed by breakages of phosphodiester bonds and the presence of phosphotyrosyl adducts between two tyrosine residues on the active side.[22]

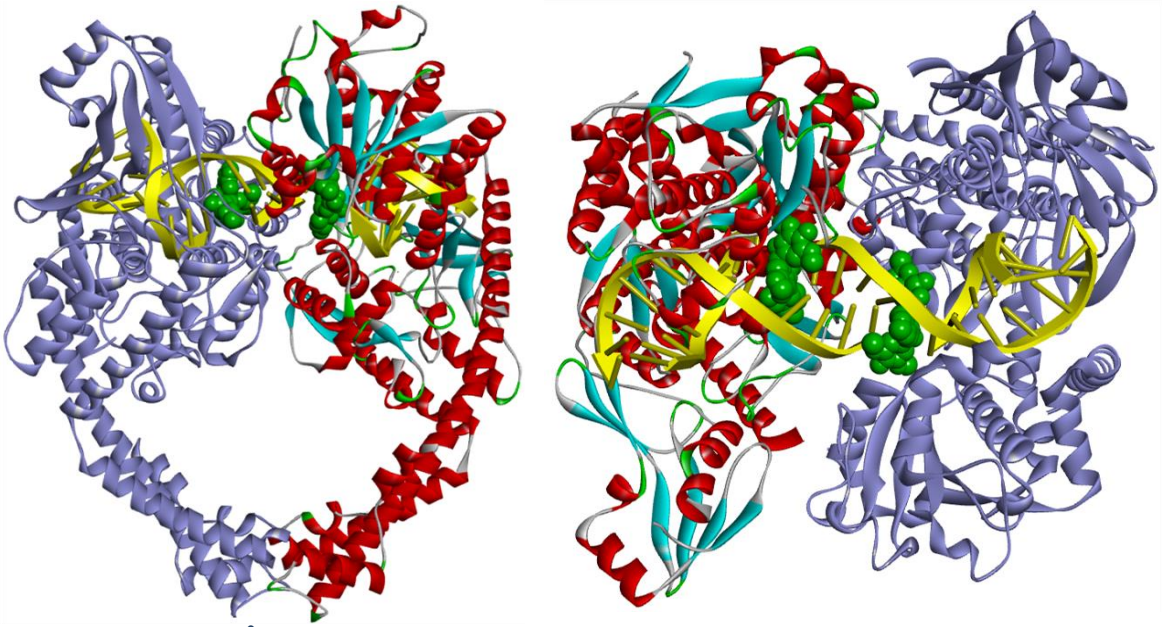

Figure 1.8: 2.16 Å crystal structure of etoposide-bound stabilized cleavage complex.[22] Reproduced from X-ray structure coordinates of PDB entry 3QX3.

1.7.3. Topoisomerase II catalytic inhibitors

Unlike Topo II interfacial inhibitors, Topo II catalytic inhibitors act on other steps in the catalytic cycle other than stabilizing the cleavable complex. They are a diverse group of compounds that hinder the binding of DNA to Topo II, interfere with Topo II ATP binding, or preserve the noncovalent DNA-Topo II complexes.[39] They can be used for different purposes such as their activity as modulators, antineoplastic agents, or as modulators to enhance the other agents' efficacy, this makes them different from topoisomerase poisons which only serve in tumor activities.

So far Topo II catalytic inhibitors are restricted to aclarubicin and sobuzoxane (Figure 1.9). Aclarubicin has been shown to inhibit Topo II in a concentration-dependent manner.[39] For instance, at higher concentration aclarubicin, stabilizes the DNA-Topo II complex, at normal concentrations, it inhibits the binding of the Topo II to DNA.

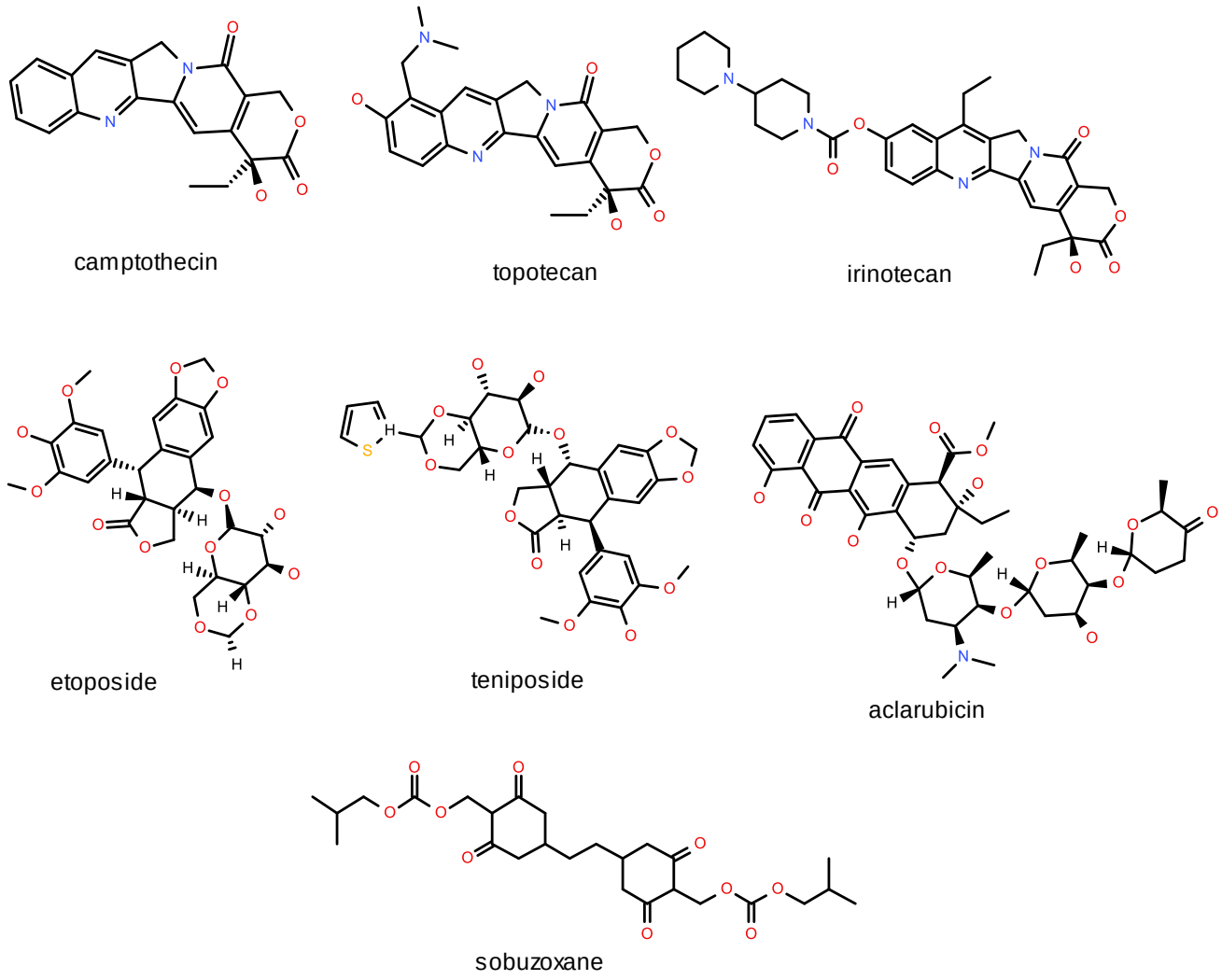

Figure 1.9: Organic Topo I inhibitors (camptothecin, topotecan, and irinotecan) and Topo II inhibitors (etoposide, teniposide, aclarubicin, and sobuzoxane).[39]

1.8. Metallodrugs as topoisomerase inhibitors

DNA topoisomerases have been identified as key targets in cancer treatment. However, most topoisomerase inhibitors found in clinical use are organic drugs.[17] Camptothecin, as mentioned above, is a common organic drug that targets topo I in cancer cells. Topo II, however, is a target to several organic drugs including, etoposide, mitoxantrone, and doxorubicin. Other compounds such as intoplicine, β-Lapachone, saintopin, and inoloquinolinedione have been identified as potential inhibitors for both enzymes.

Metallodrugs known to inhibit topoisomerase enzymes are Au(III) compounds such as Au(III) porphyrin complexes, Au(III) amides as well as Au(III) macrocycles. Two Au(III) porphyrin complexes, [Au(4-glucosyl-TPP)Cl] (H_2(4-glucosyl-TPP) = meso-tetrakis(4-β-D-glucosylphenyl)-porphyrin) and [Au(TMPyP]Cl_5 ($[H_2TMPyP]^{4+}$ = meso-tetrakis(N-methylpyridium-4yl) porphyrin) were proven to inhibit TopoI's relaxation activity of supercoiled DNA. They bind to the DNA in vitro with the binding constant between 4.9×10^5 and 4.1×10^6 dm^3 mol. Their interaction with the DNA is through intercalation and it is similar to that of, Ethidium Bromide (EB, a known DNA intercalator).[20] The flow cytometric analysis showed that both compounds arrest the cell cycle S-phase of cancer cells meaning that the anticancer activity happens due to termination of the replication process.[20]

Furthermore, a newer class of Au(III) square planar cationic complexes was proven to inhibit both Topo I and Topo II. These compounds include Au(III) macrocycles and Au(III) amides.[29,43] Au(III) macrocycles incorporate an alkyl chain bridge on one side connected to two pyrrole-ring systems attached to quinolone constituent on the other side. They are specifically designed to be DNA intercalators. According to DNA binding results, they intercalate DNA with an affinity constant greater than 10^6 M^{-1} bp. The screening of the most active compound (Figure 1.10) against NCI's panel of 60 different human cancer cell lines indicated that the compound behaves most similarly to an organic Topo I poison, camptothecin. Several topical enzyme assays were used to prove that this compound is a catalytic inhibitor Topo 1 based on the fact that its catalytic inhibition of Topo I was three orders of magnitude greater than that of Topo II.[29,43]

The Au(III) amides, however, inhibit both Topo I and Topo II. Topo II inhibition assay showed that amides act as interfacial inhibitors at low concentrations whereas at high concentrations they behave as catalytic inhibitors. However, with the use of enzyme inhibition assay that can distinguish between Topo I interfacial poisons and catalytic inhibitors, it was possible to prove that Au(III) amides are catalytic inhibitors of Topo I and not interfacial inhibitors.[43]

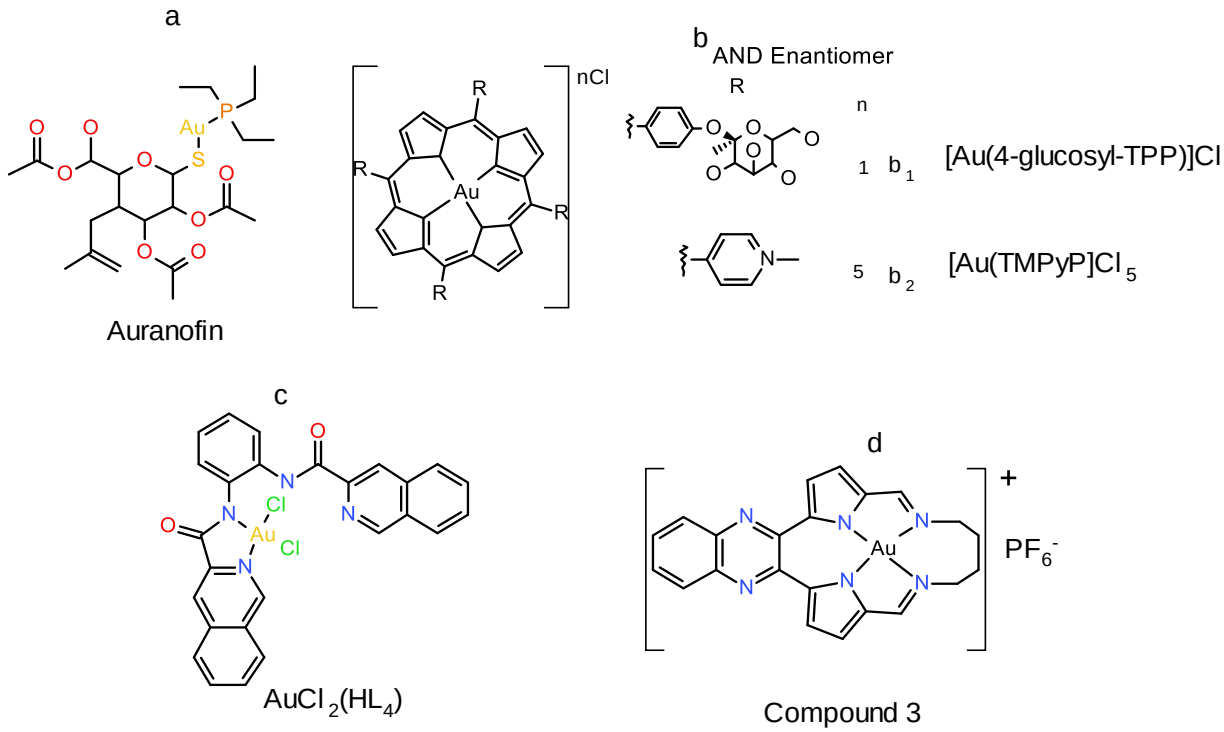

Figure 1.10: Structures of known cytotoxic Au(III) chelates: a) auranofin[18], b_1) [Au(4-glucosyl-TPP)]Cl, b_2) [Au(TMPyP]Cl_5,[20] c) $AuCl_2(HL_4)$ amides[43], d) Au(III) macrocycles[29]. The latter two Au(III) systems are proven Topo I and Topo II inhibitors.

1.9. AIM

The project aims to synthesize and characterize several novel bis(indazole-imine) ligands suitable for chelating Au(III) to give a new library of square-planar d^8 Au(III) complexes with the potential ability to target DNA. The ligands are characterized by two indazole rings connected by an alkyl bridging group. Their structures are varied by changing the chain lengths and the substituents on the diamine bridge as shown in Figure 1.11 below. The Au(III) chelates will form the focus of the study as it is known that Au(III) complexes of similarly-designed bis(pyrrolide-imine) macrocycles and chelates are bioactive due to the way the Au(III) ion interacts with biomolecules such as DNA. Coordination of ligands to Au(III) metal ion leads to deprotonation of the two hydrogen atoms on the indazole NH, forming a complex with the overall charge of +1.[29]

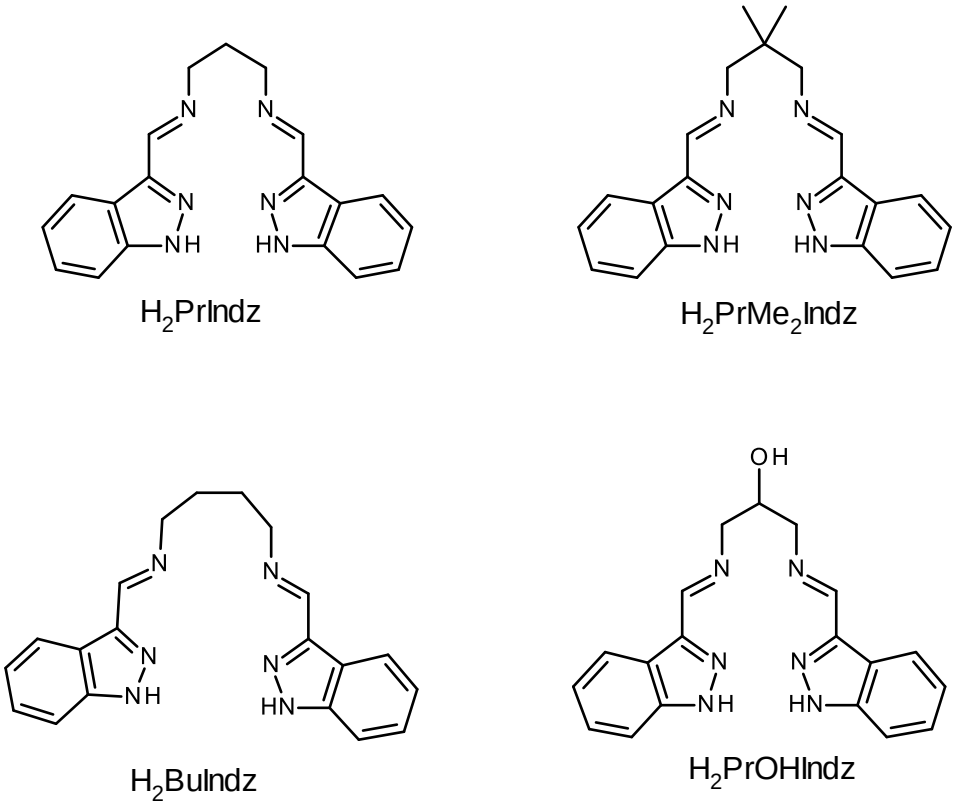

Figure 1.11: Chemical structures of novel bis(indazole-imine) ligands to be chelated to Au(III) ion in this project.

The design of these complexes allows them to interact with the DNA through intercalation; by stacking in between DNA bases using π-π as well as electrostatic interactions this is illustrated in Figure 1.12 below. As a result, they are anticipated to block essential topoisomerase enzymes from regulating DNA topology in eukaryotes and prokaryotes, thereby functioning as cytotoxic and/or bactericidal agents for potential chemotherapeutic development. This interaction is expected to interfere with the activity of Topo I and/ Topo II proteins causing cell death. The ability of the complexes to bind DNA as well as their cytotoxicity will be determined in this project.

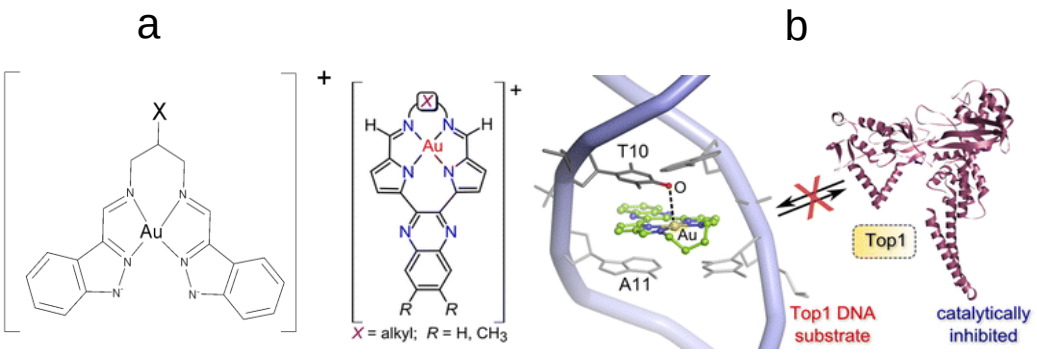

Figure 1.12: The Figure demonstrates a) the novel target Au(III) chelate and b) Au(III) macrocycle (a known cytotoxic Au(III) chelate). Based on the similarities in the directly-coordinated groups to Au(III) for the two classes of compound, we expect the target compound to possibly interact with DNA through intercalative interaction and could potentially also catalytically inhibit Topo I. Part b) of the figure is taken from Ref. 29.

1.10. Objectives

The objectives of this study were to:

1. Synthesize and fully characterize bis(indazole-imine) ligands and their corresponding Au(III) complexes using ^{1}H, ^{13}C, NMR spectroscopy as well as FTIR, UV-visible spectroscopy and single-crystal X-ray crystallography (for Au(III) complexes only).

2. Perform computational simulations using density functional theory (DFT). This will give simulated characterization data which includes geometry optimized structures, NMR spectra, UV-vis spectra as well as IR spetra. This data will be compared with the experimental data, it will also aid in interpreting experimental results.

3. Perform DNA binding assays by spectroscopy, electrophoresis and viscometry to determine the DNA binding mode of new Au(III) complexes.

4. Screen the Au(III) chelates on two breast cancer cells, MDA-MB-231 and MCF-7, and one normal cell line, HEK-293.

1.11. References

(1) 'Chapter 11 - Drug Targeting in Anticancer Chemotherapy' (2008) *Medicinal Chemistry of Anticancer Drugs*, pp.351–385. doi: 10.1016/B978-0-444-52824-7.00011-1.

(2) Hejmadi, M., 2010. *Introduction to Cancer Biology, 2nd Edition*; pp.1-48.

(3) National Cancer Institute. Comprehensive cancer information, viewed 20 February 2019, https://www.cancer.gov/.

(4) Dorfman, R.I., 1975. Chemistry and pharmacology of naproxen. *Arzneimittel-Forschung*, *25*(2A), pp.278-281.

(5) Wajed, S.A., Laird, P.W. and DeMeester, T.R., 2001. DNA methylation: an alternative pathway to cancer. *Annals of surgery*, *234*(1), p.10.

(6) Wilgar Hannah,Boldú Laura Olivares,Danson Mark ,Steve Scott, G. F. yourgenome https://www.yourgenome.org/facts/what-types-of-mutation-are-there (accessed Jul 7, 2019).

(7) Peedicayil, J., 2016. Epigenetic drugs for multiple sclerosis. *Current neuropharmacology*, *14*(1), pp.3-9.

(8) Doll, R. and Peto, R., 1981. The causes of cancer: quantitative estimates of avoidable risks of cancer in the United States today. *JNCI: Journal of the National Cancer Institute*, *66*(6), pp.1192-1308.

(9) Lax, A.J. and Thomas, W., 2002. How bacteria could cause cancer: one step at a time. *Trends in microbiology*, *10*(6), pp.293-299.

(10) Zamanian, A. and Hardiman, C., 2005. Electromagnetic radiation and human health: A review of sources and effects. *High Frequency Electronics*, *4*(3), pp.16-26.

(11) American Cancer Society. Cancer Information, viewed 13 July 2019, www.cancer.org.

(12) Sun, J., Wei, Q., Zhou, Y., Wang, J., Liu, Q. and Xu, H., 2017. A systematic analysis of FDA-approved anticancer drugs. *BMC systems biology*, *11*(5), pp.1-17.

(13) Housman, G., Byler, S., Heerboth, S., Lapinska, K., Longacre, M., Snyder, N. and Sarkar, S., 2014. Drug resistance in cancer: an overview. *Cancers*, *6*(3), pp.1769-1792.

(14) Karavasilis, V., Reid, A., Sinha, R., Bono, J. S. D. E.,2008. Cancer drug design and discovery. *Elsevier*. 4(9), pp. 150-173.

(15) Liu, W. and Gust, R., 2016. Update on metal N-heterocyclic carbene complexes as potential anti-tumor metallodrugs. *Coordination Chemistry Reviews*, *329*, pp.191-213.

(16) Mjos, K. D., Orvig, C., 2014. Metallodrugs in medicinal inorganic chemistry. *Chemical Reviews,114* (8), pp.4540–4563.

(17) Ott, I. and Gust, R., 2007. Non-platinum metal complexes as anti-cancer drugs. *Archiv der Pharmazie: An International Journal Pharmaceutical and Medicinal*

Chemistry, *340*(3), pp.117-126.

(18) Berners-Price, S.J. and Filipovska, A., 2011. Gold compounds as therapeutic agents for human diseases. *Metallomics*, *3*(9), pp.863-873.

(19) P Pommier, Y., 2006. Topoisomerase I inhibitors: camptothecins and beyond. *Nature Reviews Cancer*, *6*(10), pp.789.

(20) Sun, R.W.Y., Li, C.K.L., Ma, D.L., Yan, J.J., Lok, C.N., Leung, C.H., Zhu, N. and Che, C.M., 2010. Stable anticancer gold (III)–porphyrin complexes: Effects of porphyrin structure. *Chemistry–A European Journal*, *16*(10), pp.3097-3113.

(21) Staker, B. L., Hjerrild, K., Feese, M. D., Behnke, C. A., Burgin, A. B., Stewart, L., 2002. Nonlinear partial differential equations and applications: The Mechanism of Topoisomerase I Poisoning by a Camptothecin Analog. *National Academy of Sciences*, *99*(24), pp.15387–15392.

(22) Wu, C.C., Li, T.K., Farh, L., Lin, L.Y., Lin, T.S., Yu, Y.J., Yen, T.J., Chiang, C.W. and Chan, N.L., 2011. Structural basis of type II topoisomerase inhibition by the anticancer drug etoposide. *Science*, *333*(6041), pp.459-462.

(23) Wilson, C.R., Fagenson, A.M., Ruangpradit, W., Muller, M.T. and Munro, O.Q., 2013. Gold (III) complexes of pyridyl-and isoquinolylamido ligands: structural, spectroscopic, and biological studies of a new class of dual topoisomerase I and II inhibitors. *Inorganic chemistry*, *52*(14), pp.7889-7906.

(24) Germe, T., Vörös, J., Jeannot, F., Taillier, T., Stavenger, R.A., Bacqué, E., Maxwell, A. and Bax, B.D., 2018. A new class of antibacterials, the imidazopyrazinones, reveal structural transitions involved in DNA gyrase poisoning and mechanisms of resistance. *Nucleic acids research*, *46*(8), pp.4114-4128.

(25) Tse-Dinh, Y.C., 2015. Targeting bacterial topoisomerase I to meet the challenge of finding new antibiotics. *Future medicinal chemistry*, *7*(4), pp.459-471.

(26) Gupta, R., Felix, C.R., Akerman, M.P., Akerman, K.J., Slabber, C.A., Wang, W., Adams, J., Shaw, L.N., Tse-Dinh, Y.C., Munro, O.Q. and Rohde, K.H., 2018. Gold (III) macrocycles and chelates targeting Mycobacterium tuberculosis and Mycobacterium abscessus: evidence for inhibition of topoisomerase 1A. *Antimicrobial Agents and Chemotherapy*.

(27) Sun, X., Tsang, C.N. and Sun, H., 2009. Identification and characterization of metallodrug binding proteins by (metallo) proteomics. *Metallomics*, *1*(1), pp.25-31.

(28) Bailly, C., 2012. Contemporary challenges in the design of topoisomerase II inhibitors for cancer chemotherapy. *Chemical Reviews*, *112*(7), pp.3611-3640.

(29) Akerman, K.J., Fagenson, A.M., Cyril, V., Taylor, M., Muller, M.T., Akerman, M.P.

and Munro, O.Q., 2014. Gold (III) macrocycles: nucleotide-specific unconventional catalytic inhibitors of human topoisomerase I. *Journal of the American Chemical Society*, *136*(15), pp.5670-5682.

(30) Wang, J., Champoux, J., T, la., Gellert, M., An, P.; The, P., 1971.DNA Topoisomerases. *Nature*, 5(1), pp.125–144.

(31) Wigley, D.B., 1995. Structure and mechanism of DNA gyrase. In *Nucleic acids and molecular biology* (pp. 165-176). Springer, Berlin, Heidelberg.

(32) Lima, C.D., Wang, J.C. and Mondragón, A., 1994. Three-dimensional structure of the 67K N-terminal fragment of E. coli DNA topoisomerase I. *Nature*, *367*(6459), p.138.

(33) Pommier, Y., 2009. DNA topoisomerase I inhibitors: chemistry, biology, and interfacial inhibition. *Chemical Reviews*, *109*(7), pp.2894-2902.

(34) Kampranis, S.C., Bates, A.D. and Maxwell, A., 1999. A model for the mechanism of strand passage by DNA gyrase. *Proceedings of the National Academy of Sciences*, *96*(15), pp.8414-8419.

(35) Pommier Editor, Y. *DNA Topoisomerases and Cancer*; Pommier, Y., Ed.; Cancer Drug Discovery and Development; Springer New York: New York, NY, 2012. https://doi.org/10.1007/978-1-4614-0323-4.

(36) Deweese, J.E. and Osheroff, N., 2009. Coordinating the two protomer active sites of human topoisomerase IIα: nicks as topoisomerase II poisons. *Biochemistry*, *48*(7), pp.1439-1441.

(37) Laponogov, I., Pan, X.S., Veselkov, D.A., McAuley, K.E., Fisher, L.M. and Sanderson, M.R., 2010. Structural basis of gate-DNA breakage and resealing by type II topoisomerases. *PloS one*, *5*(6), pp.11338.

(38) Laponogov, I., Sohi, M.K., Veselkov, D.A., Pan, X.S., Sawhney, R., Thompson, A.W., McAuley, K.E., Fisher, L.M. and Sanderson, M.R., 2009. Structural insight into the quinolone–DNA cleavage complex of type IIA topoisomerases. *Nature structural & molecular biology*, *16*(6), pp.667.

(39) Larsen, A.K., Escargueil, A.E. and Skladanowski, A., 2003. Catalytic topoisomerase II inhibitors in cancer therapy. *Pharmacology & Therapeutics*, *99*(2).167-181.

(40) Gibson, E. G., Deweese, J. E., 2013. Covalent poisons of topoisomerase II. *Current Topics in Pharmacology*, *17* (1), p.1–12.

(41) 'Chapter 7 - DNA Intercalators and Topoisomerase Inhibitors' (2008) *Medicinal Chemistry of Anticancer Drugs*, pp. 199–228. doi: 10.1016/B978-0-444-52824-7.00007-X.

(42) Staker, B.L., Feese, M.D., Cushman, M., Pommier, Y., Zembower, D., Stewart, L. and

Burgin, A.B., 2005. Structures of three classes of anticancer agents bound to the human topoisomerase I− DNA covalent complex. *Journal of medicinal chemistry*, *48*(7), pp.2336-2345.

(43) Wilson, C.R., Feinson, A.M., Ruangpradit, W., Muller, M.T. and Munro, O.Q., 2013. Gold (III) complexes of pyridyl-and isoquinolylamido ligands: structural, spectroscopic, and biological studies of a new class of dual topoisomerase I and II inhibitors. *Inorganic chemistry*, *52*(14), pp.7889-7906.

Chapter 2

Experimental Section

2.1. General Methods

2.1.1. Solvents and Reagents

All fine chemicals were purchased from Sigma-Aldrich and were used without additional purification. Analytical grade solvents were purchased from Merck and were dried with molecular sieves before use.

2.1.2. Analytical techniques

2.1.2.1. Nuclear magnetic resonance (NMR) spectroscopy

NMR spectra for ^{1}H and ^{13}C NMR studies were recorded on Bruker Avance III 400 and 300 NMR spectrometers at frequencies of 400 MHz and 300 MHz, respectively, for ^{1}H and ^{13}C was measured at a frequency of 100 MHz and 75 MHz on the 400 and 300 MHz NMR spectrometers, respectively. Either the 5 mm BBOZ or TBIZ probes were used. All the chemical shifts for both proton and carbon were recorded concerning the appropriate reference solvent. MestReNova software (version 9.0.0-12821) was used to analyze NMR spectra.

2.1.2.2. Ultraviolet-visible (UV-vis) spectroscopy

Absorbance spectra were recorded using a PerkinElmer UV-vis Lambda 365 spectrometer connected to a Peltier controller and a Peltier Temp multicell unit set at 25 °C. The spectral data were analyzed with the UV Express software (Version 4.1.2.). The samples were run in increasing concentrations for characterization and determination of molar absorptivity constants. Quartz cuvettes with a path length of 10 mm were used.

2.1.2.3. Fourier-transform infrared (FTIR) spectroscopy

FTIR spectra of powder samples were recorded using a Bruker Alpha FTIR spectrometer incorporating a Bruker Platinum diamond ATR sampling accessory. Spectra were analyzed using the OPUS software package on the spectrometer (version 7.5).

2.1.2.4. High-resolution mass spectroscopy (HRMS)

Mass spectra for all samples were recorded with Bruker Compact Q-TOF high-resolution mass spectrometer using Bruker Daltronics HyStar 3.2 SR4 software. Bruker Compass DataAnalysis software (Version 4.3) was used to analyze chromatograms. Samples of pure compounds (10 µg/mL) were prepared in HPLC grade acetonitrile for metal chelates and HPLC grade methanol for ligands in serial dilution.

2.1.2.5. X-ray crystallography

Single crystals of [Au(PrIndz)]Cl, [Au($PrMe_2$Indz)]PF_6, [Au(PrOHIndz)]PF_6, and the Au(III) precursor, [Bu_4N][$AuCl_4$], were grown using different crystallization methods as stated in Chapter 3. Suitable crystals were individually selected and mounted as follows: [Bu_4N][$AuCl_4$] was mounted with Paratone oil on a nylon loop and fixed to a brass collet on a Bruker APEX2 CCD (fine focus sealed tube X-ray source) diffractometer. [Au(PrIndz)]Cl was mounted on a 300 µm MiTeGen needle loop in NVH oil on a Bruker D8 Venture diffractometer. [Au($PrMe_2$Indz)]PF_6 was mounted using NVH oil on a nylon loop (Hampton Research) on a Bruker APEX-II CCD diffractometer. [Au(PrOHIndz)]PF_6 was mounted in NVH oil on a 200-micron MiTeGeN cryoloop before flash cooling in nitrogen vapor to -100 °C on a Bruker D8 Venture diffractometer. All the crystals were kept at 173.15 K during data collection. Using Olex2,[1] the structures were solved with the ShelXT[2] structure solution program using intrinsic phasing and refined with the ShelXL[3] refinement package using least-squares minimization.

2.1.3 DNA binding studies

2.1.3.1. Gel electrophoresis

The gel electrophoresis experiments were conducted in hand-cast 1.25% agarose gels dissolved in 1x TAE buffer in a Mini-Sub-Cell GT Agarose Gel electrophoresis System (Bio-Rad). (The buffer was purchased from Sigma-Aldrich and was diluted 10x with type 1 ultrapure water to maintain the working concentration 1 mM EDTA,40 mM TRIS-acetate and pH 8.3). Ethidium bromide solution (0.5 mg/L in Type 1 ultrapure water) was used as a staining agent and the gels were stained for 30 minutes and were washed with type 1 ultrapure water for 20 minutes. The gels were visualized with a Syngene G: Box Chemi XRQ gel doc system, with mid-wave UV transillumination and UV filter (GeneSys 1.4.6.0)

2.1.3.2. Viscometry

Viscosity measurements for metal chelates were conducted with an Anton Paar Lovis 2000 M rolling ball micro viscometer. Measurements were carried out in triplicate as a function of the concentration of Au(III) chelate added to a fixed concentration of ctDNA at 37 °C in 1x Tris-HCl (pH 7) buffer. The viscosity data were averaged to obtain a normalized plot of $(\eta - \eta_0/\eta_0)^{1/3}$ versus $1/r$, where r equals the moles of ligand per mole of DNA base pairs and η and η_o are the dynamic viscosities in the presence and absence of compound, respectively.

2.1.4. Biological studies

2.1.4.1. Cell culturing

To culture the MCF-7, MDA-MB-231, and HEK-293 cells a Dulbecco's modified Eagles medium (DMEM) comprising 4.5 g/L D-glucose-glutamine and pyruvate was used. The 10% fetal bovine serum albumin and 1% penicillin/streptomycin were added to the media for MCF-7 and HEK-293 cell lines and MDA-MB-23 Ham's F12 was further added in a ratio of 3:1 (DMEM: Ham's F12). Each cell line was incubated for 24, 48, and 72 hours in an incubator set at 37 ºC under a 5% CO_2 humidified atmosphere.

2.1.4.2. Sub-culturing of cells

MDA-MB-231, MCF7, and HEK-293 cell lines.

2 mL phosphate-buffered saline (PBS) was used to wash cells once and a 2 mL of 1% trypsin-EDTA was added to the flask before incubation at 37 ºC for 5-10 minutes. Afterward, the flask was shaken to detach cells from the surface. An aliquot (4 mL) of supplemented was added to deactivate trypsin. The cells were then transferred to a new flask depending on the confluency required. The cells were then passaged every 48 hours.

2.1.4.3. Cell stocks

Cells were removed and the above method was followed to collect them. This was followed by centrifugation in an Eppendorf centrifuge MiniSpin at a speed of 4000 rpm for 4 minutes. The resulting pellet was resuspended in 70% DMEM, 10% DMSO, and 20% FBS to a total volume of 1 mL. A cryogenic vial was used for the storage of cells at -80 ºC until required.

2.1.4.4. Revival of stocks

Cells were removed from the stocks and were thawed in a 37 ºC water bath, at the end the volume of thawed cells was 1 mL. These cells were then transferred to an appropriate corning cell culture flask (25 cm^2 and 75 cm^2) filled with 4 mL DMEM followed by incubation for 24 hours. Afterward, the old media was replaced with the new one (5 mL) and the cells were incubated until they reached confluence.

2.1.4.5. Cell counting with trypan blue exclusion assay

The cells were detached from the surface by replacing the media with 2 mL of 1x trypsin/EDTA followed by incubation at 37 ºC, the 2 mL of the media was then added to deactivate trypsin. 0.4% 1:1 trypan blue was transferred to the cell suspension to make up the volume of 10 µL to stain dead cells. The suspension was then blended on parafilm and was transferred to the Neubauer haemocytometer.

This was followed by the determination of cellular viability:

$$\%\ \text{Cell viability} = \frac{\text{No. of live cells (unstained)}}{\text{Total no. of counted cells (dead and live)}} \times 100$$

Only cells with viability above 90 % were used in all experiments.

2.1.4.6. Cell plating

MDA-MB-231, MCF7, and HEK-293 cell lines. Cells plating was done in triplicates. Before cell plating, cells (MDA-MB-231, MCF7, and HEK-293 cell lines) were collected and counted as illustrated above. 5000 cells were added to 96 well plates to a final volume of 45 µL cells and then incubated for optimum adhesion for 24 hours before treatments. To prevent media evaporation during incubation, autoclaved H_2O was added to the outer wells of the plates.

2.1.4.7. Growth inhibition with MTT assay

Stock concentrations of test compounds: $[Au(PrMe_2Indz)]PF_6$, $[Au(PrOHIndz)]PF_6$, and cisplatin were prepared in 10% DMSO and DMEM before treatment. 5 µL of each test compound (at varying concentrations) were added to the above media to a volume of 50 µL in each well. Cisplatin was used as a positive control. Cells were treated with compound concentrations: 5, 10, 20, 50, 100 µM, followed by 24-hour incubation. 5 mg/L of MTT in PBS was transferred to each well and cells were incubated for 2-hours. This was followed by the addition of solubilisation solution, 10% SDS and 10 mM HCl, of volume equivalent to the volume of media present in each well. The cells were again incubated for 16 hours at 37 °C. A microtiter plate reader Multiskan GO Microplate Reader was then used to determine the optical density of the wells at 570 nm. This was followed by the determination of percentage viability/inhibition. All the graphs were plotted on GraphPad Prism 5 initially, and subsequently with Origin Pro 2019.

Microsoft Excel was used to determine the statistical analysis and the final IC_{50} values were calculated by curve fitting in Origin Pro 2019. The experiments were carried out in duplicates and the student t-test was performed to calculate statistical significance. The significance of the observation was estimated using a p-value of less than 0.05. For each 96-well plate, a Z-factor was calculated and assays with the Z-factor greater than 0.5 were included in the statistical analysis.

2.2. Synthesis and Characterization of Ligands

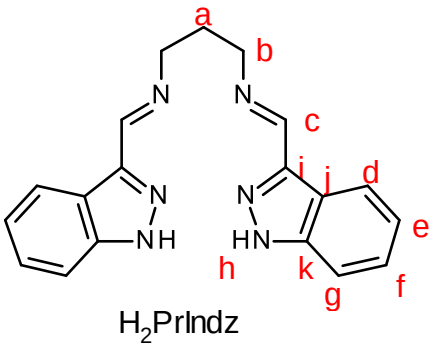

H_2PrIndz

(*E*)-1-(1H-indazol-3-yl)-N-[3-[(*E*)-1H-indazol-3-ylmethyleneamino]propyl]methanimine (H_2PrIndz). 1H-indazole-3-carboxaldehyde (0.6012 g, 4.114 mmol), 1.3-diaminopropane (173 µL, 2.073 mmol), and approximately two spatula spoonfuls of magnesium sulfate ($MgSO_4$) were added into a 100 mL round-bottomed flask. Ethanol (20 mL) was added and the mixture was refluxed for three hours. The reaction mixture was then allowed to cool. After cooling, $MgSO_4$ was removed by suction filtration. Ethanol was removed from the filtrate by rotary evaporation and the product was isolated as a fluffy yellowish powder (isolated mass: 0.6372 g, yield: 93%).

^{1}H NMR (300 MHz, DMSO-d_6) δ 13.38 (s, 2H, **h**), 8.67 (s, 2H, **c**), 8.29 (dt, J = 8.1, 1.1 Hz, 2H, **g**), 7.59 (dt, J = 8.4, 1.0 Hz, 2H, **d**), 7.41 (ddd, J = 8.3, 6.9, 1.2 Hz, 2H, **f**), 7.22 (ddd, J = 8.0, 6.9, 0.9 Hz, 2H, **e**), 3.85 – 3.74 (m, 4H, **b**), 2.09 (p, J = 6.7 Hz, 2H, **a**). ^{13}C NMR (75 MHz, DMSO-d_6) δ 157.08 (**c**), 143.14 (**k**), 142.01 (**i**), 127.50 (**f**), 123.05 (**e**), 122.60 (**g**), 121.42 (**d**), 111.20 (**j**), 59.76 (**b**), 33.04 (**a**). UV-vis: (DMSO) λ_{max} [nm] (ε/M^{-1} cm^{-1}): 281 (14 273), 300 (11805). IR (cm^{-1}): 3175br ν(N-H), 2921s ν(CH_2), 1644m ν(N=C),1476m ν(C=C). HRMS (m/z): $[M]^+$ calculated for [$C_{19}H_{18}N_6$]: 331.39 amu; found: 331.15 amu.

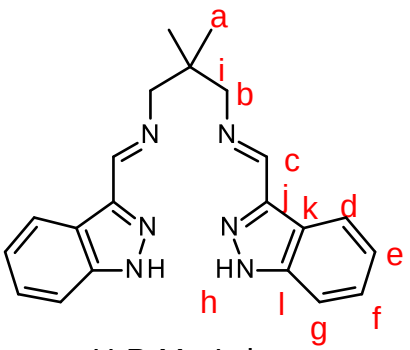

H_2PrMe_2Indz

(*E*)-1-(1H-indazol-3-yl)-N-[3-[(*E*)-1H-indazol-3-ylmethyleneamino]-2,2-dimethyl-propyl]methanimine (H_2PrMe_2Indz). 1H-indazole-3-carboxaldehyde (0.3001 g, 2.053 mmol) and 2,2-dimethyl-1,3-propanediamine (123 µL, 1.024 mmol) were ground together for 10 minutes in a warm pestle and mortar. Small portions of DCM were added to aid with grinding. The crude product was then dissolved in 20 mL DCM and was transferred into a 100 mL beaker. The mixture was stirred at room temperature. The solution turned cloudy in less than 5 minutes. It was left to stir until it was white and most of the DCM had evaporated (about 30 minutes). The remaining DCM was then removed by rotary evaporation. The resulting product was white and was dried in air overnight (isolated mass: 0.5934 g, yield: 91%).

^{1}H NMR (400 MHz, DMSO-d_6) δ 13.42 (s, 2H, **h**), 8.64 (s, 1H, **c**), 8.31 (d, J = 8.1 Hz, 2H, **g**), 7.60 (d, J = 8.4 Hz, 2H, **d**), 7.47 – 7.38 (m, 2H, **f**), 7.25 (t, J = 7.5 Hz, 2H, **e**), 3.61 (s, 4H, **b**), 1.10 (s, 6H, **a**). ^{13}C NMR (100 MHz, DMSO-d_6) δ 168.27 (**c**), 154.45 (**l**), 153.21 (**j**), 138.70 (**e**), 134.16 (**f**), 133.87 (**g**), 132.69 (**k**), 122.41 (**d**), 81.98 (**b**), 36.34 (**a**). UV-vis: (DMSO) λ_{max} [nm] (ε/M^{-1} cm^{-1}): 280 (20 544), 301 (24 236). IR (cm^{-1}): 3123br ν(N-H), 2935br ν(CH_2, CH_3), 1650s ν(N=C) 1481m ν(C=C). HRMS (m/z): $[M]^+$ calculated for [$C_{21}H_{22}N_6$]: 359.45 amu; found: 359.20 amu.

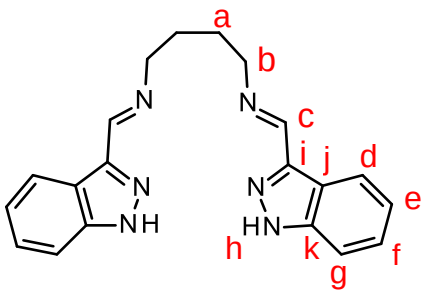

H_2BuIndz

(*E*)-1-(1H-indazol-3-yl)-N-[4-[(*E*)-1H-indazol-3-ylmethyleneamino]butyl]methanimine (H_2BuIndz). 1H-indazole-3-carboxaldehyde (0.5000 g, 3.421 mmol) and 1,4-diaminobutane (173 µL, 1.721 mmol) were ground together for 10 minutes in a warm pestle and mortar. Small portions of methanol were added to aid with grinding. The crude product was then dissolved in 20 mL methanol and then transferred into a 50 mL round-bottomed flask and stirred for about 5 minutes. The solvent was then removed by rotary evaporation and the product was characterised (isolated mass: 0.5103 g, yield: 86%).

^{1}H NMR: (400 MHz, DMSO-d_6) δ 13.42 (s, 2H, **h**), 8.65 (s, 2H, **c**), 8.25 (d, J = 8.1 Hz, 2H, **g**), 7.58 (d, J = 8.3 Hz, 2H, **d**), 7.41 (t, J = 7.6 Hz, 2H, **f**), 7.20 (t, J = 7.5 Hz, 2H, **e**), 3.71 (d, J = 5.7 Hz, 4H, **b**), 1.93 – 1.70 (m, 4H, **a**). ^{13}C NMR: (100 MHz, DMSO-d_6) δ 167.92 (**c**), 154.32 (**k**), 153.17 (**i**), 138.63 (**g**), 134.17 (**f**), 133.72 (**e**), 132.57 (**d**), 122.35 (**j**), 72.97(**b**), 40.49 (**a**). UV-vis: (DMSO) λ_{max} [nm] (ε/M^{-1} cm^{-1}): 280 (14 541), 300 (17 111). IR (cm^{-1}): 3177br ν(N-H), 2918br ν(CH_2, CH_3), 1643s ν(N=C), 147m ν(C=C). HRMS (m/z): $[M]^+$ calculated for [$C_{20}H_{20}N_6$]: 345.42 amu; found: 345.18 amu.

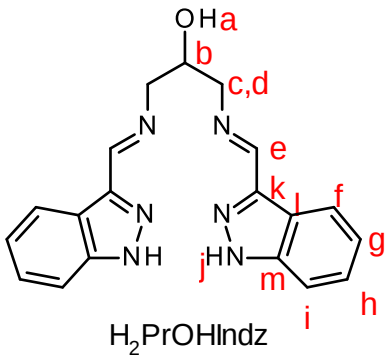

H_2PrOHIndz

1,3-bis[(*E*)-1H-indazol-3-ylmethyleneamino]propan-2-ol (H_2PrOHIndz). 1H-indazole-3-carboxaldehyde (0.2001 g, 1.369 mmol) and 1,3-diamino-2-propanol (0.06180 g, 0.6858 mmol) were ground together for 10 minutes in a warm pestle and mortar. Small portions of ethanol were added to aid with grinding. The crude product was then dissolved in 20 mL ethanol and then transferred into a 50 mL round-bottomed flask and stirred for about 5 minutes. The solvent was then removed by rotary evaporation and the product was characterized (isolated mass: 0.1830 g, yield: 77%).

^{1}H NMR (400 MHz, DMSO-d_6) δ 13.39 (s, 2H, **j**), 8.65 (s, 2H, **e**), 8.31 (d, J = 8.1 Hz, 2H, **i**), 7.59 (d, J = 8.4 Hz, 2H, **f**), 7.42 (ddd, J = 8.2, 6.8, 1.1 Hz, 2H, **h**), 7.23 (dd, J = 8.1, 6.9 Hz, 2H, **g**), 4.88 (d, J = 5.4 Hz, 1H, **a**), 4.15 (h, J = 5.5 Hz, 1H, **b**), 3.94 (ddd, J = 11.7, 5.1, 1.4 Hz, 2H, **c**), 3.79 – 3.67 (m, 2H, **d**). ^{13}C NMR (100 MHz, DMSO-d_6) δ 169.24 (**e**), 154.44 (**m**), 153.17 (**k**), 138.66 (**g**), 134.36 (**h**), 133.72 (**i**), 132.62 (**l**), 122.34 (**f**), 82.25 (**b**), 77.85 (**c,d**). IR (cm^{-1}): 3179br ν(N-H, O-H), 2865br ν(CH_2), 1645s ν(N=C) 1476m ν(C=C). UV-vis: (DMSO) λ_{max} [nm] (ε/M^{-1} cm^{-1}): 281 (15 306), 301 (19 445). HRMS (m/z): [M]$^+$ calculated for [$C_{19}H_{18}N_6O$]: 347.39 amu; found: 347.16 amu.

2.3. Synthesis of Metal Salt Precursor

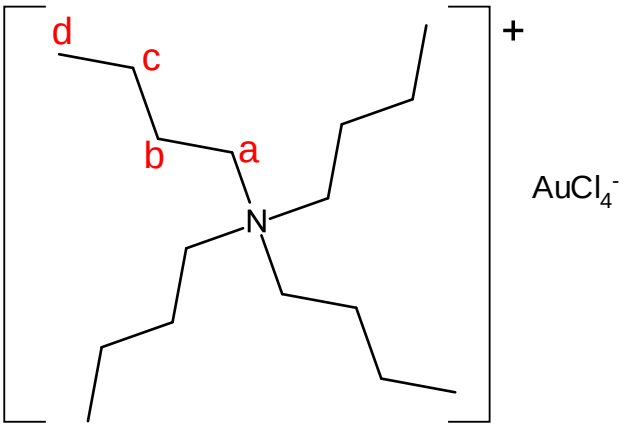

Tertbutylammonium tetrachloroaurate. Hydrogen tetrachloroaurate(III) (0.1000g, 0.2943 mmol) was dissolved in 4 mL distilled water. To this solution, tertbutylammonium bisulphate (0.0837g, 0.2465 mmol) was added forming a lipophilic gold(III) salt which immediately precipitated from the aqueous solution as a bright yellow powder. $[Bu_4N][AuCl_4]$ was extracted into DCM (5 mL portions). Organic portions were combined and dried over magnesium sulphate. DCM was removed by rotary evaporation (isolated mass: 0.1060 g, yield: 74%).

^{1}H NMR (400 MHz, DMSO-d_6) δ 3.28 – 3.06 (m, 8H, **a**), 1.57 (td, J = 12.0, 10.1, 6.2 Hz, 8H, **b**), 1.32 (h, J = 7.4 Hz, 8H, **c**), 0.94 (t, J = 7.3 Hz, 12H, **d**). ^{13}C NMR (100 MHz, DMSO-d_6) δ 58.05 (**a**), 23.56 (**b**), 19.70 (**c**), 14.00 (**d**). (DMSO) λ_{max} [nm] (ε/M^{-1} cm^{-1}): 327 (5 178). IR (cm^{-1}): 2961s, 2929m, 2872m ν(C-H stretch), 1483s,1380ss ν(C-H bending). HRMS (m/z): $[M]^+$ calculated for $[C_{16}H_{36}N]$: 242.53 amu; found: 242.28 amu.

Crystal Data for $C_{16}H_{36}AuCl_4N$ (M = 581.22 g/mol): monoclinic, space group $P2_1/n$ (no. 14), a = 14.7743(7) Å, b = 8.8213(5) Å, c = 18.1408(12) Å, β = 107.079(2)°, V = 2260.0(2) $Å^3$, Z = 4, T = 173.15 K, μ(MoKα) = 6.980 mm^{-1}, *Dcalc* = 1.708 g/cm^3, 14522 reflections measured (4.22° ≤ 2Θ ≤ 55.994°), 5428 unique (R_{int} = 0.0507, R_{sigma} = 0.0748) which were used in all calculations. The final R_1 was 0.0266 (I > 2σ(I)) and wR_2 was 0.0416 (all data).

2.4. Synthesis and Characterization of Metal Chelates

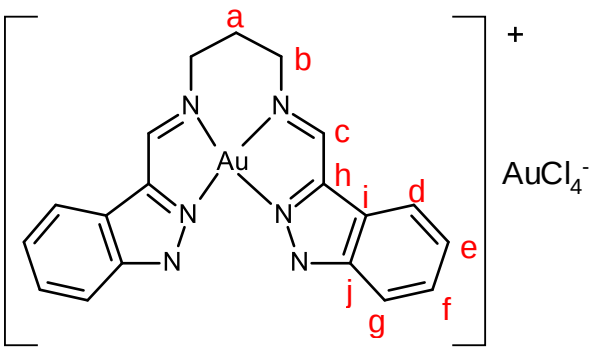

[Au(PrmeIndz)]$AuCl_4$

(*E*)-1-(indazol-3-yl)-N-[3-[(*E*)-indazol-3-ylmethyleneamino]propyl]methanimine gold(III) tetrachloroaurate ([Au(PrIndz)]$AuCl_4$). H_2PrIndz (0.4366 g, 1.322 mmol), [Bu_4N][$AuCl_4$] (0.7609 g, 1.309 mmol) and tertbutylammonium hexaflourophosphate (1.023 g, 2.641 mmol) were ground together for about ten minutes in a warm pestle and mortar. Ethanol (20 mL) was then added to the homogenous powder and the solution was stirred for two hours in a 50 mL round bottom flask. The solution formed an orange precipitate after five minutes. After two hours the product was filtered out and it was recrystallized with acetonitrile which resulted in crystalline red needles (isolated mass: 0.2601 g, yield: 23%).

^{1}H NMR (400 MHz, DMSO-d_6) δ 9.19 (d, J = 1.6 Hz, 2H, **c**), 8.19 – 8.09 (m, 2H, **g**), 8.06 – 7.96 (m, 2H, **d**), 7.53 – 7.42 (m, 4H, **f** and **e**), 4.02 – 3.95 (m, 4H, **b**), 2.44 (t, J = 5.1 Hz, 2H, **a**). ^{13}C NMR (100 MHz, DMSO-d_6) δ 163.44 (**c**), 148.80 (**i**), 139.25 (**j**), 127.87 (**e**), 126.71 (**f**), 123.92 (**g**), 120.57 (**k**), 119.53(**d**), 53.37 (**b**), 30.94 (**a**). IR (cm^{-1}): 3014br ν(CH_2), 1571s ν(N=C), 1332m ν(C=C). UV-vis: (DMSO) λ_{max} [nm] (ε/M^{-1} cm^{-1}): 317 (15 136), 415 (7 318).

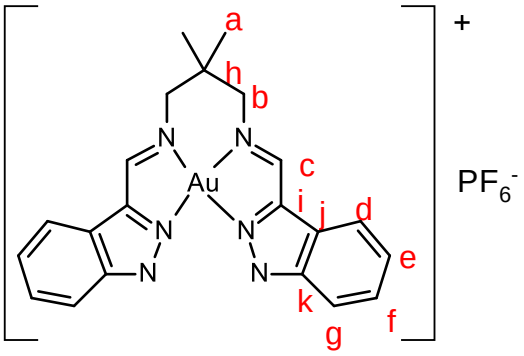

[Au(Prme$_2$Indz)]PF$_6$

(*E*)-1-(indazol-3-yl)-N-[3-[(*E*)-indazol-3-ylmethyleneamino]-2,2-dimethylpropyl]methan-imine gold (III) hexaflurophosphate ([Au(PrMe$_2$Indz)]PF$_6$). H_2PrMe_2Indz (0.1077 g, 0.3005 mmol), $[Bu_4N][AuCl_4]$ (0.1750 g, 0.3011 mmol) and tertbutylammonium hexaflourophosphate (0.1162 g, 0.3000 mmol) were ground together for about ten minutes in a warm pestle and mortar. Ethanol (20 mL) was then added to the homogenous powder, transferred to a 50 mL round bottom flask and it was stirred for two hours. The solution formed an orange precipitate after five minutes. After two hours the product was filtered out and it was recrystallized with acetonitrile which resulted in tiny fiber-like crystals. Bigger crystals were grown using the liquid-liquid diffusion method with two solvents, namely: DMF: diethyl ether. Alternatively, the product was washed with DCM to remove the tetrachloroaurate that forms as a by-product until the DCM appears clear (about six times) (isolated mass: 0.05453 g, yield: 26%).

^{1}H NMR (400 MHz, DMSO-d_6) δ 9.17 (s, 2H, **c**), 8.19 – 8.13 (m, 2H, **g**), 8.06 – 7.99 (m, 2H, **d**), 7.53 – 7.49 (m, 2H, **f**), 7.48 (d, J = 3.0 Hz, 2H, **e**), 3.72 (s, 4H, **b**), 1.24 (s, 1H, **a**).^{13}C NMR (100 MHz, DMSO-d_6) δ 164.46 (**c**), 148.76 (**k**), 139.23 (**i**), 127.97 (**e**), 126.73 (**f**), 123.97 (**g**), 120.60 (**j**), 119.57 (**d**), 62.82 (**b**), 40.55 (**h**), 23.59 (**a**). IR (cm^{-1}): 2965br ν(CH_2, CH_3), 1569s ν(N=C) 1429m ν(C=C), 827vs ν(PF_6). UV-vis: (DMSO) λ_{max} [nm] (ε/M^{-1} cm^{-1}): 270 (33 922), 327 (18 979), 414 (10 964). HRMS (m/z): $[M]^+$ calculated for $[C_{21}H_{20}N_6Au]$: 553.39 amu; found: 553.14 amu.

Crystal Data for: $C_{23}H_{23}AuF_6N_7P$ (M = 739.42 g/mol): triclinic, space group P-1 (no. 2), a = 6.4966(5) Å, b = 13.4032(10) Å, c = 14.3029(10) Å, α = 79.251(2)°, β = 86.872(2)°, γ = 87.361(2)°, V = 1220.94(16) Å^3, Z = 2, T = 173.15 K, μ(MoKα) = 6.165 mm^{-1}, *Dcalc* = 2.011 g/cm^3, 35136 reflections measured (6.284° ≤ 2Θ ≤ 57.672°), 6332 unique (R_{int} = 0.0716, R_{sigma} = 0.0601) which were used in all calculations. The final R_1 was 0.0343 (I > 2σ(I)) and wR_2 was 0.0607 (all data).

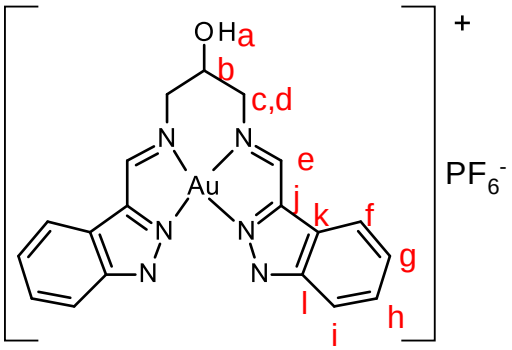

[Au(PrOHIndz)]PF_6

1,3-bis[(*E*)-1H-indazol-3-ylmethyleneamino]propan-2-ol gold(III) hexaflurophosphate ([Au(PrOHIndz)]PF_6). H_2PrOHIndz (0.1006 g, 0.2904 mmol) was ground with [Bu_4N][$AuCl_4$] (0.1673 g, 0.2878 mmol) and tertbutylammonium hexaflourophosphate (0.1160 g, 0.2994 mmol) in a pestle and mortar for 10 minutes. Ethanol (20 mL) was added. The solution was transferred into a 50 mL round bottom flask before being stirred at ambient temperature for three hours. Afterward, the product was filtered followed by five minutes of centrifugation in DCM. Centrifugation was repeated several times until the DCM solution became clear. The DCM solution was then removed and the product was left to dry in the air (isolated mass: 0.06120 g, yield: 31%).

^{1}H NMR (400 MHz, DMSO-d_6) δ 9.29 (s, 2H, **e**), 8.19 – 8.11 (m, 2H, **l**), 8.03 (ddd, *J* = 6.9, 3.6, 2.1 Hz, 2H, **f**), 7.49 (dt, *J* = 6.4, 3.5 Hz, 2H, **g,h**), 5.92 (d, *J* = 5.4 Hz, 1H, **b**), 4.66 (q, *J* = 5.7 Hz, 1H, **a**), 4.08 (d, *J* = 14.7 Hz, 4H,**c,d**). ^{13}C NMR (100 MHz, DMSO-d_6) δ 165.03 (**e**), 148.83 (**l**), 139.25 (**j**), 128.06 (**g**), 126.79 (**h**), 123.91 (**i**), 120.63 (**k**), 119.55 (**f**), 69.38 (**b**), 57.48 (**c,d**). IR (cm-1): 3641br ν(O-H), 3571w ν(C-$H_{aromatic}$), 3033w ν(CH_2, CH_3), 1550s ν(C=N), 1434m ν(C=C), 833vs ν(PF_6). UV-vis: (DMSO) λ_{max} [nm] (ε/M^{-1} cm^{-1}): 271 (30 908), 328(17 995), 414 (10 092). HRMS (m/z): $[M]^+$ calculated for [$C_{19}H_{16}N_6OAu$]: 541.34 amu; found: 541.10 amu.

Crystal Data for: $C_{21}H_{22}AuF_6N_6O_2P$ (*M* = 764.44 g/mol): monoclinic, space group $P2_1$ (no. 4), *a* = 13.7818(5) Å, *b* = 6.6345(3) Å, *c* = 16.3299(6) Å, *β* = 107.382(2)°, *V* = 1424.95(10) $Å^3$, *Z* = 2, *T* = 173.15 K, μ(MoKα) = 5.360 mm^{-1}, *Dcalc* = 1.782 g/cm^3, 21443 reflections measured (3.096° ≤ 2Θ ≤ 56.53°), 7060 unique (R_{int} = 0.0849, R_{sigma} = 0.1003) which were used in all calculations. The final R_1 was 0.0644 (I > 2σ(I)) and wR_2 was 0.1838 (all data).

2.5. DFT simulations

All the DFT-calculations of Au(III) chelates were performed using GuassView 6.0 as the interface to Gaussian 16W. The X-ray coordinates were used as input structures in all cases and geometry optimization was carried out at HSEHIPBE[4]/SDD[5] level of theory. The output file was then used to calculate the vibrations (IR), NMR and electronic transitions using the same level of theory used for geometry optimization. The NMR spectra were calculated using DMSO as a model solvent. Electronic transitions were calculated using the TD-SCF[6] method, with the same level of the theory mentioned above, this was done for 60 excited states.

2.6. References

(1) Dolomanov, O.V., Bourhis, L.J., Gildea, R.J., Howard, J.A. and Puschmann, H., 2009. OLEX2: a complete structure solution, refinement and analysis program. *Journal of Applied Crystallography*, 42(2), pp.339-341.

(2) Sheldrick, G.M., 2015. SHELXT–Integrated space-group and crystal-structure determination. *Acta Crystallographica Section A: Foundations and Advances*, 71(1), pp.3-8.

(3) Sheldrick, G.M., 2015. Crystal structure refinement with SHELXL. *Acta Crystallographica Section C: Structural Chemistry*, 71(1), pp.3-8.

(4) Heyd, J. and Scuseria, G.E., 2004. Efficient hybrid density functional calculations in solids: Assessment of the Heyd–Scuseria–Ernzerhof screened Coulomb hybrid functional. *The Journal of Chemical Physics*, *121*(3), pp.1187-1192.

(5) Fuentealba, P., Preuss, H., Stoll, H. and Von Szentpaly, L., 1982. A proper account of core-polarization with pseudopotentials: single valence-electron alkali compounds. *Chemical Physics Letters*, *89*(5), pp.418-422.

(6) Bauernschmitt, R. and Ahlrichs, R., 1996. Treatment of electronic excitations within the adiabatic approximation of time dependent density functional theory. *Chemical Physics Letters*, *256*(4-5), pp.454-464.

Chapter 3

Synthesis and Spectroscopic Characterization

3.1. Synthesis

Bis(indazole-imine) ligands and chelates synthesized in this project are novel and add to the existing library of potential chemotherapeutic agents. The ligand scaffold consists of two indazole rings connected through different alkyl chains. The ligand formation occurs through a condensation reaction between a carbonyl compound (which is an aldehyde in this case) and various primary imines. This reaction was invented by Hugo Schiff in 1864 and its mechanism is well understood and has been studied extensively.[1,2] All the reaction steps are reversible as shown in Scheme 1. It is, therefore, possible to form a library of these type of ligands if different combinations of carbonyl compounds and primary amines are utilized as starting materials under thermodynamically regulated conditions.[1]

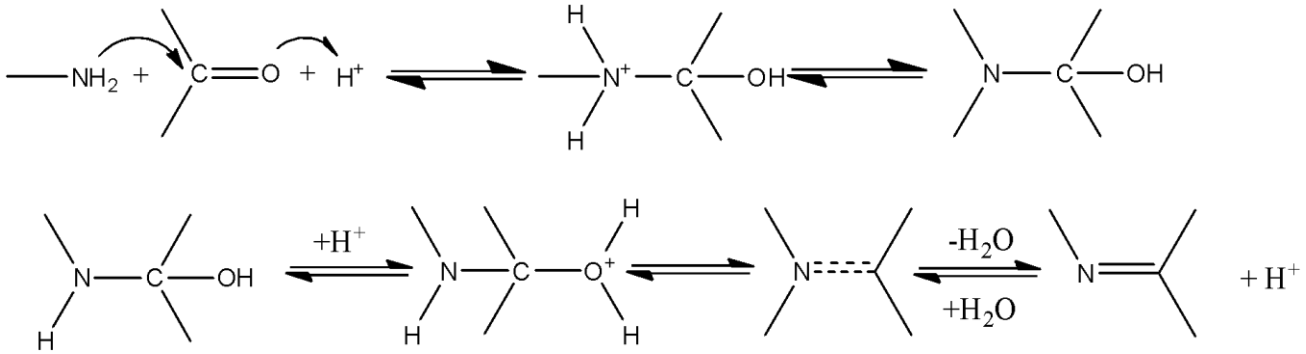

Scheme 1: Condensation mechanism of carbonyl compounds with primary amines.[1,2]

Four bis(indazole-imine) ligands are reported in this project. Their structures are varied by changing the substituent on the alkyl bridge as well as the length of the dimethyl chain. Complexation of these ligands to Au(III) occurs through deprotonation of two indazole N protons giving stable mono-cationic, square planar Au(III) chelates with a 1:1 metal-ligand ratio.[3] Such tetradentate Schiff base ligands have been reported to be well suited to undergo chelation with square planar and octahedral metals such as Co(II), Mn(II), Fe(III), Ni(II), and Pd(II).[3–5]

The Au(III) chelates of interest are very similar to previously synthesized Au(III) tetraarylporphyrins, bis(pyrrolide-imine) Au(III) chelates, and bis(pyrrolide-imine) macrocycles which are also primarily based on dianionic tetradentate ligands.[6–8] These compounds have proved to be cytotoxic to a variety of human cancer cell lines. They also have similar activity to cisplatin which has been in clinical use for several decades.

Their advantage, however, is that they are novel and due to their electron-rich indazole rings, they can stabilize the high-oxidation state Au(III) cation, thus preventing its reduction under physiological conditions. They are therefore suitable to serve as investigational metallodrugs.

The goal of this project is to expand the library of square-planar d^8 Au(III) chelates by developing bis(indazole-imine) ligands that will complex and stabilize Au(III). These compounds will potentially serve as DNA intercalators with an innate ability to disrupt the function of DNA topoisomerases. The compounds can then be further studied as preclinical investigational chemotherapeutic agents. This chapter, therefore, focuses on synthetic techniques employed to generate these ligands and their corresponding Au(III) chelates.

3.1.1. Synthesis of bis(indazole-imine) ligands

Four bis(indazole-imine) ligands were synthesized in this project; three of them were obtained by employing a solid-state reaction (the grinding method, Scheme 2) using a pestle and mortar. The n-propyl bridged ligand was obtained by a reflux reaction under nitrogen gas.

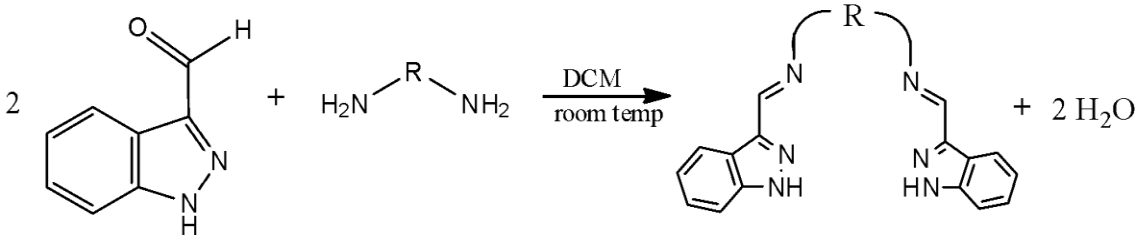

R = $CH_2(H_3)_2CH_2$ (H_2PrMe_2Indz),

$CH_2CHOHCH_2$ ($H_2PrOHIndz$),

$CH_2(CH_2)_2CH_2$ ($H_2BuIndz$)

Scheme 2: Grinding method carried out at room temperature using DCM as a solvent.

The *n*-propyl-bridged ligand ($H_2PrMeIndz$) was obtained through a reflux reaction under nitrogen gas at 78 °C (Scheme 3). The reaction involved adding 1H-indazole-3-carboxaldehyde, 1,3-diamino propane and approximately two full spatula spoons of magnesium sulphate ($MgSO_4$) into a 100 mL round-bottomed flask. $MgSO_4$ helped to drive the reaction forward by removing water. Ethanol (20 mL) was then added to the mixture which was refluxed for three hours. The reaction mixture was then allowed to cool and $MgSO_4$ was removed by suction filtration. The product was isolated as a fluffy yellowish powder by rotary evaporation of the solvent. This product displayed light sensitivity when exposed to light; its colour changed from yellowish to greenish colour.

Storage of the compound in the dark at room temperature with the screw-cap bottle sealed in aluminum foil was necessary to prevent photochemical degradation of the compound. This is the only ligand that was prepared by a conventional (non-mechanochemical) method.

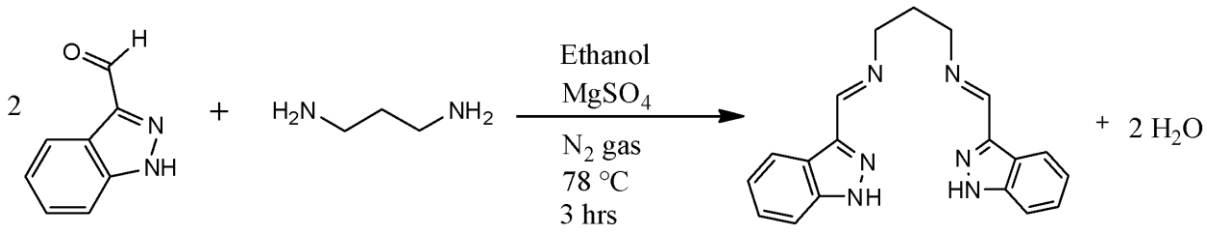

Scheme 3: Synthesis of the n-propyl-bridged ligand (H_2PrmeIndz) at 78 °C under N_2 gas, with the presence of $MgSO_4$ to remove water and drive the reaction forward.

The other three ligands (2, 2-dimethyl propyl, 2-hydroxypropyl and n-butyl) were prepared similarly using the grinding method with slightly different isolation of ligands.

For the 2,2-dimethylpropyl-bridged ligand (H_2PrMe$_2$Indz), the solution turned cloudy in less than 5 minutes of stirring; it then precipitated completely out of the solvent after about 15 minutes. The solvent was then removed by filtration to obtain a white fine powder product with a high yield. The other two ligands, H_2PrOHIndz and H_2BuIndz) did not precipitate out after the addition of a solvent. They were therefore isolated by removing the solvent by rotary evaporation which resulted in the formation of a spongy solid that became powdery when scraped out of the flask. The resulting products were both white fluffy powders which were also isolated in high yields.

In this work, successful mechanochemical synthesis of three ligands repeatedly afforded high yield products compared to traditional synthesis such as refluxing of the reagents which were also attempted. Similar observations are documented in the literature, where mechanochemical reactions were run at room temperature. For instance, the synthesis of related tetradentate Schiff-base ligands such as salophen ((N,N-phenylene-bis(salicylimine)) and salen (N,N-bis(salicylidene) ethylenediamine) by mechanochemistry gave relatively high yields, between 60% and 70% through milling at room temperature.[9] Mechanical synthesis, however, did not work well with the *n*-propyl analog as it did not produce the desired product. The grinding method is, nonetheless, most appreciated in this work because it uses a small amount of solvent in the reaction; it is carried out at room temperature and it takes a shorter period to complete. It is, therefore, energy, time and resource-efficient.

3.1.2. Metallation of ligands

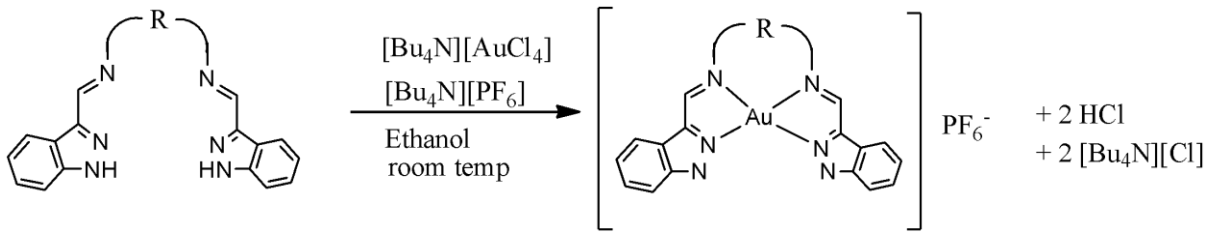

R = $CH_2CH_2CH_2$ (H_2PrIndz),

$CH_2C(H_3)_2CH_2$ (H_2PrMe$_2$Indz),

$CH_2CHOHCH_2$ (H_2PrOHIndz),

$CH_2(CH_2)_2CH_2$ (H_2BuIndz)

Scheme 4: Metallation of the bis(indazole-imine) ligands with a suitably reactive Au(III) salt at room temperature using a solid-state reaction.

Metallation of the bis(indazole-imine) ligands depicted in Scheme 2 was achieved using tetrabutylammonium tetrachloroaurate(III), $[Bu_4N][AuCl_4]$, as a reactive Au(III) salt. This is a yellow, non-hygroscopic lipophilic powder that is very stable under atmospheric conditions. The chosen Au(III) salt is resistant to reduction and its synthesis is quick and straightforward.

The chosen Au(III) salt is stable and it prevents the formation of unwanted counter ions: $[AuCl_2]^-$ and $[AuCl_4]^-$. These counterions, however, are formed during metallation of the *n*-propyl bridged ligand (the discussion to follow). The salt's pH neutrality would also be expected to interfere minimally with ligand deprotonation (indazole NH groups), which is required for the chelation of the Au(III) ion to form a monocationic product salt. An acidic Au(III) salt such as $HAuCl_4$ introduces the acidic environment that can interfere with complexation.[10]

All the bis(indazole-imine) Au(III) chelates in this work were synthesized by a solid-state reaction mentioned in Section 3.1. This method involved grinding one mole equivalent of each: ligand, Au(III) salt, and tetrabutylammonium hexafluorophosphate(V) altogether for about 10 minutes in a warm pestle and mortar.

The presence of all these reagents is crucial for the reaction to proceed forward. Removal of either of them would interfere with the formation of the desired product. Carrying out this reaction with any other solvent (like DCM, acetonitrile) except ethanol gives no product neither does using ethanol without PF_6^- give a product, as it was attempted in this work and an undesired and insoluble product was obtained.

The result is a homogeneous fine yellow power shown in Figure 3.1a below. Ethanol was added to the homogenous powder and the solution was stirred for two hours. The mixture turned from yellow to an orange precipitate after five minutes. At the end of two hours, the precipitate was filtered off, dried in air and recrystallized with acetonitrile. The crystals formed were orange microfiber crystals (Figure 3.1b).

The above method was very straightforward for the dimethyl- and the hydroxy-bridged Au(III) chelates, [Au(PrMe$_2$Indz)]PF$_6$ and [Au(PrOHIndz)]PF$_6$, respectively. Another way to separate the product from the solvent was through centrifugation of the chelate solution, rinsing with DCM about six times to make sure that the product is completely clean. DCM was used because it is an organic solvent and it can easily extract the unreacted and the by-product lipophilic Au(III) salt completely from the product. This method gave a clean product with a high yield. Bigger crystals were grown using the liquid-liquid diffusion method: DMF: diethyl ether.



a b

Figure 3.1: a) Photograph of the homogenous yellow powder formed after grinding the starting materials using a pestle and mortar. b) Photograph of the orange fiber-like crystals of one of the Au(III) bis(indazolide-imine) chelates in a crystallization tube.

In this work, only two chelated Au(III) salts were successfully made in which the desired counterion (PF_6^-) was present. These were the dimethyl- and the hydroxy-bridged Au(III) chelates, [Au(PrMe$_2$Indz)]PF$_6$ and [Au(PrOHIndz)]PF$_6$, respectively. The X-ray structures of both these compounds were obtained and proved that they both contained PF_6^- as a counter ion. Both Au(III) chelates dissolve completely in DMSO and DMF and have partial solubility in acetonitrile. When heated in acetonitrile, the complexes were obtained as fine orange crystalline powder (Figure 3.2a).



a b

Figure 3.2: a) Photograph of the fine orange crystalline powder of a typical [Au(L)][PF_6] salt, where L = bis(indazolide-imine), after recrystallization in acetonitrile. b) Photograph of a crystalline red powder of the propyl-bridged Au(III) chelate with the undesirable $[AuCl_4]^-$ counterion, [Au(PrIndz)][$AuCl_4$].

The synthesis of the *n*-propyl-bridged chelate $[Au(PrIndz)]^+$ although successful, yielded either $[AuCl_2]^-$ or $[AuCl_4]^-$ counterions depending on the synthetic step. The $[AuCl_4]^-$ counterion, for instance, formed when the ligand, Au(III) salt, and [Bu_4N][PF_6] were ground together, stirred for two hours in ethanol, then filtered and dried. The product was an orange powder with high impurities and low solubility in most solvents which made it difficult to characterize as it could no dissolve in any solvent (the characterization techniques, NMR, MS and Uv-vis require that the compound be dissolved before analysis). The product was recrystallized in hot acetonitrile and a red-crystalline power was obtained (shown in Figure 3.2b). Crystallization of this powder gave rise to a propyl-bridged Au(III) chelate with $[AuCl_4]^-$ counterion instead (Scheme 5).

As an attempt to resolve this problem, the Au(III) chelate was reacted with tertbutyl ammonium chloride [Bu_4N]Cl in the presence of DCM to change the $[AuCl_4]^-$ counter ion to chloride (Cl^-) counterion (Scheme 5). The logic behind this idea was that [Bu_4N]Cl would dissociate into $[Bu_4N]^+$ and Cl^- when reacted with the chelate. The $[AuCl_4]^-$ ion from the chelate would then readily electrostatically associate with $[Bu_4N]^+$ to form [Bu_4N][$AuCl_4$] (which can be isolated easily, through crystalization), leaving the Cl^- to associate with the metal chelate to form an Au(III) chelate charge-balanced with a biologically compatible Cl^- counterion.

This reaction, however, yielded an Au(III) chelate with $[AuCl_2]^-$ instead of the Cl^- counterion. See Scheme 5 below. This was proven by a crystal structure.

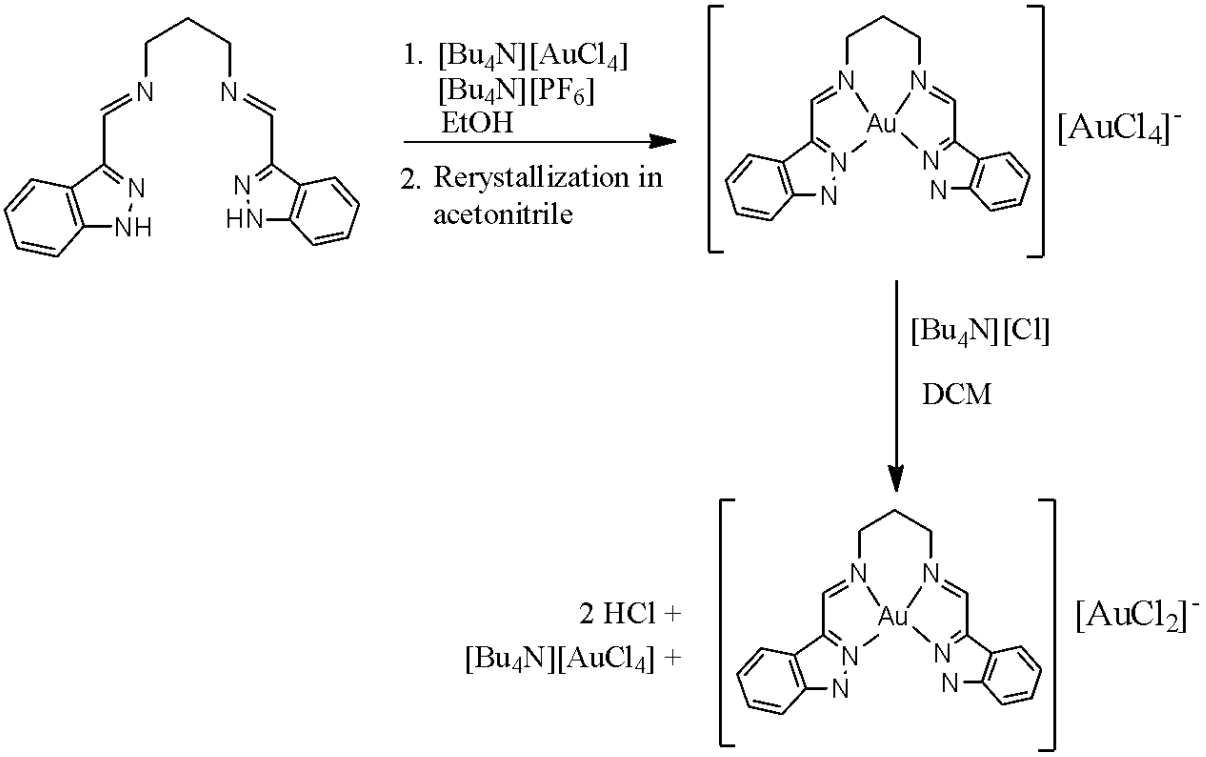

Scheme 5: Attempts to synthesize Au(III) chelates of the propyl-bridged ligand with either PF_6^- or Cl^- counterions. Reactions typically afforded $[AuCl_4]^-$ and $[AuCl_2]^-$ salts of the Au(III) chelate.

The synthesis of the *n*-butyl-bridged Au(III) chelate, $[Au(BuIndz)]^+$, was the most challenging in this work. The grinding method was first used following the same synthetic route used for the synthesis of other successful chelates. The product, however, was very insoluble, highly impure and therefore difficult to characterize. The product could only dissolve in hot DMSO or DMF. The synthesis of $[Au(BuIndz)]^+$ in this case was, therefore, unsuccessful.

A different method was then used which involved dissolving the ligand in ethanol first and preparing a mixture of $[Bu_4N][PF_6]$ and $[Bu_4N][AuCl_4]$ in a separate flask using DCM. This mixture was added to the ligand solution dropwise.

The solution was then refluxed for one hour and a red precipitate formed. The precipitate was then filtered and allowed to dry. Characterization of the solid by NMR produced complicated spectra and this thus indicated that the synthesis was also unsuccessful. Future efforts to prepare this compound would presumably require the use of a different Au(III) precursor.

Though not required for initial complexation of a metal ion by the bis(indazole-imine) Schiff base, it may also be necessary to explore the use of a mild base to assist deprotonation of the indazole NH groups, thereby enhancing the nucleophilicity of the tetradentate ligand and improving the probability of chelate formation.

3.2. Spectroscopic characterization

3.2.1. IR spectroscopy: Results and discussion

The IR spectroscopy results indicate a successful synthesis of bis(indazole-imine) ligands as well as their corresponding Au(III) metal chelates, this can be observed through characteristic signals for both the ligand and Au(III) chelate spectra. Superimposed IR spectra of H_2PrMe_2Indz and $[Au(PrMe_2Indz)]PF_6$ as well as $H_2PrOHIndz$ and $[Au(PrOHIndz)]PF_6$ are shown in Figure 3.3 and 3.4 below. These compounds were successfully synthesized in this work and are used as representative examples of bis(indazole-imine) ligands and bis(indazolide-imine) Au(III) chelates.

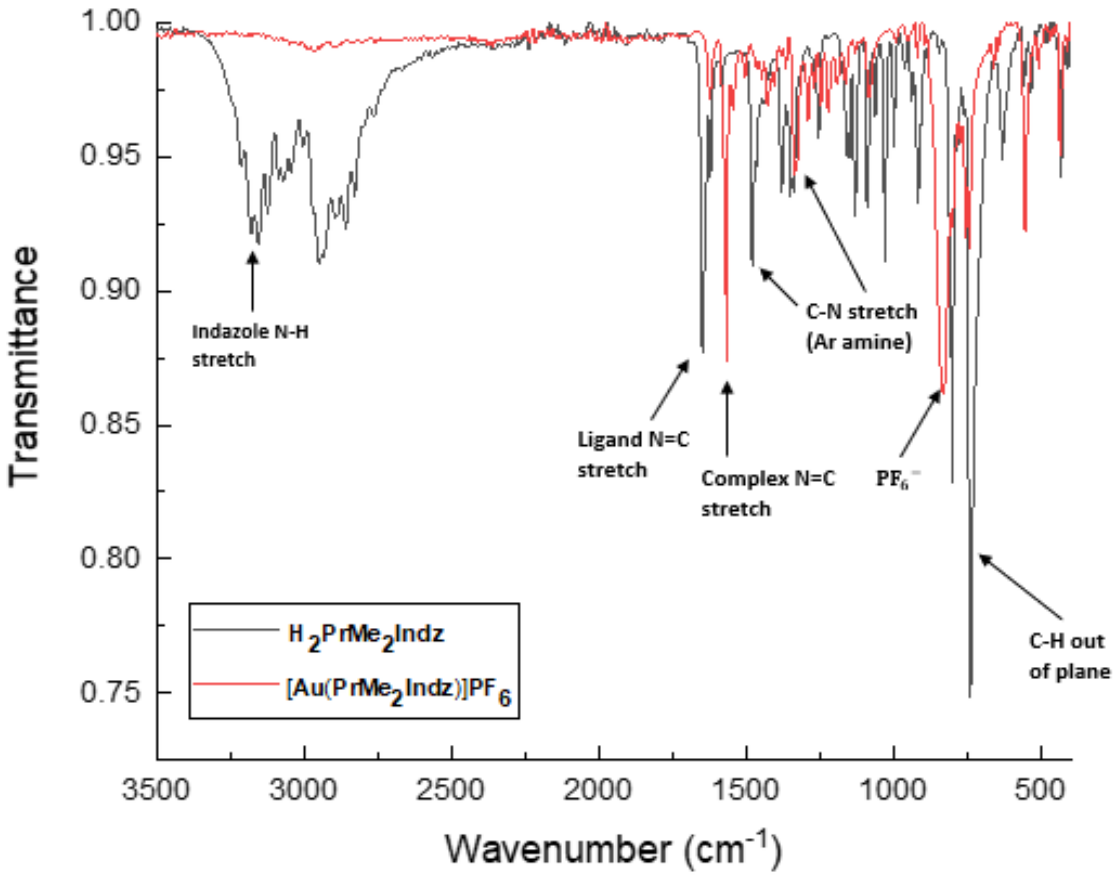

Figure 3.3. Superimposed IR spectra of H_2PrMe_2Indz and $[Au(PrMe_2Indz)]PF_6$ indicating their characteristic signals which prove their successful synthesis.

The most distinguishable signal in the ligand's spectrum is the NH stretch signal which is usually a broad stretch found in the 3300-3500 cm^{-1} region of the IR. This signal is observed at around 3123 cm^{-1} and 3179 cm^{-1} in the H_2PrMe_2Indz and $H_2PrOHIndz$ IR spectra, respectively. As anticipated, this signal disappears in both the Au(III) chelate spectra. This is due to the concomitant deprotonation of two indazole NH protons during metal chelation. The Au(III) chelate, therefore, does not contain indazole NH protons, consistent with the ligand chelating the metal ion as a dianion. It is a very good indication of successful Au(III) chelation into the ligand. Table 3.1 below indicates the NH stretching frequencies of all the bis(indazole-imine) ligands synthesized in this work. These signals differ due to varying substituents on each ligands' diamine bridge.

Table 3.1. NH and C=N stretching frequencies for bis(indazole-imine) ligands.

Ligand	NH stretch (cm^{-1})	C=N stretch (cm^{-1})
$H_2PrIndz$	3175	1644
H_2PrMe_2Indz	3123	1650
$H_2ButIndz$	3177	1643
$H_2PrOHIndz$	3179	1646

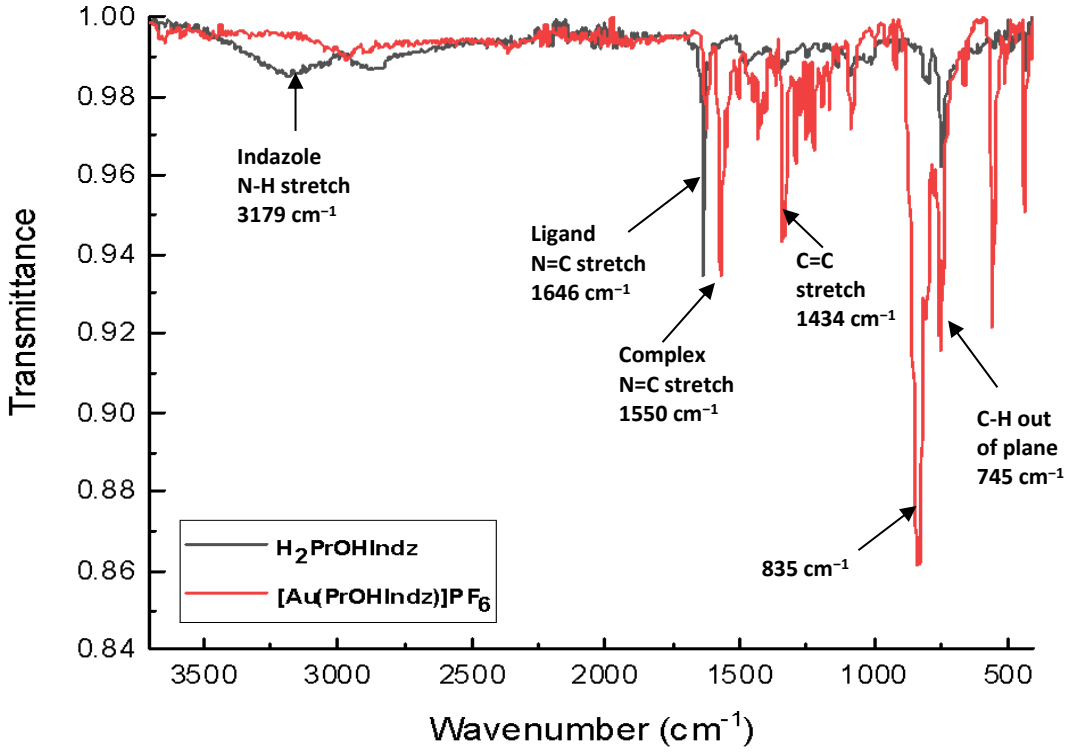

Figure 3.4: Superimposed IR spectra of $H_2PrOHIndz$ and $[Au(PrOHIndz)]PF_6$ indicating characteristic signals which prove their successful synthesis.

Another distinguishable signal is the imine C=N stretch which is usually found at around 1690-1640 cm^{-1} range in the IR region. During metal chelation, this signal is expected to undergo a significant spectral shift, towards lower energy, as the bonds weaken when the Au(III) ion back-donates electron density into the π^* MO of the C=N bond, thereby reducing the C-N bond order. For H_2PrMe_2Indz and $[Au(PrMe_2Indz)]PF_6$ as anticipated, the C=N signals are observed at 1650 cm^{-1} and 1569 cm^{-1}, respectively. The same trend is observed for $H_2PrOHIndz$ and $[Au(PrOHIndz)]PF_6$. This means that the π * orbitals are low enough in energy for the ligand to act as a π -acid.

Table 3.2 below compares the IR C=N stretch and C=C stretch of the Au(III) chelates reported in this work together with their respective ligands to one of the literature reported macrocyclic pyrrole type Au(III) chelate together with its corresponding macrocyclic ligand. Figure 3.5 below shows the pyrrole-type macrocyclic ligand and Au(III) chelate comparable to bis(indazole-imine) ligands and Au(III) chelates reported in this work.

Table 3.2: C=N and C=C stretching frequencies of bis(indazole-imine) ligands and Au(III) chelates compared with data for macrocyclic bis(pyrrolide-imine) ligands and Au(III) chelates.

Compound	C=N stretch (cm^{-1})	C=C stretch (cm^{-1})
H_2PrMe_2Indz	1650	1481
$[Au(PrMe_2Indz)]PF_6$	1569	1429
$H_2PrOHIndz$	1646	1476
$[Au(PrOHIndz)]PF_6$	1550	1434
	Literature	
Compound 5c	1650	1438
Compound 5	1573	1396

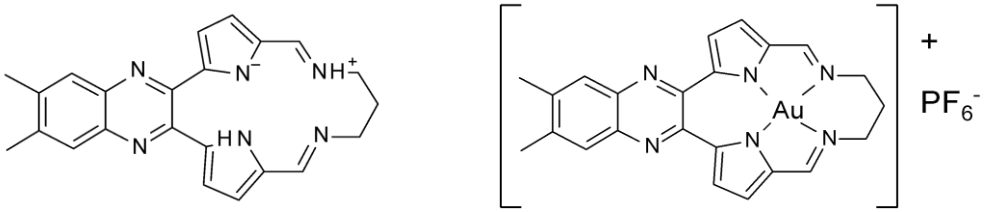

Compound 5c Compound 5

Figure 3.5: A pyrrole-type macrocyclic ligand and Au(III) chelate comparable to bis(indazole-imine) ligands and Au(III) chelates reported in this work.[6]

3.2.2. Results and discussion: UV-vis spectroscopy

The electronic spectra of H_2PrMe_2Indz and $[Au(PrMe_2Indz)]PF_6$ are shown in Figure 3.6 below as representative examples of bis(indazole-imine) ligands and Au(III) chelates. Both ligands and chelates have aromatic chromophores which are mainly dominated by $\pi \rightarrow \pi^*$ transitions and the spectra of which may be quite complex.

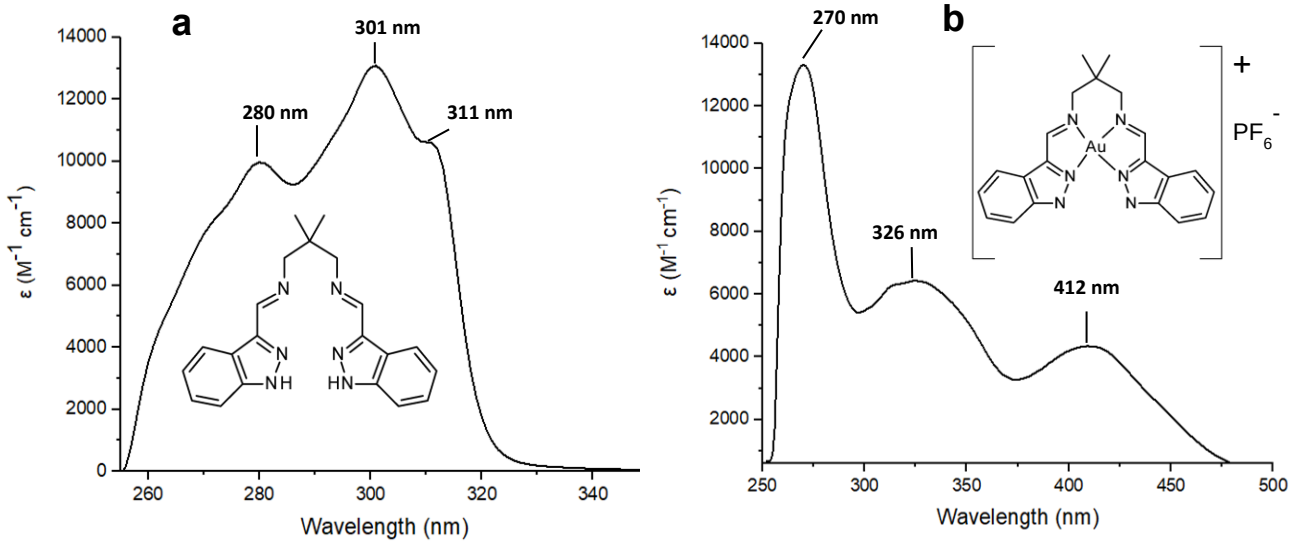

Figure 3.6: Electronic spectra of a) H_2PrMe_2Indz and b) $[Au(PrMe_2Indz)]PF_6$ in 10% DMSO-water at 298 K.

The electronic spectrum of H_2PrMe_2Indz has two resolved bands at 280 nm and 301 nm and a shoulder at 311 nm. The intensity of the most intense peak is $1.31 \times 10^4\,M^{-1}\,cm^{-1}$. Although this intensity differs from ligand to ligand, the basic shape of the spectrum and the position of the absorbance peaks are very similar to those of other ligands reported in this work, $H_2ButIndz$ and $H_2PrOHIndz$. $H_2PrOHIndz$, however, appears to have the highest intensity at 300 nm, $2.05 \times 10^4\ M^{-1}\,cm^{-1}$. $H_2PrmeIndz$, unlike other ligands, has two unresolved peaks in the 280 nm region, but all the other peaks are similar to those of other ligands. Table 3.3 below summarises the wavelengths and extinction coefficients of the ligands and chelates at their relevant absorption band maxima.

The synthesized Au(III) chelates in this work $[Au(PrMe_2Indz)]PF_6$ and $[Au(PrOHIndz)]PF_6$ appear to have very similar $\lambda_{max.}$ and overall, they have three resolved bands at 270, 326, and 412 nm. The first two bands at around 270 and 326 nm are attributed to $\pi \rightarrow \pi^*$ bands and the LMCT bands are at around 412 nm due to $\pi \rightarrow \sigma^*$ transitions. These results are consistent with the UV-vis results of reported Au(III) compounds.

DFT simulations were used to further the Au(III) complexes to compare simulated results with experimental results. This part is discussed more in Chapter 4. The basic spectral envelope predicted by DFT, however, is the same except that the three absorbance peaks are found at around 200 nm, 250 nm, and 350 nm.

Table 3.3: Wavelengths and extinction coefficients for absorption band maxima of bis(indazole-imine) ligands and Au(III) chelates at maximum absorbance peaks.

Ligand	λ_{max}/ nm (ε/M^{-1} cm^{-1})	λ_{max}/ nm (ε/M^{-1} cm^{-1})	λ_{max}/ nm (ε/M^{-1} cm^{-1})
H_2PrmeIndz	281 (1.46×10^4) 288 (1.41×10^4)	300 (1.21×10^4)	310 (9.74×10^4)
H_2PrMe_2Indz	280 (9.97×10^3)	301 (1.31×10^4)	311 (1.06×10^4)
H_2PrbutIndz	279 (1.63×10^4)	300 (1.97×10^4)	310 (1.63×10^4)
H_2PrOHIndz	280 (1.56×10^4)	300 (2.05×10^4)	310 (1.70×10^4)
Au(III) chelates			
[Au($PrMe_2$Indz)]PF_6	270 (1.33×10^4)	326 (6.43×10^4)	412 (4.35×10^3)
[Au(PrOHIndz)]PF_6	270 (2.93×10^4)	326 (1.57×10^4)	412 (9.52×10^3)

3.2.3. NMR - Results and discussion

NMR spectroscopy indicated that the chelation of Au(III) to the series of bis(indazole-imine) ligands was effectively complete with little evidence of unreacted free ligand present in the sample. A comparison of the NMR spectra of ligands and their corresponding Au(III) chelates confirms that metal chelation resulted in a significant downfield shift for several of the Au(III) chelates' ^{1}H NMR signals, as anticipated. Table 3.4 below gives a summary of ^{1}H NMR chemical shifts for H_2PrMe_2Indz and [Au($PrMe_2$Indz)]PF_6 as representatives of bis(indazole-imine) ligands and Au(III) chelates in this work. See Appendix A for the NMR spectra of [Au(PrOHIndz)]PF_6. The alphabetical assignments represent each magnetically distinct proton labeled on the compound structures shown in Figures 3.7 and 3.8.

Table 3.4: ^{1}H NMR chemical shifts (ppm) of H_2PrMe_2Indz and $[Au(PrMe_2Indz)]PF_6$ in DMSO at 300 K.

Proton	H_2PrMe_2Indz (ppm)	$[Au(PrMe_2Indz)]PF_6$ (ppm)
a	1.93-1.70	1.24
b	3.71	3.72
c	8.65	9.17
d	7.58	8.06-7.99
e	7.20	7.48
f	7.41	7.53-7.49
g	8.25	8.19-8.13
h	13.41	N/A

^{1}H NMR spectra of H_2PrMe_2Indz and $[Au(PrMe_2Indz)]PF_6$ are indicated in Figures 3.7 and 3.8 below. All the signals were assigned with the help of DFT. The DMSO (solvent) and water signals were detected at around 2.5 ppm and 3.4 ppm, respectively. The water signal is due to the hygroscopic behavior of the DMSO. As mentioned above, NMR signals of $[Au(PrMe_2Indz)]PF_6$ experienced a significant downfield shift due to Au(III) chelation to the ligand.

The phenyl NMR signals appear to have experienced a minor downfield shift, reflecting the fact that they are further away from the Au(III) ion in the molecular structure. The spectrum also indicates an overlap of signals e and f of the chelate phenyl group, and in general, the phenyl group signals are closer together in the chelate spectrum compared with the ligand NMR spectrum. The imine N=CH proton signal (c) exhibits the anticipated large downfield shift after the Au(III) chelation. This is consistent with polarization of the metal-bound imine group by the Au(III) ion and therefore reduced shielding of the imine CH proton.

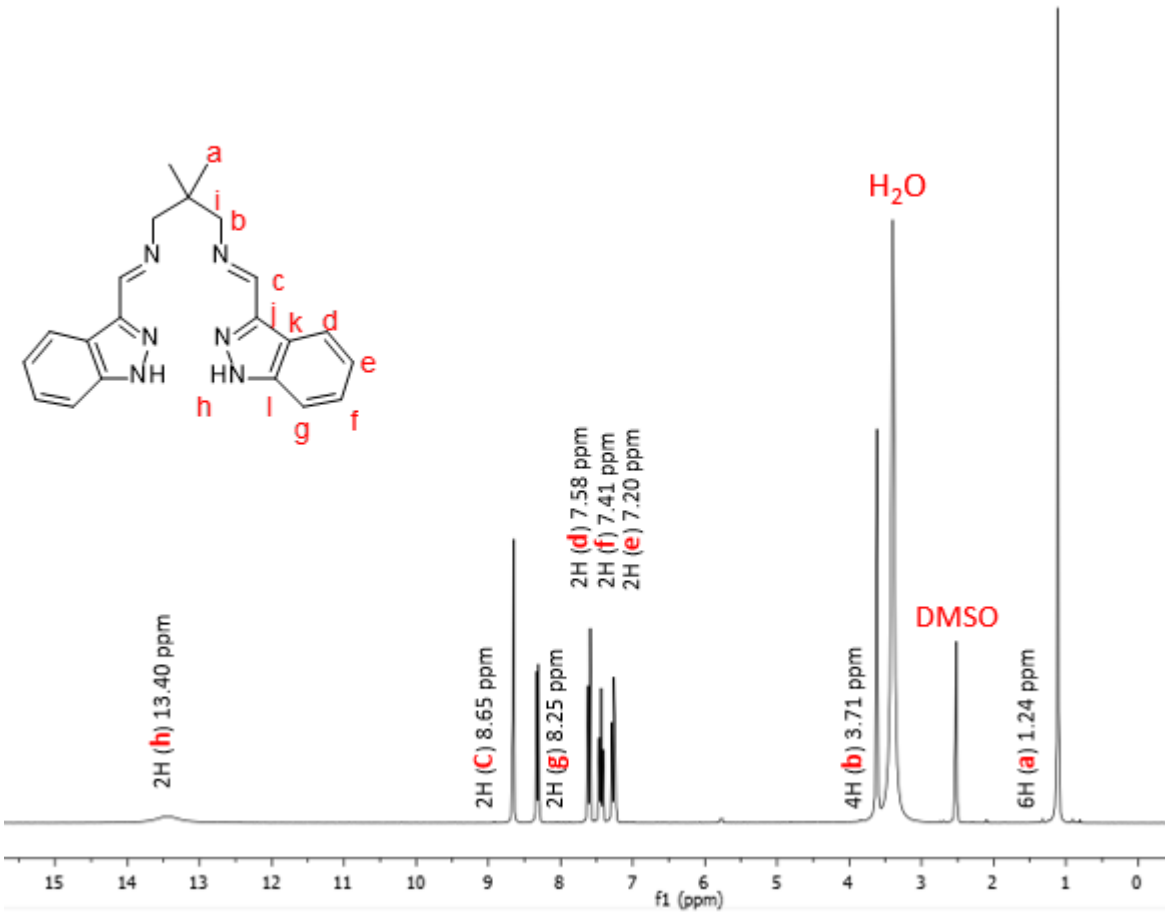

Figure 3.7: Assigned ^{1}H NMR spectrum of H_2PrMe_2Indz in DMSO at 300 K.

The disappearance of the NH signal (**h**) from the [Au($PrMe_2Indz$)]PF_6 spectrum at around 13.40 ppm (Figure 3.8) further confirms successful Au(III) chelation. This is because metal chelation occurs with concomitant deprotonation of two NH protons. Overall the results are consistent with literature results of reported macrocyclic bis(pyrrolide-imine) ligands and complexes.[6]

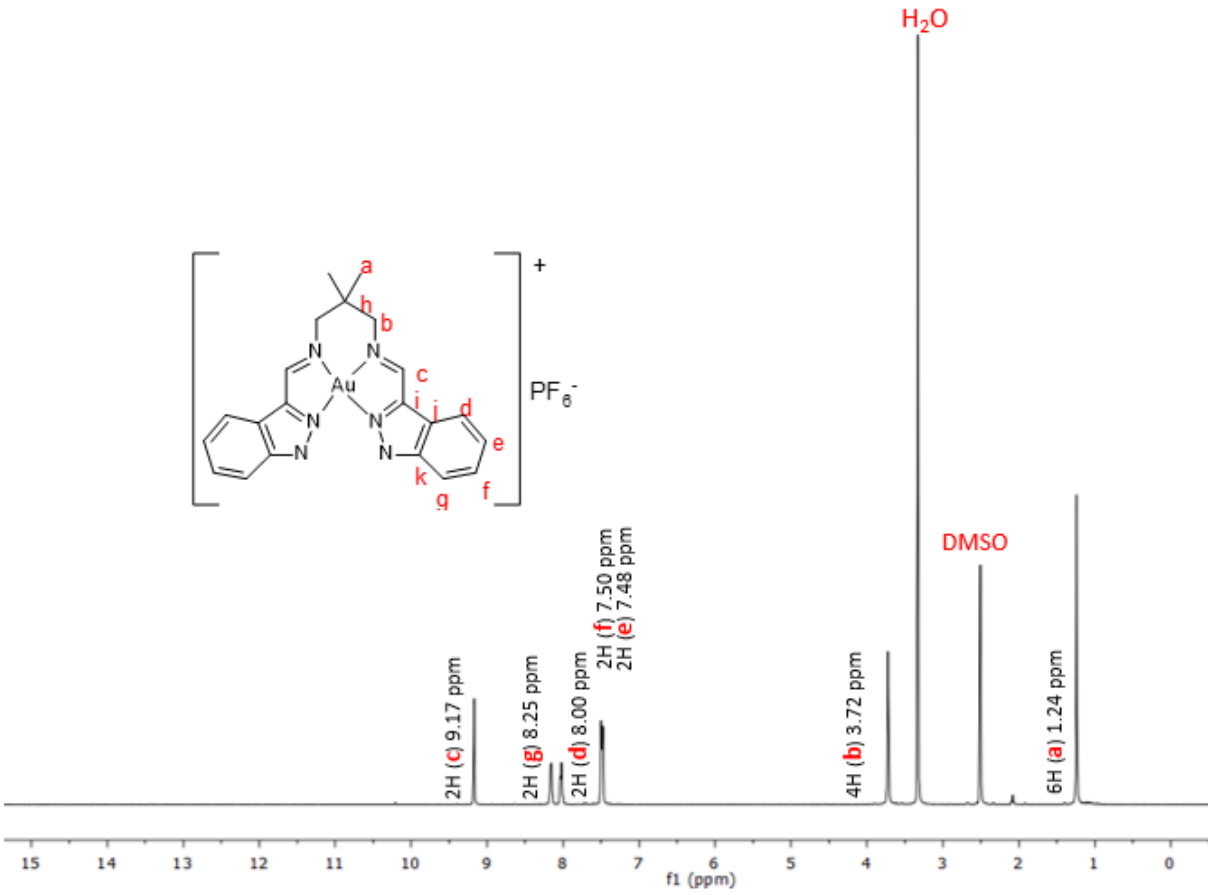

Figure 3.8: Assigned ^{1}H NMR spectrum of [Au(PrMe$_2$Indz)]PF$_6$ in DMSO at 300 K.

Table 3.5 below summarises ^{13}C NMR chemical shifts of H$_2$PrMe$_2$Indz and [Au(PrMe$_2$Indz)]PF$_6$. The results indicate an overall upfield shift of the [Au(PrMe$_2$Indz)]PF$_6$ signals relative to those of H$_2$PrMe$_2$Indz.

Table 3.5: ^{13}C NMR chemical shifts of H$_2$PrMe$_2$Indz and [Au(PrMe$_2$Indz)]PF$_6$ in DMSO at 300 K.

Carbon	H$_2$PrMe$_2$Indz (ppm)	[Au(PrMe$_2$Indz)]PF$_6$ (ppm)
a	36.34	23.59
h	48.52	N/A
b	81.98	62.83
d	122.41	119.59
j	132.69	120.61
g	133.37	123.98
f	134.16	126.74
e	138.70	127.98
i	153.21	139.24
k	154.45	148.78
c	168.27	164.48

Comparing the ^{13}C NMR spectra of H_2PrMe_2Indz and $[Au(PrMe_2Indz)]PF_6$ indicates that Au(III) chelation, as already shown by ^{1}H NMR spectroscopy, causes a significant shift for the $[Au(PrMe_2Indz)]PF_6$ NMR signals. Many of the ^{13}C NMR signals shift in the opposite direction (upfield, or to smaller chemical shifts). The largest upfield shifts are observed for the methyl and methylene carbon atoms in the alkyl bridge, whose nuclei show increased shieldings of ca. 12 and 17 ppm, respectively, upon chelation of Au(III). Regarding the ring carbons, the signal for carbon atom (**i**) within the indazole ring directly bound to the metal ion shows a ca. 13 ppm upfield shift upon metallation of ligand. This is the case with other Au(III) chelates reported in this work. Figures 3.9 and 3.10 below show the ^{13}C NMR spectra of H_2Prme_2Indz and $[Au(PrMe_2Indz)]PF_6$, respectively. The sp^3 carbon (**h**) around 48.52 ppm in the H_2Prme_2Indz spectrum appears to be absent in the complex spectrum. This is because it overlapped with the DMSO solvent peak after chelation, which appears at around 40 ppm in the $[Au(PrMe_2Indz)]PF_6$ ^{13}C NMR spectrum.

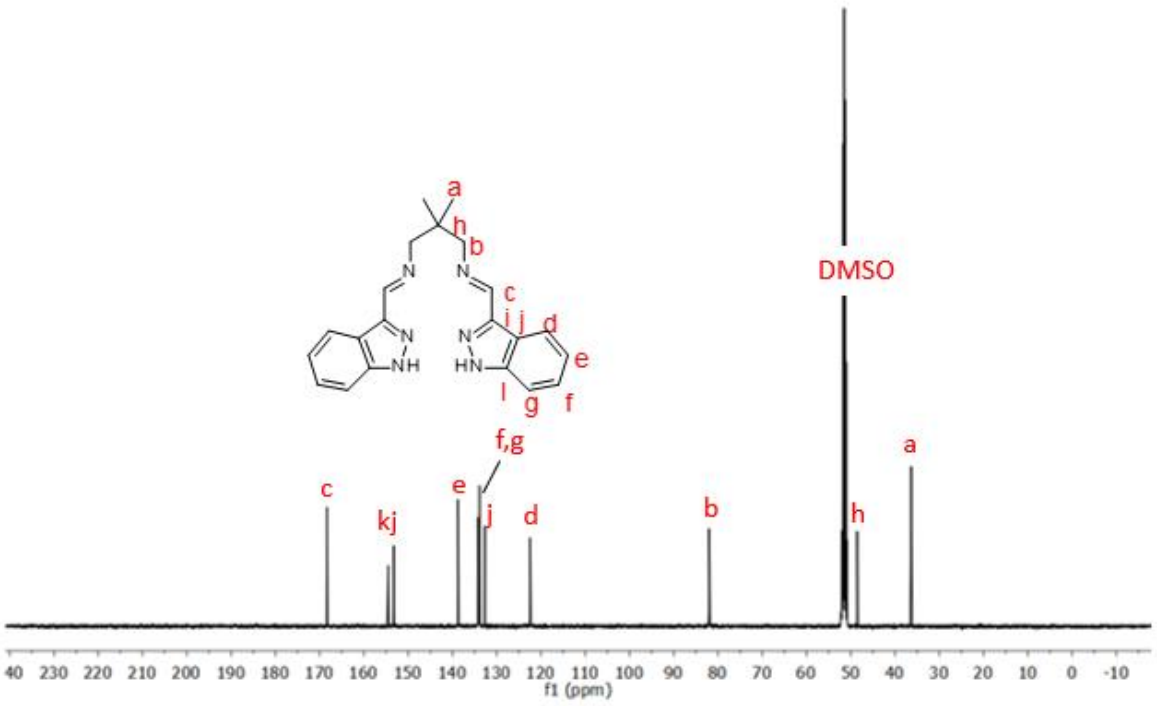

Figure 3.9: Assigned ^{13}C NMR spectrum of H_2prMe_2Indz in DMSO at 300 K.

It is also apparent that Au(III) chelation caused the indazole ring ^{13}C signals in the $[Au(PrMe_2Indz)]PF_6$ ^{13}C spectrum to become more resolved than in the H_2PrMe_2Indz NMR spectrum. The CH_2 carbon (b), in the $[Au(PrMe_2Indz)]PF_6$ spectrum, seems to have experienced the greatest upfield shift (from 81.98 ppm to 62.83 ppm). This is because it is very close to the Au(III) ion in the $[Au(PrMe_2Indz)]PF_6$ structure.

This is also the case with the five-membered ring carbon signal N=C (**i**). These results are consistent with the ^{13}C NMR spectral shifts reported for the related bis(pyrrolide-imine) Au(III) macrocycles.[6] The NMR assignments for all bis(indazole-imine) ligands and Au(III) chelates are reported in Chapter 2; the assignments were made using DFT-calculated shielding tensors to guide the assignment of the experimental spectra..

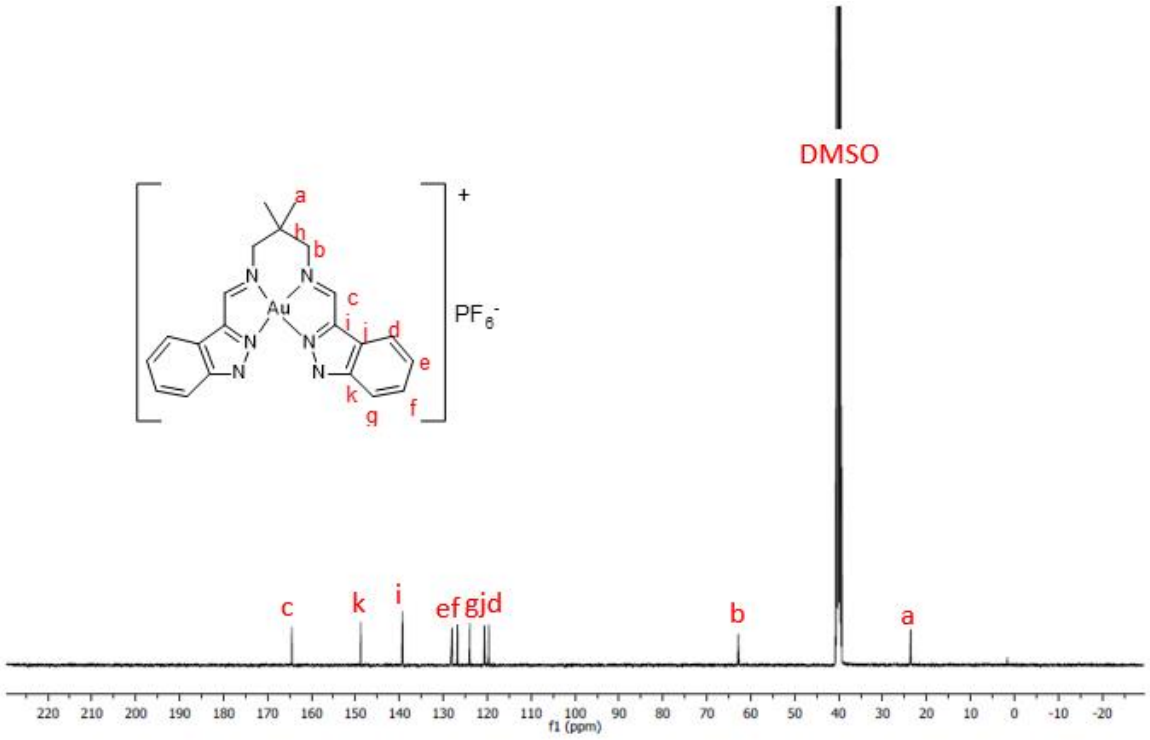

Figure 3.10: Assigned ^{13}C NMR spectrum of [Au(PrMe$_2$Indz)]PF$_6$ in DMSO at 300 K.

3.2.4. Mass spectroscopy of ligands and Au(III) chelates

High-resolution mass spectroscopy was used to determine the mass of both bis(indazole-imine) ligands and the corresponding Au(III) chelates. All the spectra were recorded in the ES+ mode. Figures 3.11 and 3.12 below show the mass spectra of H_2PrOHIndz and [Au(PrOHIndz)]PF_6, respectively. The H_2PrOHIndz peak appears at 347.16 *m/z* in the ligand spectrum; this peak indicates that the ligand was successfully synthesized. Another peak at 219.12 m/z represents the $C_{11}H_{14}N_4O$ fragment of the ligand. This means that the ligand breaks at one of the imine bonds during ionization.

This is the case with all the other bis(indazole-imine) ligands reported in this work. The [Au(PrOHIndz)]PF_6 peak appears at 541.10 *m/z* in the complex MS spectrum. This mass corresponds to the actual mass of the chelate, thus indicating its successful synthesis.

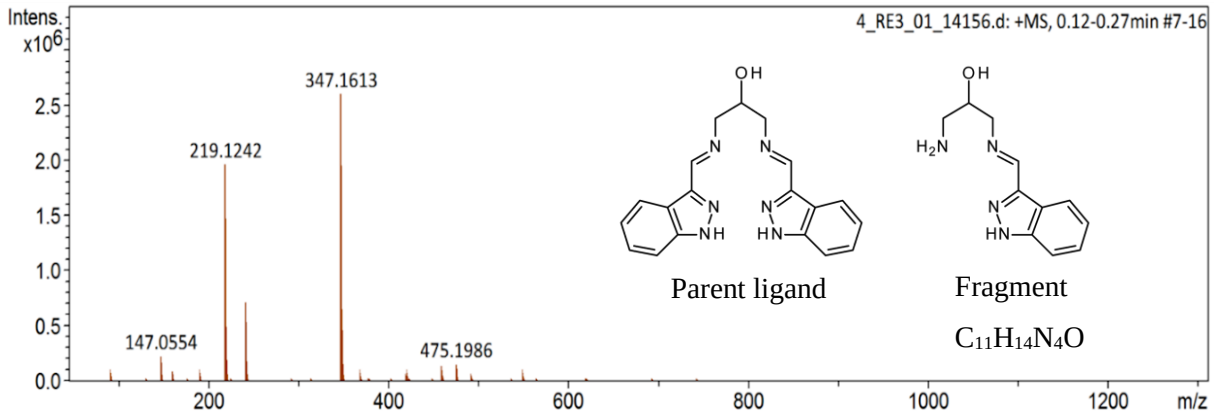

Figure 3.11: Mass spectrum of H_2PrOHIndz showing its mass peak at 347.16 *m/z*. Another peak at 219.12 *m/z* represents the $C_{11}H_{14}N_4O$ fragment of H_2PrOHIndz.

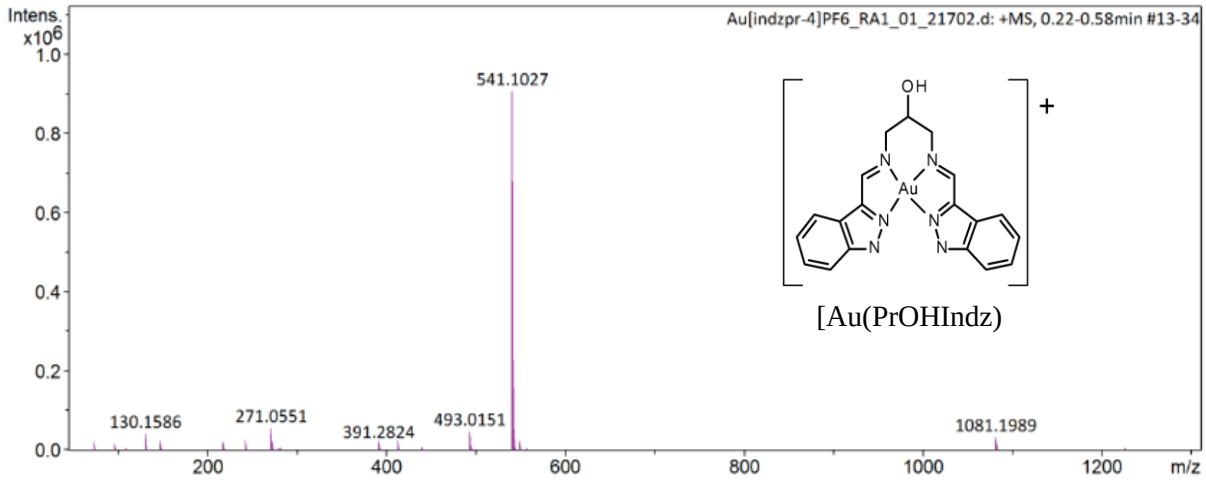

Figure 3.12: Mass spectrum of [Au(PrOHIndz)]PF_6 showing its mass peak at 541.10 *m/z.*

The mass spectrum of the Au(III) chelate lacks distinct and abundant low mass fragments. This is different to what is observed with the ligand above. There is no evidence for demetallation of the Au(III) ion from the chelating ligand in the MS experiment, nor any evidence for any stable fragments derived from the metal chelate. This suggests that the Au(III) chelate is remarkably stable in solution and under ionising conditions within the mass spectrometer.

The peak at m/z = 1081 on the metal chelate spectrum indicates that the cation has π-π dimer that is stable enough to be detected. The mass is exactly 2 × 541.The stable dimer is formed (m/z = 1081). The dimer may lose a proton in the MS because the charge is not 2+ on the molecular entity, as expected for two pi-stacked cations. The dimer's mass is m/z = 1081 instead of m/z = 1082 because this mass is consistent with the loss of a proton which then makes one of the cations neutral and the total charge (of the dimer) is then 1+ and not 2+.

3.3. References

(1) Borisova, N.E., Reshetova, M.D. and Ustynyuk, Y.A., 2007. Metal-free methods in the synthesis of macrocyclic Schiff bases. *Chemical Reviews*, *107*(1), pp.46-79.

(2) van den Ancker, T.R., Cave, G.W. and Raston, C.L., 2006. Benign approaches for the synthesis of bis-imine Schiff bases. *Green Chemistry*, *8*(1), pp.50-53.

(3) Munro, O.Q. and Camp, G.L., 2003. Self-recognition in a flexible bis (pyrrole) Schiff base derivative: formation of a one-dimensional hydrogen-bonded polymer. *Acta Crystallographica Section C: Crystal Structure Communications*, *59*(12), pp.672-675.

(4) Bacchi, A., Carcelli, M., Gabba, L., Ianelli, S., Pelagatti, P., Pelizzi, G. and Rogolino, D., 2003. Syntheses, characterization and X-ray structure of palladium (II) and nickel (II) complexes of tetradentate pyrrole containing ligands. *Inorganica Chimica Acta*, *342*, pp.229-235.

(5) Simonov, Y., Bologa, O., Bourosh, P., Gerbeleu, N., Lipkowski, J. and Gdaniec, M., 2006. Synthesis and structural characterization of gold (III) dioximates with anions $[AuCl_4]^-$ and $[AuCl_2]^-$. *Inorganica Chimica Acta*, *359*(2), pp.721-725.

(6) Akerman, K.J., Fagenson, A.M., Cyril, V., Taylor, M., Muller, M.T., Akerman, M.P. and Munro, O.Q., 2014. Gold (III) macrocycles: nucleotide-specific unconventional catalytic inhibitors of human topoisomerase I. *Journal of the American Chemical Society*, *136*(15), pp.5670-5682.

(7) Lammer, A.D., Cook, M.E. and Sessler, J.L., 2015. Synthesis and anti-cancer activities of a water-soluble gold (III) porphyrin. *Journal of Porphyrins and Phthalocyanines*, *19*(01n03), pp.398-403.

(8) Munro, O.Q., Akerman, K.J. and Akerman, P., University of Kwazulu Natal, 2016. *Gold complexes for use in the treatment of cancer*. U.S. Patent 9,346,832.

(9) Leoni, L., Carletta, A., Fusaro, L., Dubois, J., Tumanov, N.A., Aprile, C., Wouters, J. and Dalla Cort, A., 2019. A Simple and Efficient Mechanochemical Route for the Synthesis of Salophen Ligands and of the Corresponding Zn, Ni, and Pd Complexes. *Molecules*, *24*(12), p.2314.

(10) Barnholtz, S.L., Lydon, J.D., Huang, G., Venkatesh, M., Barnes, C.L., Ketring, A.R. and Jurisson, S.S., 2001. Syntheses and Characterization of Gold (III) Tetradentate Schiff Base Complexes. X-ray Crystal Structures of [Au (sal_2pn)] $Cl \cdot 2.5\ H_2O$ and [Au (sal_2en)] PF_6. *Inorganic Chemistry*, *40*(5), pp.972-976.

Chapter 4

X-ray Crystallography and DFT Simulations

4.1. Introduction

This chapter discusses X-ray crystallography as well DFT simulations of Au(III) chelates. X-ray crystal structures of novel Au(III) bis(indazole-imine) chelates provides structural information such as bond lengths, bond angles as well as the geometry of the structure and makes it possible to study their solid-state interactions and understand the potential of this class of compounds to act as possible DNA intercalators (which are normally planar aromatic cations capable of forming π-stacked oligomers). DFT simulations on the other hand provide the same information as X-ray crystallography and more. Extra information from DFT simulations includes vibrations (IR), NMR and electronic transitions. This chapter, therefore, compares experimental results with the DFT simulations. Four bis(indazole-imine) ligands were successfully synthesized, although it was impossible to obtain their crystal structures due to their inability to crystalize. However, three metal complexes corresponding to three of these ligands were successfully synthesized and studied by X-ray crystallography. According to the Cambridge Structural Database search (CSD), none of the structures related to the bis(indazole-imine) ligands were made or reported before. The complexes reported in this work are therefore novel.

4.2. X-ray crystallography of Au(III) chelates

The crystal data for bis(indazolide-imine) Au(III) chelates are given in Table 4.1 below. The tabulated data show the crystal system, space group, crystallization temperature, and the *Z* value.

Table 4.1: Crystal data for bis(indazolide-imine) Au(III) chelates.

Crystal structure	Crystal system	Space group	*Z*	Temperature (K)
[Au(PrIndz)]Cl·3H_2O	Triclinic	*P*-1	2	173.15
[Au(PrIndz)]$AuCl_4$·CH_3CN	Monoclinic	$P2_1/c$	8	173.15
[Au($PrMe_2$Indz)]PF_6·CH_3CN	Triclinic	*P*-1	2	173.15
[Au(PrOHIndz)]PF_6·2DMSO	Monoclinic	$P2_1$	2	173.15

4.2.1. X-ray crystallography of [Au(PrIndz)]Cl·3H$_2$O and [Au(PrIndz)][AuCl$_4$]·CH$_3$CN

The crystals were grown from a DMF solution of the complex layered with diethyl ether. The bulk sample of crystals comprised [Au(PrIndz)][AuCl$_4$]·CH$_3$CN, which contained an undesired counterion, $[AuCl_4]^-$, that is incompatible with biological molecules and cells were grown in culture. These crystals were bright orange-red needles when viewed in the NMR tube used for crystallization. Under the microscope, close inspection revealed that the crystals were pleochroic, meaning that when viewed with the broad needle face toward the viewer, the crystals were yellow. However, on reorienting the same crystal through an angle of 90° so that the view was parallel to the thin needle face, the crystals were dark red. Several X-ray data sets were collected because the crystals all had intrinsically weak X-ray diffraction; one data set luckily afforded an unpublishable low-resolution structure that confirmed the composition of the crystals and especially the presence of the $[AuCl_4]^-$ ion.

Whilst searching for a better crystal specimen, some clear dark red needles that were non-pleochroic were discovered. These crystals were a minority species in the bulk sample (< 0.5%). A suitable specimen was mounted and had an astonishing scattering power (to better than 0.6 Å resolution). The present X-ray structure report relates to this crystal specimen of the minority species and outstanding quality, which is none other than the trihydrate of the starting chloride salt used in the metathesis reaction with [Bu$_4$N][PF$_6$], specifically [Au(PrIndz)]Cl·3H$_2$O.

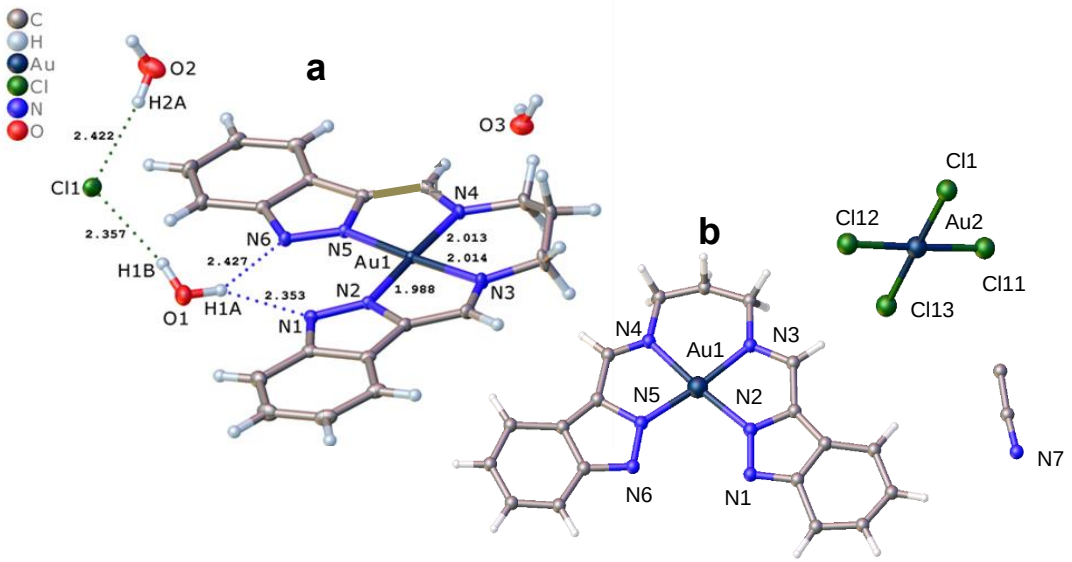

Figure 4.1: Thermal ellipsoid view of the X-ray structure of [Au(PrIndz)]Cl·3H_2O and [Au(PrIndz)][$AuCl_4$]·CH_3CN rendered at the 50% probability level. Hydrogen bonds, selected atom labels, and interaction distances (Å) are shown for [Au(PrIndz)]Cl·3H_2O.

[Au(PrIndz)]Cl·3H_2O crystallised in the triclinic space group *P*-1, *Z* = 2, Figure 4.1a. An important feature of this structure is that it highlights how the ligand interacts with an H-bonding solvent such as water via the indazole nitrogen atoms labeled N1 and N6. The complex is expected to show significant water solubility. [Au(PrIndz)][$AuCl_4$]·CH_3CN, however, crystallized in the monoclinic space group $P2_1/c$, *Z* = 8, Figure 4.1b. A search of the CSD (Cambridge Structure Database) search has proved that the bis(indazolide-imine) gold(III) chelates reported here have not been previously structurally characterized.

The compounds represented in this work are therefore completely novel. Metal chelation occurs with concomitant deprotonation of the two indazole N-H protons, as the ligand occupies four available coordination sites of the Au(III) cation, forming a monocationic square planar chelate with a Cl^- counterion. Table 4.2 below gives more information regarding the coordination sphere of the cationic complex, $[Au(PrIndz)]^+$.

Table 4.2: Selected bond lengths and bond angles describing the coordination sphere of [Au(PrIndz)]$^+$ for [Au(PrIndz)]Cl·3H_2O.

Bond	Length (Å)	Bond	Angle (°)
Au1-N2	1.9884 (13)	N2-Au-N5	102.69(5)
Au1-N3	2.0141(13)	N2-Au-N3	79.93(5)
Au1-N4	2.0129(13)	N3-Au-N4	97.25(5)
Au1-N5	1.9883(12)	N4-Au-N5	80.12(5)

As expected, the Au-$N_{indazole}$ bond lengths are shorter than the Au-$N_{imine\ bond}$ lengths. This is due to the indazole groups being anionic σ-donors with C-N-C bond angles that are more acute than the C=N-C angle of the imine group as already mentioned above. This compound is therefore very similar to macrocyclic Au(III) chelates and other related Au(III) chelates in this regard.[1] Figure 4.2 below shows that coordination of the ligand with the square planar Au(III) ion yields a predominantly planar complex with the alkyl group protruding out of the molecular mean plane. The distances (in Å) between the mean planes passing through all nominally coplanar atoms (23 in total) within each cation partner constituting the symmetry-unique dimer are highlighted. The distance is most easily measured as the Au···plane separation, which averages 3.15(1) Å and is consistent with a tight π-stacked interaction. The interplanar separation between adjacent π-stacked dimers in the extended 1D stacked array is also shown (3.348 Å).

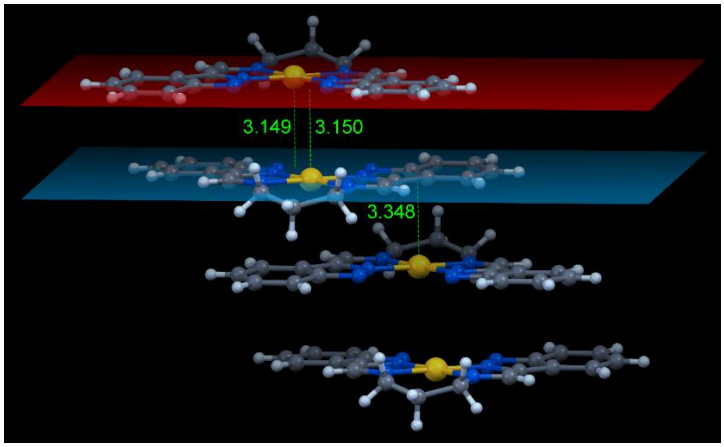

Figure 4.2: View of the centrosymmetric π–π dimers formed by the cations in the triclinic X-ray structure of [Au(PrIndz)]Cl·3H_2O. The model is rendered in ball and stick format; solvate water molecules and chloride ions have been omitted for clarity.

4.2.2. X-ray crystallography of [Au(PrMe$_2$Indz)][PF$_6$]·CH$_3$CN

[Au(PrMe$_2$Indz)][PF$_6$]·CH$_3$CN crystallized in the triclinic space group *P*-1, *Z* = 2, Figure 4.3. The chelate contains two indazole rings linked through a dimethyl propyl bridge.

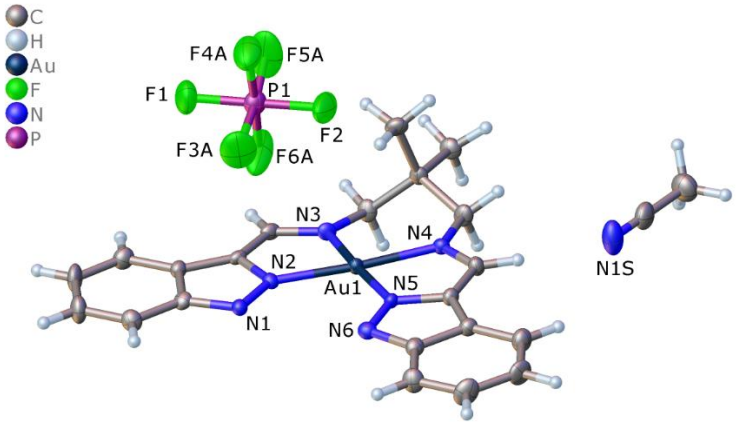

Figure 4.3: Thermal ellipsoid view (50% probability surfaces) of the X-ray structure of [Au(PrMe$_2$Indz)][PF$_6$]·CH$_3$CN showing the cation and closest positions for the anion and solvent molecule. Selected atoms have been labeled. Only the major component (ca. 60%) of the disordered hexafluorophosphate(V) ion is shown and all H atoms are drawn as spheres of an arbitrary radius.

Metal chelation has yielded a planar complex with the dimethylpropyl linkage approximately perpendicular to the plane. As shown in Figure 4.4 below, the cations of [Au(PrMe$_2$Indz)]PF$_6$·CH$_3$CN form π-stacks in the crystal structure in which there exist symmetry-unique inter-planar spacings. The inter-planar spacings measure 3.16 Å and 3.32 Å between the inversion pair (red and blue planes) and neighboring dimers (blue and green planes), respectively, defined by 23 atoms.

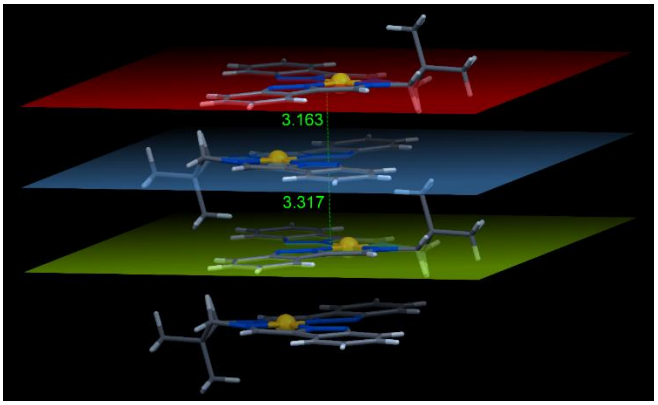

Figure 4.4**:** View of the cation stack in the crystal structure of [Au(PrMe$_2$Indz)][PF$_6$]·CH$_3$CN with the symmetry-unique inter-planar spacings (Å) illustrated.

Table 4.3 below shows the selected bond lengths and bond angles that describe the coordination sphere of [Au(PrMe$_2$Indz)][PF$_6$]·CH$_3$CN. This data favorably compares to that of [Au(PrIndz)]$^+$ wherein the Au-N$_{indazole}$ bond lengths are shorter than the Au-N$_{imine}$ bond lengths.

Table 4.3: Selected bond lengths and bond angles of [Au(PrMe$_2$Indz)][PF$_6$]·CH$_3$CN representing its coordination sphere.

Bond	Length (Å)	Bond	Angle (°)
Au1-N2	1.995(3)	N2-Au-N5	103.48(13)
Au1-N3	2.015(3)	N2-Au-N3	80.45(14)
Au1-N4	2.008(3)	N3-Au-N4	95.92(13)
Au1-N5	1.986(3)	N4-Au-N5	80.20(13)

The neighboring molecules form head-to-tail π-stacked columns in which the molecules in the columns are aligned such that the indazole ring and the alkyl linkage of one compound overlap with the indazole ring and the alkyl chain of the neighboring molecule, Figure 4.5. The π-stacked dimers are also stabilized by short intermolecular contacts (Å) with a distance less than the sum of the van der Waals radii of the interacting atoms minus 0.10 Å ($d_{vdw} < \{r_1 + r_2\} - 0.1$).

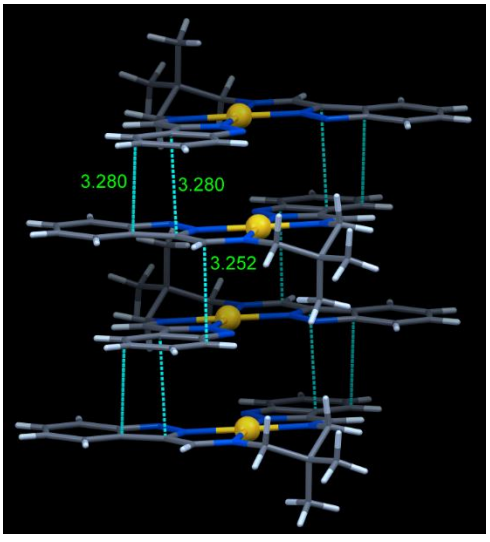

Figure 4.5: View of the short intermolecular contacts (Å) with a distance less than the sum of the van der Waals radii of the interacting atoms minus 0.10 Å ($d_{vdw} < \{r_1 + r_2\} - 0.1$).

4.2.3. X-ray crystallography of [Au(PrOHIndz)]PF_6·DMSO

[Au(PrOHIndz)]PF_6·DMSO crystallized in the monoclinic space group $P2_1$, with two molecules in a unit cell, $Z = 2$ Figure 4.6. The molecule shows that the indazole rings are coplanar with the diimine linkage containing the hydroxy substituent of the 3-carbon bridge perpendicular to the plane. PF_6^- is present as the counterion and DMSO is included as the solvent in the lattice structure.

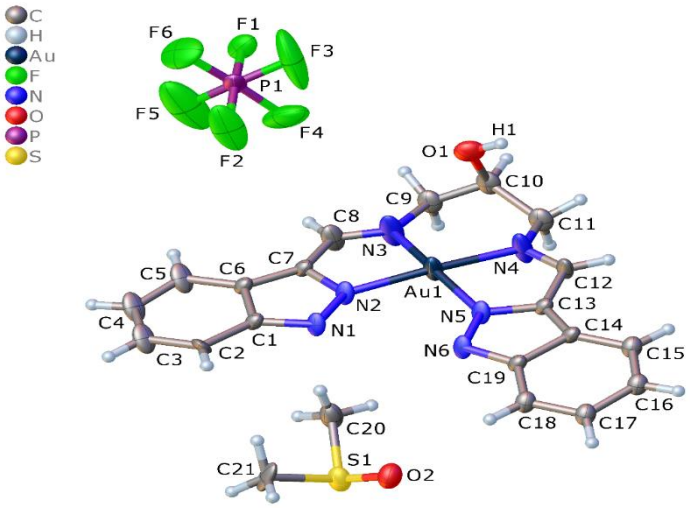

Figure 4.6: Labelled view of the X-ray structure of [Au(PrOHIndz)]PF_6·2DMSO. Thermal ellipsoids are rendered at the 30% probability level. Only the ordered DMSO molecule is shown and was included in the final model.

The average Au-N_{imine} and Au-$N_{indazole}$ bond lengths for [Au(PrOHIndz)]PF_6 are 2.03(10) Å and 1.990(9) Å, respectively. These bond lengths are very similar to those of [Au($PrMe_2$Indz)]PF_6 and [Au(PrIndz)]Cl reported in this work and are also consistent with those reported in the literature.[1] Au-N_{imine} bond lengths are longer than the Au-$N_{indazole}$ bond lengths as expected and summarized in Table 4.4. The coordination geometry about the Au(III) ion is entirely square planar as indicated by N-Au-N angles that are close to 90° and the Au-N bond angles that are almost equal. The metal ion is also located in the plane of the four N-donor atoms of the chelating ligand.

Table 4.4: Selected bond lengths and bond angles of [Au(PrOHIndz)]PF_6 describing its coordination sphere.

Bond	Length (Å)	Bond Angle	Angle (°)
Au1-N2	1.98(10)	N2-Au-N5	103.6(4)
Au1-N3	2.04(15)	N2-Au-N3	79.7(5)
Au1-N4	2.02(14)	N3-Au-N4	96.1(6)
Au1-N5	2.00(10)	N4-Au-N5	79.5(5)

Figure 4.7 below illustrates the π-stacking between the Au(III) cations within the crystal lattice of [Au(PrOHIndz)]PF_6·2DMSO. Adjacent molecules form distinct head-to-tail π-stacked columns. Short contacts less than the sum of the van der Waals radii of the interacting atoms are given in blue (dashed) lines. The Au1···C18 contact (thick line) measures 3.481 Å. The OH substituent of [Au(PrOHIndz)]PF_6·2DMSO forms hydrogen bonds with the O atom of the DMSO (solvent).

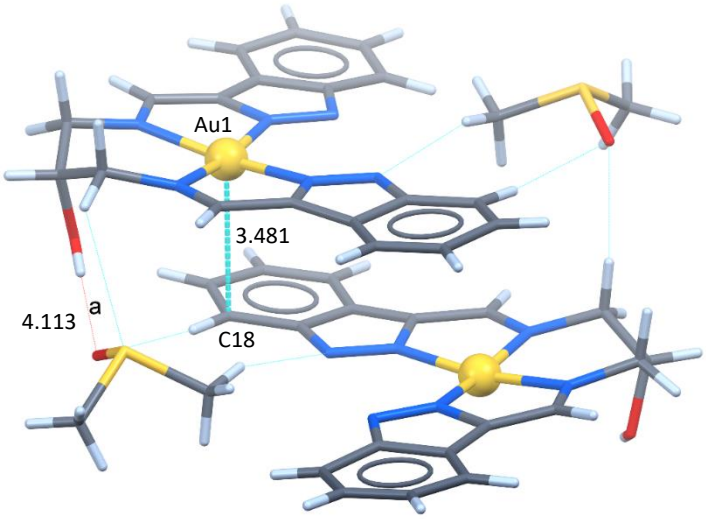

Figure 4.7: Illustration of the π-stacking between cations in the crystal lattice of [Au(PrOHIndz)]PF_6·2DMSO.

4.3. Crystal structure analysis of [Bu_4N][$AuCl_4$]

Crystallization of [Bu_4N][$AuCl_4$] yielded crystals suitable for X-ray crystallography with a respectable final *R*-factor of 2.66 % (shown in Figure 4.5 below). The crystals were simply obtained by dissolving the compound in DCM and leaving the solution to evaporate overnight, which afforded an X-ray quality yellow crystalline solid. Given the utility of the compound as a key Au(III) synthon or metallating reagent in this project, we elucidated the structure of the compound.

The crystal structure details of this compound have not been reported before and it is for the first time they are reported in this work. The compound crystallized in the monoclinic space group $P2_1/n$ with the following unit cell parameters: a = 14.77 (7) Å, b = 8.821 (5) Å, c = 18.14(12) Å, α = 90°, β = 107.1(2), and γ = 90°. The C-C and C-N bond length averages are 1.512(4) Å and 1.519(4) Å, respectively. These bond lengths are very similar to those reported in the literature for organic compounds.[2] The average Au-Cl bond length is 2.275 (10) Å with the reported average being 2.30 (8) Å. The average C-N-C bond angle is 108.59(2)°. Unconventional C-H···Cl hydrogen bonds between the cation and the anion can be noted in this structure, these are indicated by the picture on the left in Figure 4.8.

The average bond length of these hydrogen bonds is 3.301(1) Å. Similar C-H···Cl^- hydrogen bonds reported in the literature for pyrimidine compounds (PYM-Cl^- systems) have an average bond length of 2.400(1) Å.[3] The difference in bond lengths may signify their different strengths.

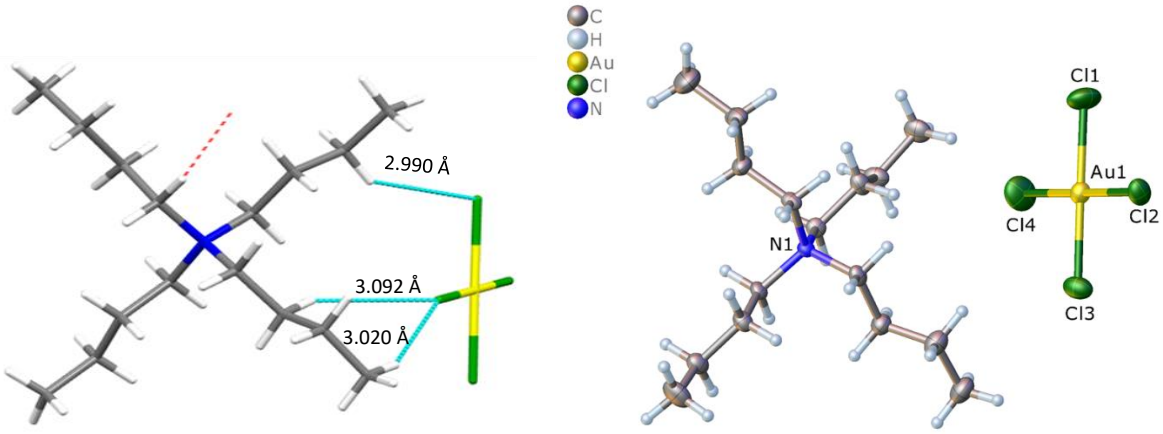

Figure 4.8: X-ray crystal structure of $[BuN_4][AuCl_4]$ analyzed at 173.15 K. The illustration on the left side shows unconventional C-H···Cl hydrogen bonds between the cation and the PF_6^- anion in the structure $[AuCl_4]^-$.

4.4. Conclusion

It was impossible to obtain X-ray structures of the bis(indazole-imine) ligands in this work, despite repeated crystallization attempts due to the isolation of powder and very fine needle-like crystals that were generally unsuitable for single crystal X-ray studies. However, the structures of three bis(indazole-imine) Au(III) chelates were obtained and studied by X-ray diffraction. Two X-ray structures distinguished by different counterions (Cl^- and $[AuCl_4]^-$) were obtained for the propyl-bridged Au(III) chelate: $[Au(PrIndz)]Cl{\cdot}3H_2O$ and $[Au(PrIndz)][AuCl_4]{\cdot}CH_3CN$. Although $[Au(PrIndz)]Cl{\cdot}3H_2O$ is the most desired compound due to the Cl^- counterion which is compatible with cells, and its high solubility, the crystal sample only contained a small amount of this salt, while the majority of the sample contained $[Au(PrIndz)][AuCl_4]{\cdot}CH_3CN$ which, possesses an undesired counterion ($AuCl_4^-$) that is poisonous to cells. Further refining and purification of the crystal sample yielded 100% $[Au(PrIndz)][AuCl_4]{\cdot}CH_3CN$ which made it even more difficult to obtain the Cl^- counterion. Part of the future work is therefore to explore more options that will give pure $[Au(PrIndz)]Cl{\cdot}3H_2O$. The most acceptable counterions are Cl^- and/or PF_6^-. The other two Au(III) chelates, $[Au(PrMe_2Indz)]PF_6{\cdot}CH_3CN$ and $[Au(PrOHIndz)]PF_6{\cdot}DMSO$ were somewhat easier to prepare in the desired salt form and contained the PF_6^- counterions.

For all Au(III) chelates, metal chelation occurred with concomitant deprotonation of two pyrrole NH protons producing monocationic square planar chelates. The mean planes indicate that the Au(III) chelates are planar with the alkyl bridging unit being approximately perpendicular to the plane. Similar to previously studied macrocyclic Au(III) chelates with pyrrolide-imine groups, the Au-N_{imine} bond lengths are longer than the Au-$N_{indazole}$ bond lengths due to the indazole groups being anionic σ-donors with C-N-C bond angles that are more acute than the C=N-C bond angle of the imine group. Each chelate undergoes significant π-stacking interactions with the adjacent molecule in the crystal, clearly indicating their potential as possible DNA intercalators.

4.5. Density Functional Theory (DFT) Simulations

DFT is a computational method, commonly used to calculate the ground-state electronic structures of molecules, atoms, and solids.[4] The main objective of DFT methods is to create functionals that relate the energy with electron density.[5] Unlike the Schrodinger equation which focuses on the wave function, DFT is mostly concerned with the electron density of systems.[4]

The introduction of orbitals into computational chemistry by Kohn and Sham was a pioneering step in the foundation of DFT methods.[5] The downfall of models that excludes the concept of orbitals is the underrepresentation of kinetic energy. The objective behind Kohn and Sham's idea, therefore, is to break the kinetic energy function of the system into a small correction term and a part that can be calculated exactly. With the introduction of orbitals, the complexity then increases from 3 variables to 3N variables, requiring the electron correlation to stand as a separate term.[5] The sum of the electron kinetic energy, the nucleus-attraction potential energy and the electron-electron repulsion potential energies gives the ground state electronic energy given by the equation:

$$E = T[\rho] + V_{Ne}[\rho] + V_{ee}[\rho] \qquad 4.1$$

Kohn-Sham DFT describes consistent equations that must be solved for a group of orbitals such that their density ρ(r) resembles that of a real system. These equations require that a small energy contribution be given as ρ(r). The kinetic energy is calculated with the assumption of non-interacting electrons where the Slanter determinant (S) is included and possesses a molecular orbital φ_i, the exact kinetic energy is therefore given by the equation:

$$T_S = \sum_{i-1}^{Nele} \langle \phi_i | -\tfrac{1}{2} \tilde{\nabla}^2 | \phi \rangle \qquad 4.2$$

In reality, however, there is an interaction between the electrons, the difference between the calculated kinetic energy and the exact kinetic energy when assuming non-interacting orbitals is, therefore, small. The rest of the kinetic energy is channeled into an exchange-correlation (XC) term. The generic DFT expression for energy is given by the equation:

$$E_{DFT}\,[\rho] = T_S[\rho] + E_{Ne}[\rho] + J[\rho] + E_{XC}[\rho_0] \qquad 4.3$$

The (XC) can be approximated in the practical calculation and the quality of the results is dependent on the approximation used.[4] Local density approximation (LDA) was the most straightforward XC approximation used as the standard in the calculation of solid electronic structures in the 1970s and 1980s. However, LDA has molecules overbound by approximately 1 eV/bond which led to the generalized gradient approximations (GGA) being realized in the late 1980s.[4] The GGA afforded good accuracy at a low computational cost in chemical calculations. Becke, however, introduced hybrids that replaced GGA with Hartree-Fock (HF) in the 1990s, leading to the most popular B3LYP approximation used in chemistry today.

DFT is integrated into many electronic structure codes such as MOLPRO, GAUSSIAN, GAMESS, etc. By far, DFT is the only method being used for the calculation of enormous electronic structures such as nucleic acids, enzymes, and proteins.[4] For macromolecules, the bulk protein or nucleic acid structure is often modeled using efficient molecular mechanics methods, while the active site of interest is modeled by DFT methods as these include electronic effects and give realistic accuracy for the chemically active region in the protein. These methods are hybrid MM-DFT methods and are useful for performing simulations on very large structures.

4.5.1. Computational objectives

In this section, computational simulations were performed on the two successfully synthesized bis(indazolide-imine) Au(III) chelates: [Au($PrMe_2$Indz)]PF_6 and [Au(PrOHIndz)]PF_6. This section, therefore, intends to compare the outcome of computational simulations with that of the X-ray structures.

4.5.2. Computational studies of Au(III) chelates

4.5.2.1. DFT-calculated geometries

The lowest energy geometries of bis(indazolide-imine) Au(III) chelates were determined through geometry optimization calculations using the HSEHIPBE/SDD level of theory. The DFT-calculated structure was then compared with the experimental structure to evaluate the correctness of the simulations. The accuracy of the simulated structure relative to the experimental structure was determined using least-square fitting and the similarity of the two structures was measured by the RMSD values. Figure 4.9 below shows the least-squares fit for [Au($PrMe_2$Indz)]PF_6 as representative of bis(indazolide-imine) Au(III) chelates. The least-squares fit for [Au(PrOHIndz)]PF_6 is indicated in Appendix E.

As anticipated, the DFT-calculated structure is planar as the Au(III) ion prefers a planar geometry due to the presence of its empty dx^2-y^2 orbital. The calculated structure appears to be in good agreement with the experimental structure. Although the experimental structure is influenced by intermolecular interactions in the crystal lattice, it is imperative to note that the DFT-calculated structure is in the gas phase and is not influenced by such interactions. The RMSD obtained was 0.1195 Å which is relatively low indicating that the DFT-calculated structure is accurate which means that the basis-set used was reliable for the simulation. RMSD's below 2 Å are good and indicate a good prediction.[6]

The geometry optimization results were compared to those of bis(pyrrolide-imine) Au(III) chelates which are reported in the literature and are very similar to the reported compounds in terms of structure. These included open chain, pseudomacrocyclic and macrocyclic bis(imine-pyrrolide) Au(III) chelates. The DFT-calculations of these chelates were conducted at a PBEPBE/LANL2D2 level of theory. They all varied from planarity to different extents, however, their RMSD were still low which implied a good comparison between the calculated and the experimental structures.

The RMSD varied from 0.0771 Å to 0.447 Å. These results, however, excluded those of a pseudomacrocyclic Au(III) chelate that afforded an RMSD of 0.674 Å which is relatively high due to the flexible nature of the ethyl appendages and the extent of the twisting of the pyrrole and imine rings. The method used in this work (HSEHIPBE/SDD) is therefore comparable with this method.

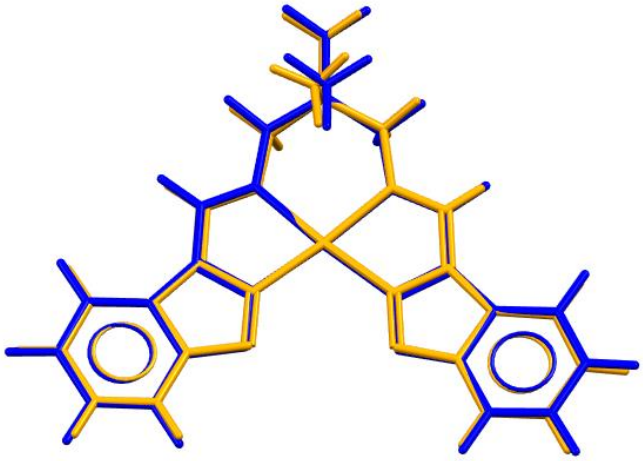

[Au(PrMe$_2$Indz)]PF$_6$: RMSD = 0.1195 Å

Figure 4.9: The least-squares fit for the DFT-calculated structure (blue) and the X-ray structure (orange) of [Au(PrMe$_2$Indz)]PF$_6$. The RMSD value is also indicated with the structure.

Table 4.5 below compares the bond distances and bond angles of the DFT-calculated and the X-ray structures of [Au(PrMe$_2$Indz)]PF$_6$. Both results show a good agreement with each other. The average percentage difference in both bond distances and bond angles is less than 2%, reflecting the accuracy of the model used for the simulation and the lack of any large lattice-induced distortions of the experimental structure. The small errors could be due to the X-ray structure not being 100% planar (as it appears in Figure 4.9), with both its benzene rings being slightly tilted. In general, the geometry optimization results for the DFT-calculated structure and X-ray structure compare very well with each other.

Table 4.5: Comparison between bond lengths and both angles of the DFT-calculated and X-ray structure of [Au(PrMe$_2$Indz)]PF$_6$.

Bond	Exp	Calc	%Diff*
		Bond Distances (Å)	
Au-N$_{indazole}$	1.99	2.02	-1.5
Au-N$_{imine}$	2.01	2.03	-1.0
		Bond Angles (°)	
N$_{indazole}$ -Au-N$_{indazole}$	103	104	-0.9
N$_{imine}$ -Au-N$_{imine}$	95.9	95.7	-0.19

*%Diff = ((exp-calc)/exp) × 100

The selected bond lengths and bond angles of [Au(PrMe$_2$Indz)]PF$_6$ were compared with those of a similar macrocyclic bis(pyrrolide-imine) Au(III) chelate, [Au(L1)]PF$_6$ (shown in Figure 4.10 below).[7] [Au(L1)]PF$_6$ has a similar scaffold to [Au(PrMe$_2$Indz)]PF$_6$ in that its structure possesses two pyrrole rings liked by a diimine bridge.

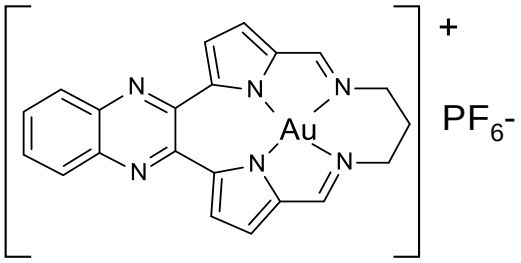

Figure 4.10: [Au(L1)]PF$_6$ ([12,13-dihydro-14H-6,9:17,20-diepimino[1,6]diazacyclo-heptadecino[12,13-β] quinoxalinato]gold(III) hexafluorophosphate(V).[7]

Therefore, the Au-N$_{indazole}$ bond length is compared to Au-N$_{pyrrole}$ bond length while the N$_{pyrrole}$ -Au-N$_{pyrrole}$ bond angle is compared to N$_{indazole}$ -Au-N$_{indazole}$ bond angle as they are very similar. The data are shown in Table 4.6 below. Comparison of the results shows that the bond lengths of the two compounds compare very well with each other. Bond angles, however, have slight differences which could be due to the rings of these compounds being different in size.

Table 4.6: Comparison of the DFT-calculated geometry optimization data of [Au(PrMe$_2$Indz)]PF$_6$ with similar Au(III) chelate [Au(L1)] PF$_6$.[7]

Bond	[Au(PrMe$_2$Indz)]PF$_6$	[Au(L1)] PF_6	%Diff*
	Bond length (Å)		
Au-N$_{pyrr/ind}$	2.02	2.00	-0.99
Au-N$_{imine}$	2.03	2.04	-0.49
	Bond angle (°)		
N$_{pyrr/ind}$ -Au-N$_{pyrr/ind}$	104	99.0	4.81
N$_{imine}$ -Au-N$_{imine}$	95.7	96.8	-1.15

*%Diff = ((bond length/angle Cpd. 1 - bond length/angle Cpd. 2)/(bond length/angle Cpd. 1) x 100

4.5.2.2. DFT-calculated IR spectra

To verify that the geometry optimization outcome was a true minimum on the global potential energy surface, vibrational frequencies were computed. The calculated IR spectral frequencies were compared with the calculated IR spectral frequencies. Figure 4.11 below shows the superimposed calculated and experimental IR spectra for [Au(PrMe$_2$Indz)]PF$_6$ as a representative of the Au(III) chelates reported herein.. See Appendix E for the DFT-calculated IR spectrum of [Au(PrOHIndz)]PF$_6$.

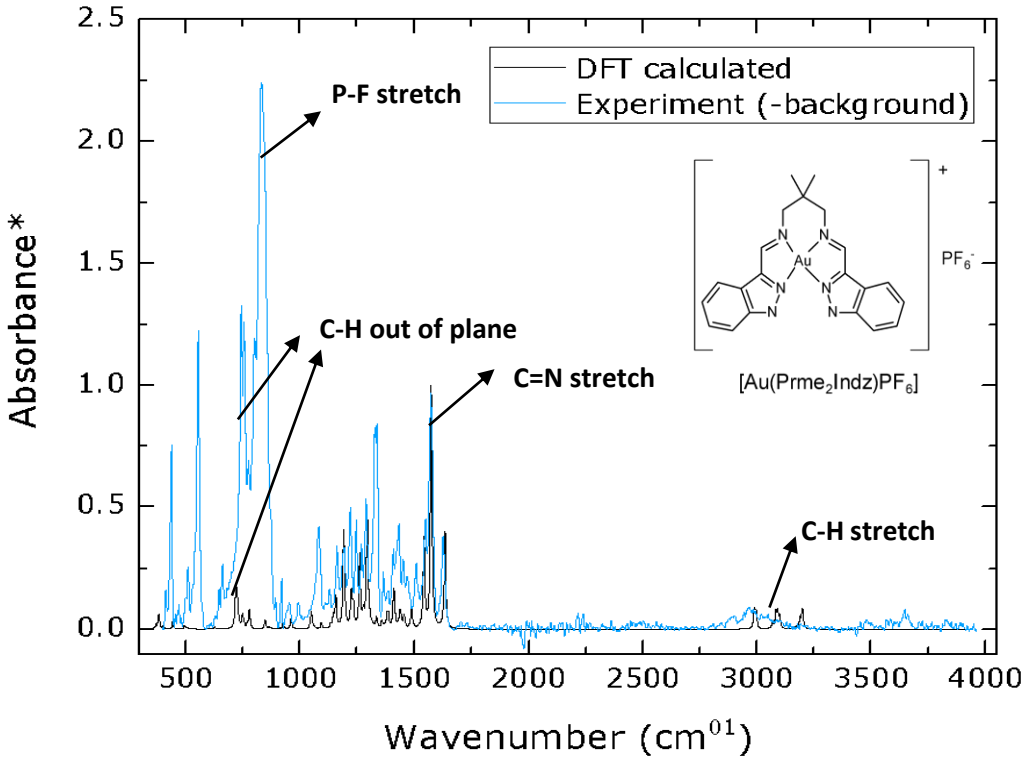

Figure 4.11: Superimposition of DFT-calculated and experimental IR spectra. The calculated IR spectrum has been scaled to match the experimental spectrum. The scale factor of 1 was used.

Figure 4.11 above shows the superimposed spectra of the DFT-calculated and the crystalline material used for the X-ray structure determination. Overall, the figure shows a good agreement between the two spectra based on vibrational frequencies. A good correlation is also observed on the relative intensities, for example, C-H out of plane, C=N and C-H stretch intensity peaks show a good correlation between DFT and the experimental results. However, the frequency of the calculated spectrum has been slightly overestimated for almost all of the peaks relative to the spectrum of the experimental structure.

Although the absorption bands due to the PF_6^- counterion dominates the experimental spectrum, the anion was not included in the calculated spectrum given that the cation is of interest as a metallodrug candidate and the anion is exchangeable and therefore lost both in vitro and in vivo. The differences in frequencies of the peaks between the DFT-calculated and the X-ray structure are shown clearly in Table 4.7.

Table 4.7: Comparison of IR data between the DFT-calculated and X-ray structure of [Au(PrMe$_2$Indz)]PF$_6$.

IR stretch	Exp (cm^{-1})	Calc (cm^{-1})	% Diff*
C-H (in plane)	2987	3175	-6.29
C-H (out of plane)	757	794	-4.89
C=C	1621	1708	-5.37
C=N	1571	1647	-4.84

*%Diff = ((exp-calc)/exp) × 100

Table 4.7 compares the frequency of the C-H (in-plane and out of plane), C=C stretch, and C=N stretching vibrations of the DFT-calculated and the experimental spectra. Although the computational frequencies were slightly overestimated, there is still a good agreement between both results with the average percentage difference of all vibrations being only 5%, although the percentage difference of the C-H (in-plane) mode is slightly higher by 1%. The calculations are accurate, and this is further confirmed by the correlation plot in Figure 4.12 below. The plot gives a linear trend with the correlation coefficient close to 1, which implies that any discrepancies detected are due to systematic errors and can be well accounted for.

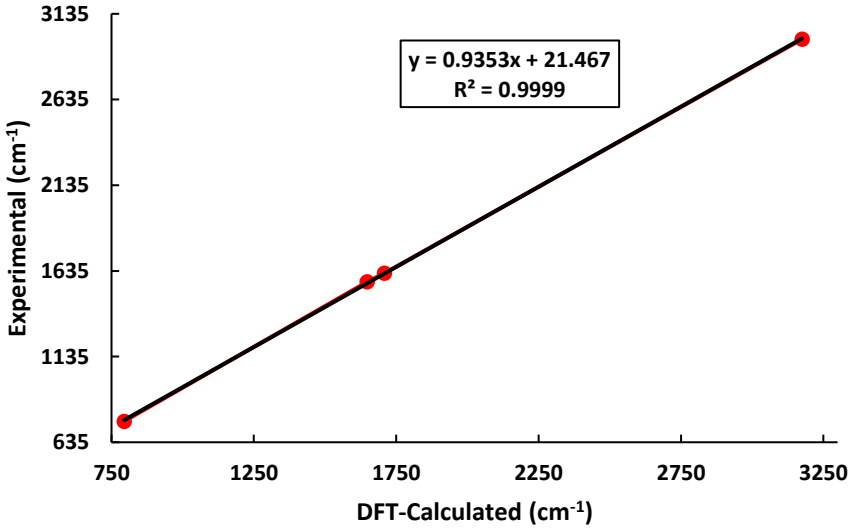

Figure 4.12: A plot showing the correlation between the experimental and DFT-calculated IR frequencies for [Au(PrMe$_2$Indz)]PF$_6$.

The DFT-calculated data for reported chelates were also compared with that of reported macrocyclic bis(pyrrolide-imine) Au(III) chelate, [Au(L1)]PF_6.[7] Only the C=N stretch and the C-H stretch were compared and the data is shown in Table 4.8 below.

Table 4.8: Comparison of the DFT-calculated IR vibrational frequencies (cm^{-1}) for [Au($PrMe_2$Indz)]PF_6 and [Au(L1)]PF_6.

Compound	C=N	C-H
[Au($PrMe_2$Indz)]PF_6	1647	3175
[Au(L1)] PF_6	1610	3008
%Diff*	2.25	5.26

*%Diff = ((bond length/angle Cpd. 1 - bond length/angle Cpd. 2)/(bond length/angle Cpd. 1) x 100

The comparison of the DFT-calculated vibrational frequencies of the C=N and C-H stretches between [Au($PrMe_2$Indz)]PF_6 and [Au(L1)] PF_6 appears to be favorable. The percentage differences between the stretches of the two compounds are relatively small and inevitable considering that the electronic environments of the bonds in the two compounds are different from each other. Small percentage differences indicate that the DFT calculation methods used are comparable.

4.5.2.3. DFT calculated electronic spectra

The TD-DFT method was used to calculate the electronic transitions of bis(indazolide-imine) gold(III) chelates solving for 60 excited states. The HSEHIPBE/SDD level of theory was used. A DMSO solvent continuum was included in the simulations to account for solvent effects found in the experimental UV-vis spectra. The calculated electronic spectrum is compared with the experimental spectrum in Figure 4.13 below, using [Au($PrMe_2$Indz)]PF_6 as a representative of bis(indazolide-imine) gold(III) chelates. See Appendix E for the DFT-calculated UV-vis spectra of [Au(PrOHIndz)]PF_6. The DFT-calculated spectrum has been scaled to match the experimental spectrum to a scale factor of 1.

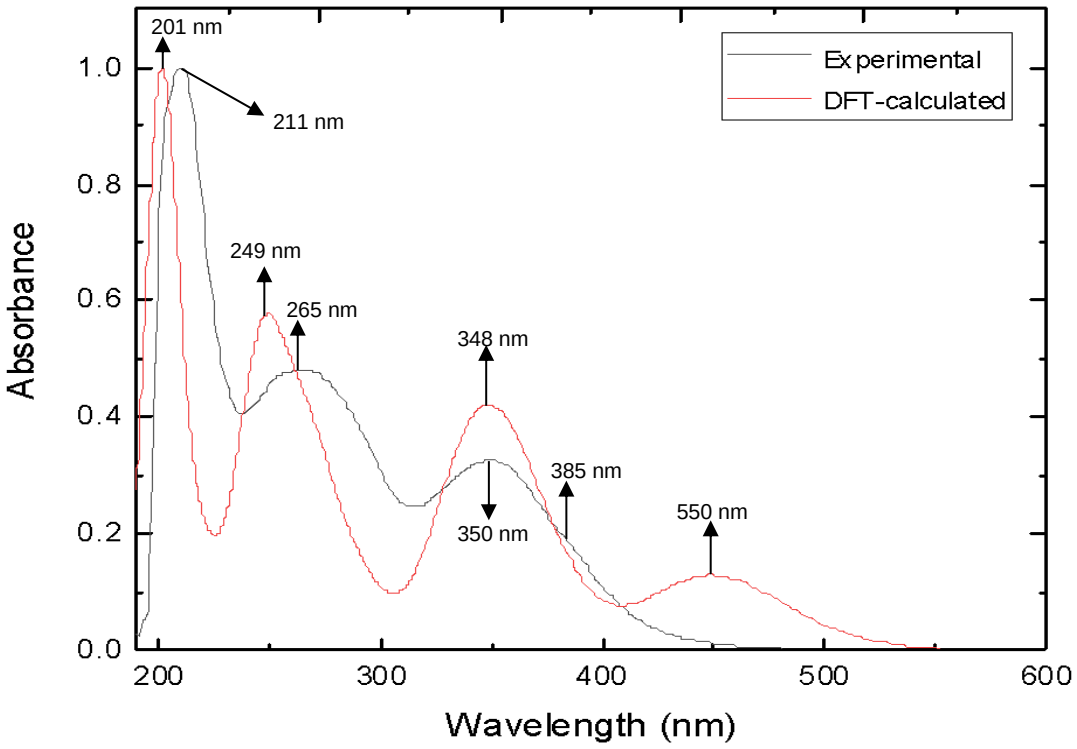

Figure 4.13: Superimposition of DFT-calculated (red) and experimental (black) UV-vis spectra for [Au($PrMe_2$Indz)]PF_6 in DMSO. The spectra were normalized to an absorbance range of 0-1 before plotting.

Figure 4.13 above demonstrates the close agreement between the calculated and the experimental UV-vis spectra. Generally, the calculated spectrum is compared favorably with the experimental spectrum. The results, however, indicate that the calculated spectrum has been slightly overestimated compared to the experimental spectrum.

The calculated spectrum displays a hypsochromic shift relative to the experimental spectrum.

Figure 4.14 below shows molecular orbitals of [Au($PrMe_2$Indz)]PF_6 that are involved in most of its transitions. See Appendix E for the molecular orbitals of [Au(PrOHIndz)]PF_6.

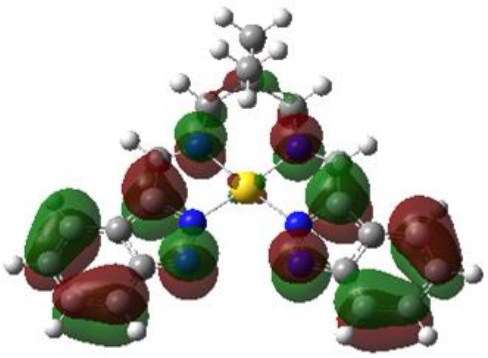

HOMO: Orbital 103

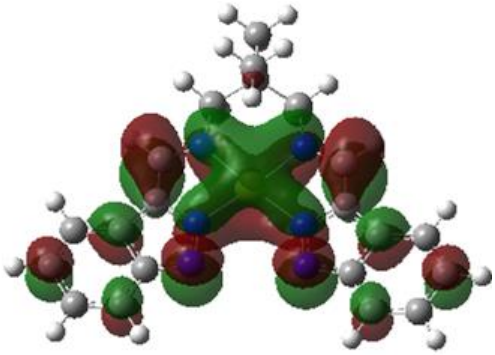

LUMO: Orbital 104

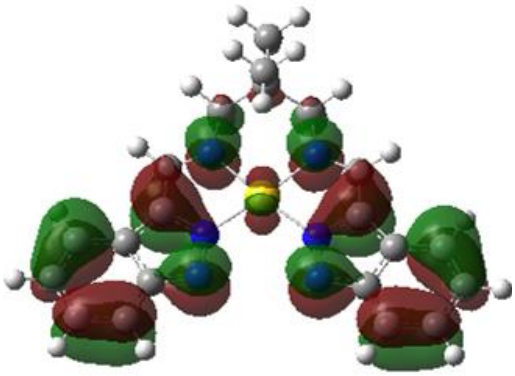

HOMO -1: Orbital 102

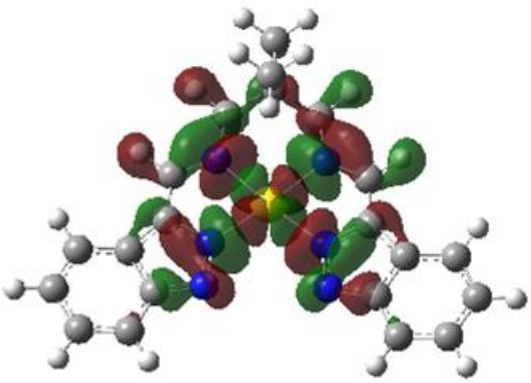

LUMO +1: Orbital 105

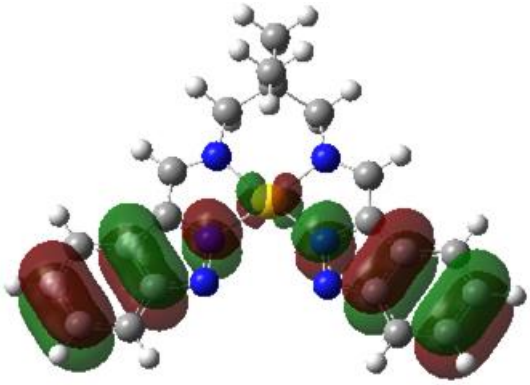

HOMO -2: Orbital 101

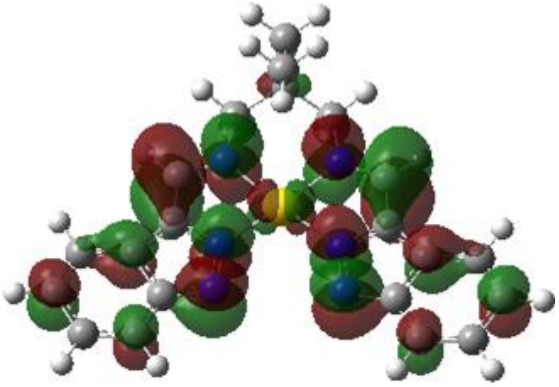

LUMO +2: Orbital 106

Figure 4.14: Image displaying molecular orbitals involved in most of the electronic transitions of [Au($PrMe_2Indz$)]PF_6. Only the LUMO+1 orbital has σ-symmetry, all the other orbitals are mostly π-symmetry.

The HOMO orbital is mostly dominated by π-symmetry with a contribution from the orbital mainly positioned around the indazole rings, however, metal character is also visible with d_{xz} orbitals. The LUMO orbital shows a greater metal character with what is possibly the vacant $6p_z$ atomic orbital of the metal mixing with the π-orbitals of the indazole ring and the C=N bonds. The HOMO-1 orbital is very similar to the HOMO orbital with the d_{yz} atomic orbital of the metal ion mixed with a π-symmetry molecular orbital on the ligand.

The LUMO+1 orbital is mainly σ-symmetry with the orbitals located around the indazole five-membered ring and the alkyl chain. This MO is the sigma antibonding orbital created from the four nitrogen lone pairs coordinated to the metal ion and their overlap with the $5d_{xz}$ atomic orbital of the Au(III) ion. The LUMO+2 orbital comprises π-orbitals centred on the indazole rings with a significant component of the d_{xz} orbital of the Au(III) ion. The LUMO+2 is vacant (antibonding) and derived from the mixing of the Au(III) d_{xz} with the ligand π-orbitals. Table 4.9 below shows the DFT-calculated transitions and assignments for the cation of $[Au(PrMe_2Indz)]PF_6$.

Table 4.9. The main DFT-calculated transitions and assignments for the cation of [Au(PrMe$_2$Indz)]PF$_6$ in a DMSO solvent continuum.*

Energy (cm-1)	Wavelength (nm)	Oscillator Strength	Symmetry	Major contributions	Minor contributions
22188	450.7	0.1008	Singlet-A	H-1->LUMO (96%)	HOMO->L+2 (2%)
22379	446.9	0.0687	Singlet-A	HOMO->LUMO (98%)	
27395	365.0	0.1783	Singlet-A	HOMO->L+2 (81%)	H-6->L+1 (3%), H-3->LUMO (4%), H-2->L+1 (9%)
28950	345.4	0.3253	Singlet-A	H-2->LUMO (97%)	
30218	330.9	0.1373	Singlet-A	H-3->LUMO (92%)	HOMO->L+2 (4%)
36801	271.7	0.1643	Singlet-A	H-6->L+1 (38%), H-4->LUMO (52%)	HOMO->L+2 (2%)
37740	265.0	0.269	Singlet-A	H-7->L+1 (65%), H-5->LUMO (26%)	H-3->L+2 (3%)
39990	250.1	0.3079	Singlet-A	H-4->L+2 (15%), H-1->L+3 (42%), HOMO->L+4(35%)	
40606	246.3	0.2353	Singlet-A	H-15->L+1 (13%), H-9->L+1 (13%), H-4->L+2 (55%)	H-1->L+3 (2%), HOMO->L+4 (9%)
41942	238.4	0.144	Singlet-A	H-5->L+2 (76%)	H-6->L+1 (4%), H-6->L+2 (4%), H-1->L+4 (6%), HOMO->L+3 (3%)

According to the assignments, peak 1 at 550 nm is due to two transitions: HOMO-1 to LUMO and HOMO to LUMO. Agreement between DFT and experiment is better for peaks at higher energy. The plot of transitions is also shown in Figure 4.15 below and it shows in vertical lines how many transitions are responsible for each peak.

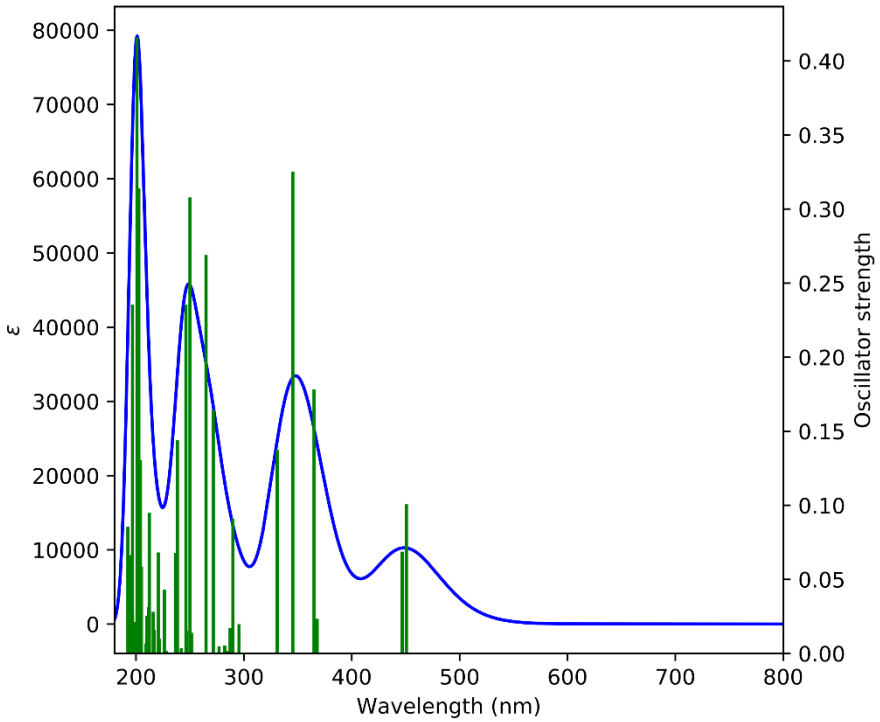

Figure 4.15: The plot of DFT-calculated transitions for [Au($PrMe_2$Ind)]PF_6.

4.5.2.4. Results for NMR calculations

The same level of theory used for geometry optimization and determination of IR and UV-vis spectra, HSEHIPBE/SDD, was used to calculate the ^{1}H and ^{13}C NMR spectra for Au(III) chelates. To account for any solvent effects, the DMSO solvent model was incorporated into the DFT calculation and TMS was used as a reference. The chemical shift of TMS was calculated at the HSEHIPBE/SDD GIAO level of theory. The chemical shifts of the experimental and the calculated Au(III) chelates were compared in this section to determine the correlation between them.

The correlation between the two sets of chemical shifts was relatively good with [Au($PrMe_2$Indz)]PF_6 having an average absolute percentage difference of 8.35% for ^{1}H NMR data and 4.88% for the ^{13}C NMR data. Table 4.12 below shows the chemical shifts for the calculated and the experimental data. The labeling scheme for [Au($PrMe_2$Indz)]PF_6 is shown in Figure 4.16 below and they correspond to the chemical shifts indicated in Table 4.10.

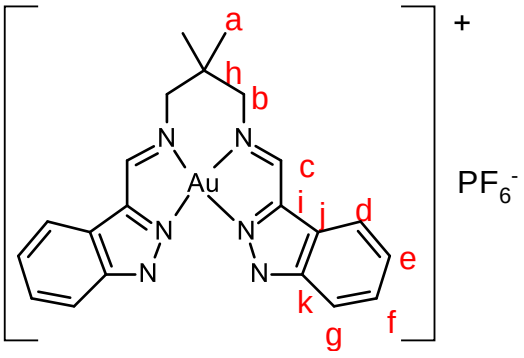

[Au(PrMe$_2$Indz)]PF$_6$

Figure 4.16: Labeling scheme for [Au(PrMe$_2$Indz)]PF$_6$.

Table 4.10: Experimental and DFT-calculated 1H and 13C NMR chemical shifts for [Au(PrMe$_2$Indz)]PF$_6$.

Proton	Exp	Calc	%Diff*	Carbon	Exp	Calc	%Diff*
a	1.24	1.36	-9.68	**a**	23.59	27.30	-15.73
b	3.72	4.10	-10.22	**h**	N/A	44.91	N/A
c	9.17	9.25	-0.87	**b**	62.83	69.90	-11.25
d	8.03	8.60	-7.10	**d**	119.59	122.83	-2.71
e	7.48	8.38	-12.03	**j**	120.61	123.59	-2.47
f	7.51	8.36	-11.32	**g**	123.98	125.57	-1.28
g	8.16	8.75	-7.23	**f**	126.74	130.81	-3.21
				e	127.98	134.55	-5.13
				i	139.24	141.49	-1.62
				k	148.78	156.26	-5.03
				c	164.48	165.08	-0.36

%Diff = ((exp-calc)/exp)×100

*N/A means that the signal was not detected by the instrument

The calculated ^{1}H NMR chemical shifts for [Au(PrMe$_2$Indz)]PF$_6$ appear to be consistently overestimated compared to the experimental chemical shifts. The comparison between the two, however, looks very good, as the absolute percentage differences are low. The absolute percentage difference for the imine peak (**c**) is the lowest (0.87%); this implies that the calculations estimated it accurately. The largest difference is between the calculated and the experimental chemical shift of the aromatic proton (**e**) (12.03%). Otherwise, all the other chemical shifts were in good agreement.

Similar to the calculated ^{1}H NMR shifts, the DFT calculations overestimated all the calculated ^{13}C NMR chemical signals for [Au(PrMe$_2$Indz)]PF$_6$ compared to the experimental data. The imine carbon peak (**c**) appears to have the lowest absolute percentage difference (0.30%) while the dimethyl and the CH_2 carbons (**a** and **b**) have the highest percentage differences, 15.73%, and 11.25%, respectively.

The absolute percentage differences, however, are still low on average, which indicates that the two results compare favorably overall. The sp^3 carbon (**h**) could not be detected on the experimental spectrum although it appears on the calculated spectrum.

The relationship between the experimental and the calculated data for the ^{1}H NMR and ^{13}C NMR spectra of [Au(PrMe$_2$Indz)]PF$_6$ was determined by linear plots, as shown in Figure 4.17 below.

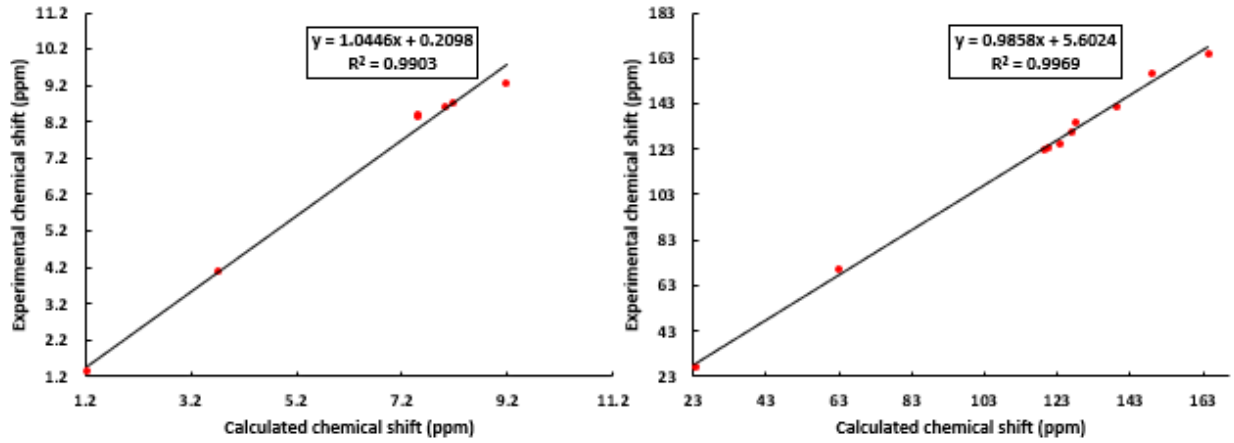

Figure 4.17: Plots showing a correlation between experimental and DFT-calculated chemical shifts for the H^1 NMR (a) and ^{13}C NMR spectra of [Au(PrMe$_2$Indz)]PF$_6$.

The plots indicate that there is a linear relationship between the experiment and the calculated ^{1}H NMR and ^{13}C NMR data for [Au(PrMe$_2$Indz)]PF$_6$. The correlation coefficients of both data sets are indicated in the plots. Since both the correlation coefficients are very close to one, it means that the correlation between experimental and the calculated data for both ^{1}H NMR and ^{13}C NMR spectra is fairly good. The DFT-calculated NMR data of [Au(PrMe$_2$Indz)]PF$_6$ was compared with the DFT-calculated NMR data of Au(L1)]PF$_6$ which was calculated at PBEPBE/LANL2DZ level of theory.[7] The TMS reference was also calculated at the same level of theory. For this compound, it is apparent that the DFT-calculations over and underestimate the chemical shifts of both the ^{1}H and ^{13}C spectra compared to the experimental spectra.

The average percentage difference for ^{1}H and ^{13}C were 3.57% and 4.48%, respectively. These values are low compared to those obtained in this work.[7] The PBEPBE/LANL2DZ method, therefore, appears to have estimated the NMR data more accurately compared to the method used in this work, HSEHIPBE/SDD. This means that the difference between that calculated data and the experimental data is small compared to that of the NMR data in this work.

4.6. Conclusions

DFT simulations were employed in this work to calculate the electronic properties of bis(indazolide-imine) Au(III) chelates. These included geometry optimization, vibrational spectra, electronic transitions, and the NMR shielding tensors. The DFT-calculated data were compared with the experimental data to evaluate the correlation between them.Geometry optimization data revealed a good correlation between the DFT-calculated and the X-ray structure. The bond distances and bond angles of the two structures were very close to one another with small percentage differences. The RMSD value of the two structures obtained was also very small, indicating that the calculations were accurate.

A comparison between the experimental and the calculated vibrational data showed that DFT calculations consistently overestimated the calculations. However, there was still a good correlation between the intensities and the frequencies of the simulations and the experiment. A correlation plot between the experimental and the calculated frequencies was linear with a correlation coefficient close to one. This confirmed an excellent correlation between the two frequencies. It also implies that any discrepancies detected can be accounted for. The electronic transition results for the calculated data were slightly overestimated compared to the experimental spectrum. The calculated spectrum displayed a hypsochromic shift relative to the experimental spectrum. All the orbitals involved in most of the chelates' electronic transitions were mostly π-symmetry except for the LUMO+1 MO which has a substantial d_{xy} atomic orbital character.

The ^{1}H and ^{13}C NMR shielding tensors were calculated and the chemical shifts were compared to the experimental chemical shifts. In most cases, the calculated chemical shifts were overestimated with slight percentage differences for both ^{1}H and ^{13}C NMR. In general, however, there was a good agreement between the experimental and the calculated NMR data. The correlation plot yielded a linear trend with correlation coefficients very close to 1.

4.7. References

(1) Akerman, K.J., Fagenson, A.M., Cyril, V., Taylor, M., Muller, M.T., Akerman, M.P. and Munro, O.Q., 2014. Gold (III) macrocycles: nucleotide-specific unconventional catalytic inhibitors of human topoisomerase I. *Journal of the American Chemical Society*, *136*(15), pp.5670–5682.

(2) Allen, F.H., Kennard, O., Watson, D.G., Brammer, L., Orpen, A.G. and Taylor, R., 1987. Tables of bond lengths determined by X-ray and neutron diffraction. Part 1. Bond lengths in organic compounds. *Journal of the Chemical Society, Perkin Transactions 2*, (12), pp.1–19.

(3) Defazio, S., Tamasi, G. and Cini, R., 2005. A molecular orbital study of C–H···Cl⁻and N–H···Cl⁻hydrogen bonds. Inferences on selected metal complexes and on protein ClC Cl–channels. *Comptes Rendus Chimie*, *8*(9-10), pp.1584-1609.

(4) Band, Y. B., & Avishai, Y., Chapter 15 - Density Functional Theory (2013) *Quantum Mechanics with Applications to Nanotechnology and Information Science*. pp.871–889.

(5) Jensen, F., Introduction to Computational Chemistry. 2007. *West Sussex, England: John Wiley & Sons Ltd*, pp.30–34.

(6) Bordogna, A., Pandini, A. and Bonati, L., 2011. Predicting the accuracy of protein–ligand docking on homology models. *Journal of Computational Chemistry*, *32*(1), pp.81-98.

(7) Ackerman K.J., Structural, Physical and Biological Studies of Gold (III) Bis (Pyrrolide-Imine) Schiff Base Macrocyclic and Pseudomacrocyclic Complexes: Targeted Chemotherapeutic Agents. 2013. phD *Thesis.* University of KwaZulu-Natal.

Chapter 5

Biological studies

5.1. Introduction

This chapter is intended to discuss the experimental data obtained investigating the DNA binding mode of the two successfully synthesized Au(III) chelates, [Au(PrMe$_2$Indz)]PF$_6$, and [Au(PrOHIndz)]PF$_6$, as well as their cytotoxicity. Generally, compounds bind the DNA in three diverse ways; minor or major groove, intercalation, and electrostatically.[1] Intercalation mode, however, is the binding mode of interest in this work. This is because the design of the chelates of interest is suitable for π-π stacking interactions between the DNA base pairs due to their planar geometry. Intercalative binding induces unwinding and lengthening the DNA helix to accommodate the intercalating compound, this causes conformational changes that result in the inhibition of cellular processes such as replication, transcription and DNA repair thus making intercalators potential anticancer agents.[1]

Three different DNA binding studies, namely: electrophoretic mobility shift assays, absorbance titrations, and viscometry, were conducted experimentally to determine the DNA binding mode of the Au(III) chelates and are fully discussed in this chapter. The last part of this chapter evaluates the cytotoxicity of the two Au(III) chelates on two different breast cancer cell lines: MDA-MB-231 cells, MCF-7 cells, and one normal cell line, HEK-293. This was carried out by MTT (3-(4,5-dimethylthiazol-z-yl)-2,5-diphenyltetrazolium bromide) assays.[2]

5.2. Electrophoretic Mobility Shift Assay (EMSA)

Electrophoretic mobility shift assay (EMSA) is the electrophoretic segregation of bound DNA molecules in an agarose gel, the DNA can either be bound to the associated protein or drug molecules. This concept was first introduced by Fried and Crothers and Garner and Revzin in their studies on RNA polymerase interaction with the *lac* promoter. Since then this concept has been applied extensively in biochemistry.[3]

In this study, EMSA was used to determine the binding mode of the newly synthesized Au(III) chelates. The technique relies on the movement of the DNA through a nondenaturing agarose gel. In the presence of a drug molecule, the DNA movement gets retarded or enhanced as the drug molecule binds to it, thereby altering the structure of the macromolecule and its hydrodynamic radius. DNA-drug interaction is therefore characterized by observing a series of discrete DNA bands shifts on a gel which convey the association of the drug compound with the DNA.[3] The EMSA was conducted with a pUC57 plasmid DNA substrate to prove that the two successfully synthesized Au(III) chelates bind the DNA through intercalation as hypothesized. The varying concentrations of the Au(III) chelates, [Au($PrMe_2$Indz)]PF_6, and [Au(PrOHIndz)]PF_6, ethidium bromide (EB, a well-known DNA intercalator) and Hoechst 33258 (a well-known groove binder) were applied. Figure 5.1 below shows the gel images of these compounds.

The gel images indicate retardation of mobility on nicked open circular (NOC) DNA and supercoiled (SC) DNA bands with increasing concentrations of EB. The NOC DNA band on the gel shows a retarded migration below 10 µM for both Au(III) chelates, which then shifts to more enhanced migration or a more compact looking band at 50 and 100 µM (lane 10 and 11). This suggests intercalative binding at lower concentrations of added compounds and groove binding at higher concentrations.

The magnitude of the mobility shift difference (for EB and Au(III) chelates) on the SC bands, could result due to various factors such as the size difference between the EB and Au(III) chelates, their DNA binding affinity, as well as the sites and the extent of DNA intercalation. The Au(III) chelates seem to exhibit higher mobility shifts at lower concentrations than EB, which implies that they bind DNA more strongly than EB. No mobility retardation is observed on the SC DNA and NOC DNA bands as the concentration of Hoechst 33258 (lane 12 to 14) increases. This is because Hoechst 33258 is a groove binder and does not affect the size of the DNA.[9]

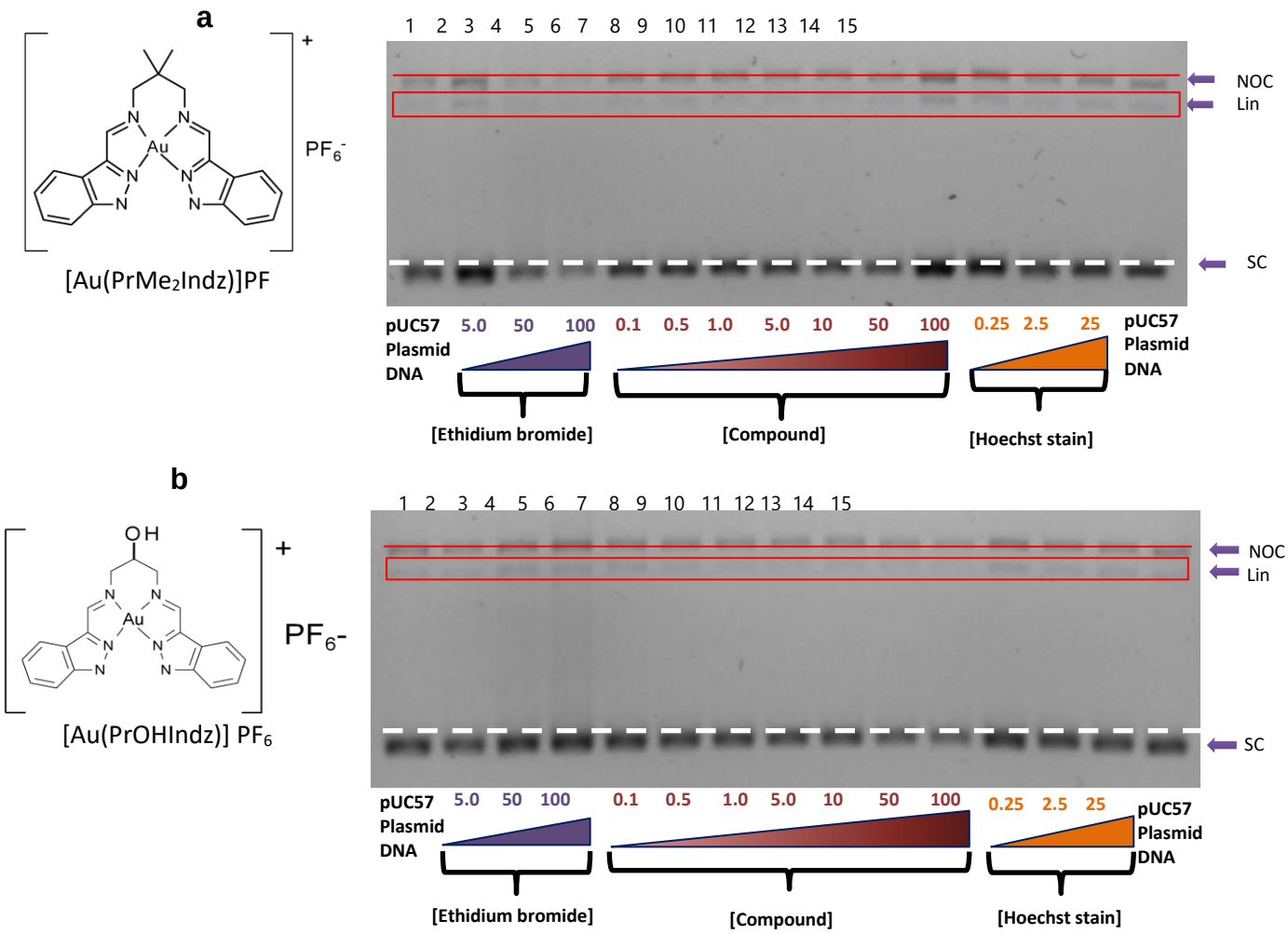

Figure 5.1: Electrophoretic mobility shift assay of a) $[Au(PrMe_2Indz)]PF_6$ and b) $[Au(PrOHIndz)]PF_6$ with pUC57 plasmid DNA. All gel electrophoresis experiments were carried out using hand-cast 1.25% agarose gels dissolved in 1x TAE buffer. 50 ng of DNA was added per lane and gels were run at a voltage of 65 V at 37 °C. Ethidium Bromide solution was used to stain the gels for 30 minutes.

5.3. Titration absorbance spectroscopy

Titration absorbance spectroscopy is the most effective method typically used to determine the DNA binding modes of metal complexes. The binding of metal complexes to the DNA is often, but not always, characterized by hypochromism (decrease in absorbance) and red-shift (shift towards high wavelength) caused by the stacking interaction of aromatic chromophores of the DNA and the metal complex.[4]

In this work, calf thymus DNA (ctDNA) was added in increasing amounts into a solution with a fixed compound concentration. The absorption spectra of both Au(III) chelates investigated were very similar and the absorption spectrum of [Au(PrMe$_2$Indz)]PF$_6$ is shown in Figure 5.2 below as a representative of both Au(III) chelates. See the absorption spectra for [Au(PrOHIndz)]PF$_6$ in Appendix F.

The spectrum indicates a hypochromic effect in the MLCT region of the spectrum with increasing DNA concentration; this suggests strong interactions between the aromatic chromophores of the complex and the DNA base pairs. Since the spectrum does not show an obvious red-shift, it is a clear indication that [Au(PrMe$_2$Indz)]PF$_6$ binds the DNA through intercalation, during which process electron density is transferred into the compound's antibonding π-orbitals, reducing the transition probabilities and consequently causing hypochromism.[5] These results are very consistent with the EMSA results which also suggest intercalation as the main binding mode.[5]

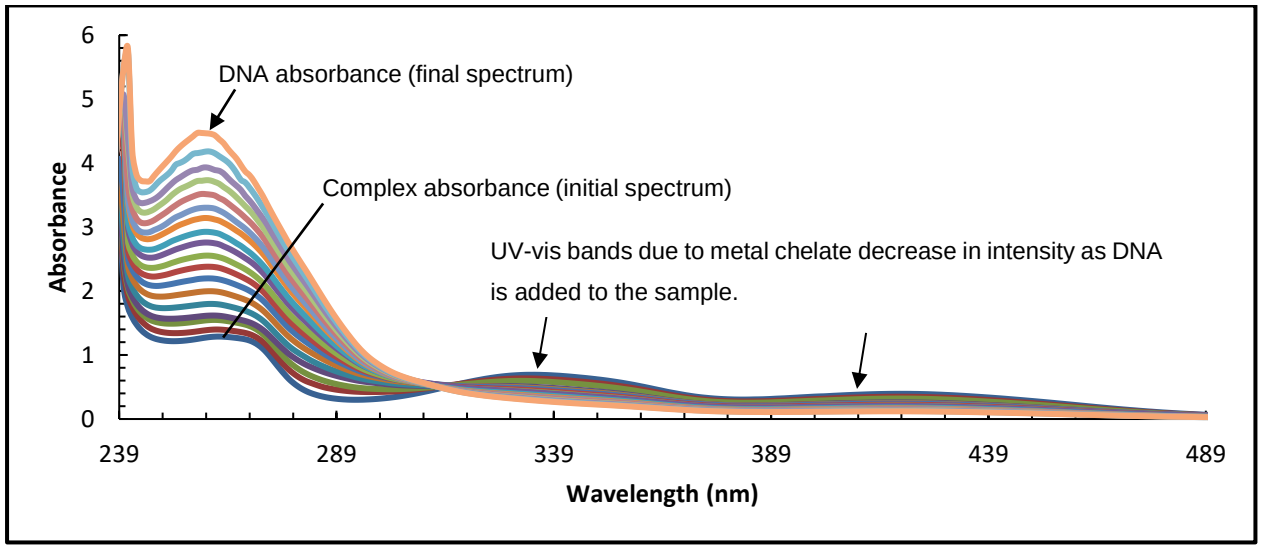

Figure 5.2: Sequential absorption spectra of [Au(PrMe$_2$Indz)]PF$_6$ in the presence and absence of ctDNA. The experiment was performed in 0.100 M pH 7.0 TRIS-HCl Buffer with 10% DMSO at 37 °C.

The binding equilibrium of the Au(III) chelates was modeled by the Hill equation. The binding curve of [Au(PrMe$_2$Indz)]PF$_6$ is shown in Figure 5.3 below. The spectrum is very similar to that of [Au(PrOHIndz)]PF$_6$ (shown in appendix F). This compound binds to the DNA with an association constant K_a of 1.39×10^7 M^{-1} and the Hill coefficient of 0.58 ± 0.06 which is indicative of a broad sigmoidal curve in which no cooperativity in the binding exists. This implies that the binding of the first chelate molecule to the DNA substrate does not influence the binding of subsequent chelates. The Hill function obtained is a single sigmoidal curve meaning that intercalation (as indicated by EMSA studies) is probably the main binding mode involved.

The low value of the Hill coefficient and shallow curvature of the plot could indicate that there are multiple binding sites and potential binding orientations for the planar Au(III) chelate. It also suggests intercalative binding at a low concentration of the added compound (and that the binding constant is high) and groove binding at higher compound concentrations (lower binding constant), consistent with gel results. There may also be little or no base pair specificity for the intercalative binding interaction. This suggests multiple intercalative binding modes at low drug concentrations that transition into multiple groove binding modes at higher drug concentrations. Future work would include using molecular simulations to shed further light on the matter.

The Hill coefficient of $n < 1$ indicates that the binding of the complex at sub-saturation levels of the target sites causes a conformational change in the DNA that reduces the affinity of the target binding sites for the incoming complex (negative cooperativity). This means that concentrations of the complex must be further increased to achieve saturation. This could happen with a cationic complex because adding cations to the DNA neutralizes the negative charge on the DNA and this is expected to reduce the electrostatic attraction between the partly saturated DNA polymer and the unbound cationic complexes in solution.

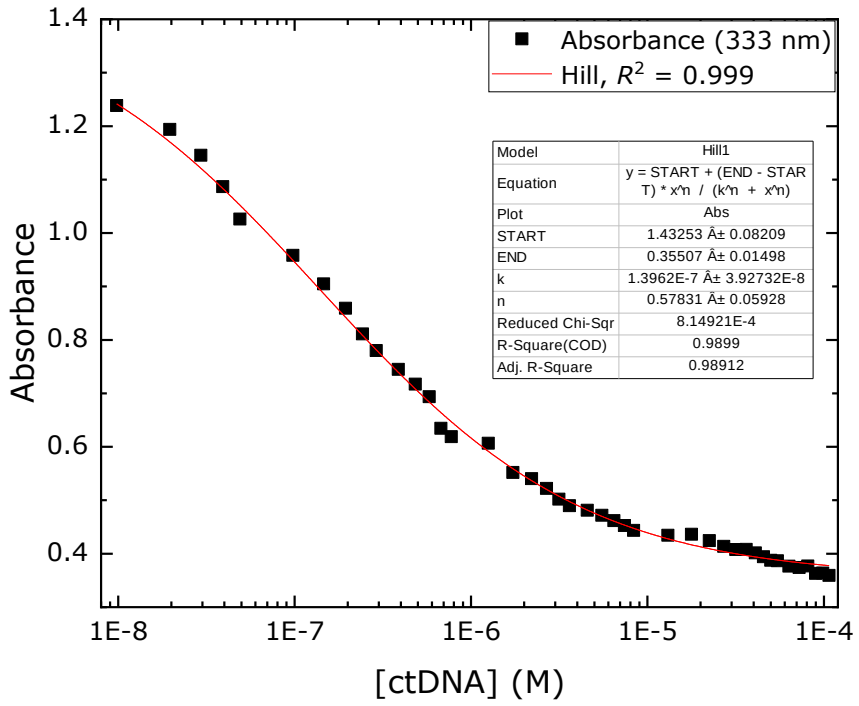

Figure 5.3: Non-linear least-squares fit of the Hill function to the spectroscopic data at 333 nm for the titration of [Au(PrMe$_2$Indz)]PF$_6$ with ctDNA at 37 ^{o}C.

The association constants of the Au(III) chelates were compared to those of other intercalators, such as Ru(II) complexes, [Ru(L)$_4$(dppz)]$^{2+}$, which also bind the DNA through stacking interactions.[6] Table 5.1 below presents the association constants of Au(III) complexes and Ru(II) complexes.

Table 5.1. The binding constants (K_a) of Au(III) chelates and Ru(II) complexes.

Compound	Binding constant (K_a)
[Au(PrMe$_2$Indz)]PF$_6$	7.19 ×10^6 M^{-1}
[Au(PrOHIndz)]PF$_6$	6.76×10^5 M^{-1}
[Ru(Im)$_4$(dppz)]$^{2+}$	4.44 ×10^5 M^{-1}
[Ru(MeIm)$_4$(dppz)]$^{2+}$	9.09 × 10^5 M^{-1}

*Im = imidazole, MeIm = methylimidazole, dppz = dipyrido[3,2-a:2′ ,3′ -c]phenazine

The binding constant of [Au(PrMe$_2$Indz)]PF$_6$ is greater than that of [Au(PrOHIndz)]PF$_6$ as well those of Ru(II) complexes, indicating that its DNA binding affinity is stronger than that of [Au(PrOHIndz)]PF$_6$ and the literature reported Ru(II) complexes. The binding constant of [Au(PrOHIndz)]PF$_6$, however, is comparable to those of Ru(II) chelates.

The higher binding constant of [Au(PrMe$_2$Indz)]PF$_6$, indicates that its dimethyl substituent enhances the binding of the drug compared with the hydroxyl substituent since the Au(III) chelates have similar ligand scaffolds. The binding constant of the classical DNA intercalator,

EB, was reported to be 1.23 X 10^5 M^{-1}, [7,8] which is lower in magnitude compared with those of the Au(III) chelates. This proves that the Au(III) chelates have improved binding affinity and this is consistent with electrophoretic mobility assay results which show that Au(III) chelates induce greater DNA mobility shifts than EB at lower concentration meaning that they bind to the DNA more strongly than EB.

5.4. Viscometry

Viscometry uses hydrodynamic measurements that are responsive to DNA length changes. It is less ambiguous and the most critical test of a binding model.[4,5] In the case of intercalation, it is anticipated that the DNA length increases as the base pairs move apart to accommodate the drug compound, and so this will necessarily increase the DNA viscosity.[5] A non-intercalative compound, however, could cause a kink or a bend on the DNA helix causing an overall decrease in its length and viscosity subsequently. The compounds that bind exclusively on the DNA helix groove are called DNA groove binders; these compounds have less significant effects to no effects on the DNA helix length and its viscosity.[4]

Viscosity measurements were undertaken to determine the binding modes of two successfully synthesized Au(III) chelates. EB, a well-known DNA intercalator, and Hoechst 33258, a well-known groove binder were included in the experiment for comparison purposes.[5,10] Specific viscosity ($(\eta - \eta_0/\eta_0)^{1/3}$) is plotted against the concentration ratio of the drug compound and the ctDNA in Figure 5.4 below. As expected, EB increases the relative viscosity of ctDNA; this implies that it intercalates between the DNA base pairs thus increasing its length, this trend is very consistent with the literature.[5,9,10] Hoechst 33258, a proven groove binder, indicates less significant changes in the relative viscosity (the curve is almost flat) simply because it does not insert into the DNA helix and thus causes less significant changes on the ctDNA length.[5]

The viscosity plots of the metal chelates, $[Au(PrMe_2Indz)]PF_6$ and $[Au(PrOHIndz)]PF_6$, indicate that the two Au(III) complexes cause the ctDNA viscosity to increase; this trend is very similar to that of EB rather than Hoeschst 33258, which suggests that both Au(III) chelates are DNA intercalators.

The two Au(III) chelates appear to be better intercalators than EB as their increase in the relative viscosity is more pronounced than that of EB. This observation is consistent with electrophoretic experiments which suggest intercalation at lower loading of the compounds. It is not easy, however, to tell from this experiment if there are two binding modes (as suggested by electrophoretic experiments) as the experiment did not go high enough in a mole ratio to reach the region where viscosity begins to stop rising as groove binding becomes predominant.

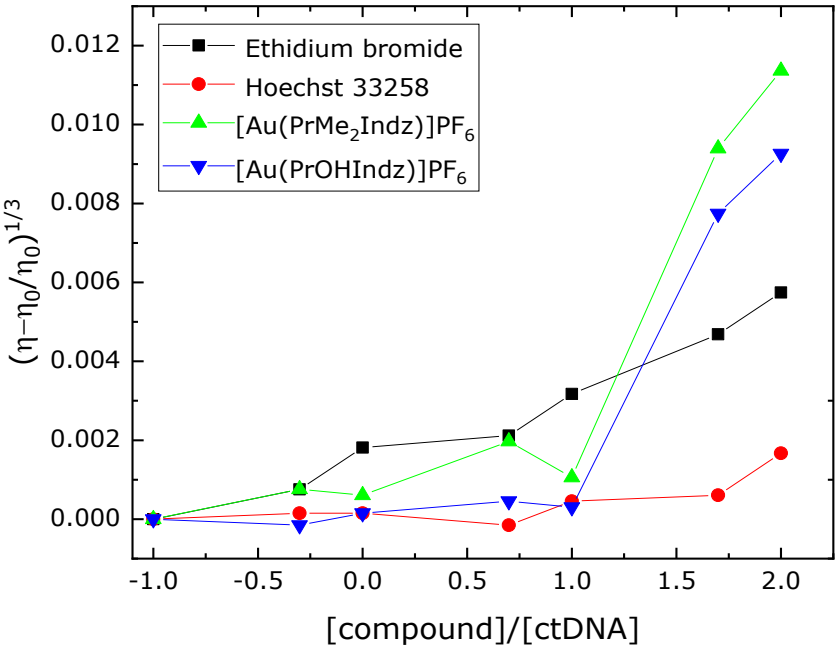

Figure 5.4: Viscosity plots showing the change in viscosity with increasing concentration of test compounds and controls. Viscosity is represented as a specific viscosity ($(\eta- \eta_0/\eta_0)^{1/3}$). Data are shown for EB (well-known intercalator), Hoechst 33258 (well-known groove binder), and $[Au(PrMe_2Indz)]PF_6$ and $[Au(PrOHIndz)]PF_6$.

The Au(III) compounds in this work behave similarly to the literature reported organic bioactive dibenzodioxides and phenazines which are also DNA intercalators.[11] The increasing concentrations of these compounds also increase the DNA solution viscosity.[11] These compounds, however, were reported to intercalate the DNA less strongly than EB, hence our data implies the Au(III) compounds are stronger DNA intercalators than the literature compounds.

Au(III) chelates were also compared to other metal chelates that are DNA intercalators. These compounds are $[Ru(bpy)_2(dpoq)]^{2+}$, where bpy = bipyridines and dpoq = dipyrido[1,2,5]oxadiazolo[3,4-b]quinoxaline and $[Ru(phen)_2(dpoq)]^{2+}$, where phen = 1,10-phenanthroline.[5] These compounds were also reported to steadily increase the relative viscosity of the DNA just like EB. Their increase in relative velocity, however, is lower than that of EB, meaning that they also intercalate the DNA less strongly than the Au(III) compounds reported in this work.[5]

5.5. Whole-cell cytotoxicity

This section reports the cytotoxicity of the two successfully synthesized bis(indazolide-imine) Au(III) chelates with non-toxic bio-compatible PF_6^- counterions, namely: $[Au(PrMe_2Indz)]PF_6$ and $[Au(PrOHIndz)]PF_6$ on two different breast cancer cell lines: MDA-MB-231 cells (TNBC), and estrogen receptor-positive (ER+) MCF-7 cells as well as one normal cell line, HEK-293. These cell lines were treated with increasing concentrations of the test compounds for 24 hours. Cisplatin was used as a positive control. The MTT (4,5-dimethylthiazol-2-yl)-2,5-diphenyltetrazolium bromide assay was carried out on these cell lines to determine the percentage viability of cells in vitro by measuring the cell's metabolic activities.

The MTT assay is a colorimetric assay that relies on the reduction of a tetrazolium salt (yellow) (MTT reagent) to formazan crystals (purple) by NAD(P)H-dependent oxidoreductase enzymes found in living cells.[12] The formazan crystals are dissolved in a solubilizing solution before the optical density of each well on the plate reader could be determined at 570 nm.[12] The greater the intensity of the purple colour, the greater the number of viable cells.

Figure 5.5 below shows the dose-response curves for Au(III) chelates and cisplatin for the breast cancer cell line MDA-MB-231. The curves give percentage cell survival as a function of drug concentration measured by the MTT assay method.

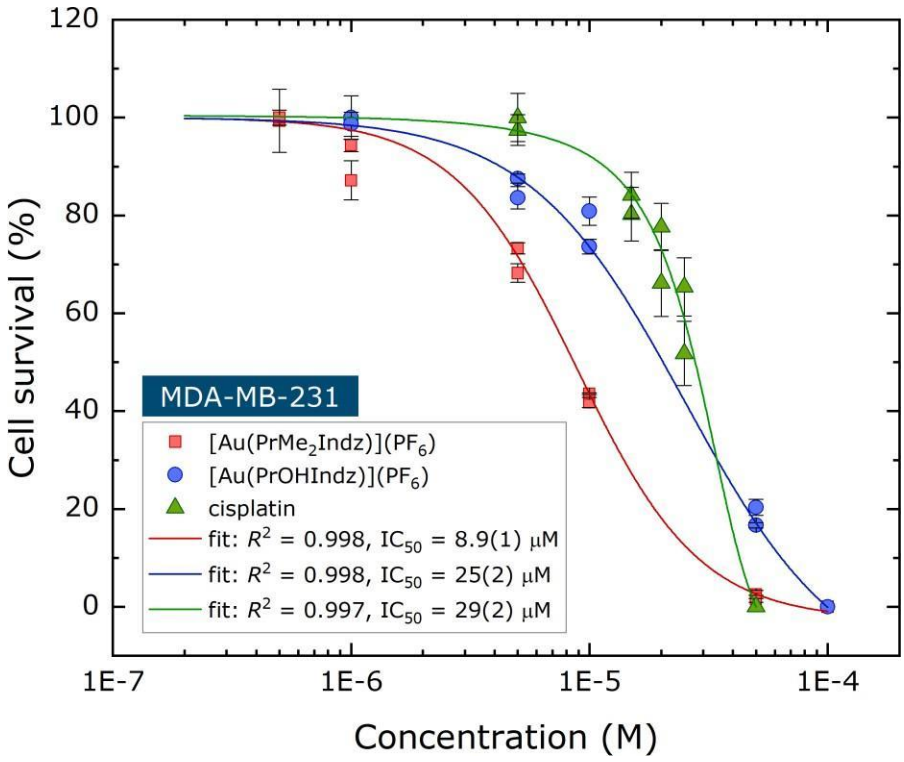

Figure 5.5: Plot of cell survival (%) as a function of drug/compound concentration measured via the MTT assay method. For each compound, data from two independent experiments are shown and each point represents the average measured from three independent cell colonies (wells).

The steepness of the curves indicates that higher concentrations of these drugs are required at the beginning to induce cell death. Small increments then further lead to increased cell mortality. $[Au(PrMe_2Indz)]PF_6$, amongst all, is more effective towards breast cancer cells with the IC_{50} of 8.9 µM. The IC_{50} is the concentration of the drug required to induce 50% cell growth inhibition. $[Au(PrOHIndz)]PF_6$ on the other hand required 25 µM to induce 50% cell death of MDA-MB-231. Cisplatin proves to be less effective towards MDA-MB-231 compared to the Au(III) chelates, with the IC_{50} of 29 µM.

Table 5.2 below gives the cytotoxicity data (IC_{50} values) for Au(III) chelates (including literature reported Au(III) chelates) and cisplatin against MDA-MB 231, MCF-7, and HEK-239 cancer cell lines.

Table 5.2: Cytotoxicity data (IC_{50} values) for Au(III) chelates and cisplatin against MDA-MB 231, MCF-7, and HEK-239 cancer cell lines. Estimated standard uncertainties are given in parentheses.

Compound	MDA-MB-231 / μM	MCF-7 / μM	HEK-293 / μM
$[Au(PrMe_2Indz)]PF_6$	8.9(1)	14(2)	16.5(3)
$[Au(PrOHIndz)]PF_6$	25(2)	18.7(6)	25.2(2)
Cisplatin	29(2)	19(1)	51(3)
$AuCl_2(ppy)$	44.3(4)	77.9 (5)	N/A
Au(III) peptide bioconjugate	24.8(3)	12.5(1)	N/A

*ppy = 2-phenyl-pyridine

Interestingly, $[Au(PrMe_2Indz)]PF_6$ possesses 1.4 to 3.2 fold greater cytotoxicity than cisplatin across all cell lines. Although $[Au(PrOHIndz)]PF_6$ has lower cytotoxicity than $[Au(PrMe_2Indz)]PF_6$, it is still better than cisplatin in terms of cytotoxicity in all cell lines. $[Au(PrMe_2Indz)]PF_6$ appears to be more cytotoxic to MDA-MB-231 than any other cell line, it can therefore be considered for a hit to lead compound optimization as a potential chemotherapeutic agent for triple-negative breast cancer (TNBC) cell lines. The key strategy going forward will be to enhance the therapeutic index from ca. 2 to approx. 10-20. The structural modifications to the compound required to achieve this are, however, currently unknown and require numerous compound analogs to generate appropriate quantitative structure-activity relationship (QSAR) data to guide the process.

$[Au(PrOHIndz)]PF_6$ shows about the same selectivity as cisplatin toward the MCF-7 cell line. Its cytotoxicity toward MDA-MD-231 and HEK-293 cell lines, however, is the same, this is a problem because it means that $[Au(PrOHIndz)]PF_6$ is likely to exert equal cytotoxicity to both MDA-MB-231 and normal cell line HEK-293 if used as a chemotherapeutic agent for MCF-7.

The IC_{50} of the Au(III) chelates in this work were compared with the IC_{50} values of other Au(III) chelates reported in the literature, these are $[AuCl_2(ppy)]$ and an Au(III) peptide bioconjugate; their IC_{50} values are shown in Table 5.4 above.[13] $[AuCl_2(ppy)]$ appears to have exhibited lower cytotoxicity than both Au(III) chelates in this work as well as cisplatin. The Au(III) peptide bioconjugate was derived from $[AuCl_2(ppy)]$ by incorporating a peptide chain LTVSPWY.[13] This is after $[AuCl_2(ppy)]$ proved to have cytotoxic effects on cancer cells. Its IC_{50} values for MDA-MD-231 and MFC-7 are 24.8(3) μM and 12.5(1) μM, respectively.[13]

These values show that the Au(III) peptide bioconjugate is more cytotoxic than cisplatin towards MCF-7 and MDA-MD-231 compared to all the compounds mentioned. It is also more cytotoxic towards MDA-MD-231 than [$AuCl_2$(ppy)], cisplatin and [Au(PrOHIndz)]PF_6. [$AuCl_2$(ppy)] and Au(III) peptide bioconjugate were evaluated against the normal human cells Fibroblast cell lines (GM56575), instead of HEK-293 cell line; their IC_{50} values were 50.8 µM and 11.5 µM, respectively.[13] Unfortunately, these compounds exhibit higher cytotoxicity towards normal human cells as well. This means that they lack specificity towards cancer cells only, therefore, their use as chemotherapeutic agents would be problematic.[13]

5.6. Conclusion

The purpose of this chapter was to determine the binding mode and the cytotoxicity (and hence anticancer drug potential) of the two successfully synthesized Au(III) chelates. DNA binding studies (two experiment methods, namely gel electrophoresis and spectroscopic titration) were in accord with each other as they suggested a possibility of two binding modes which are intercalation and groove binding. This was deduced from agarose gel EMSA experiments whereby retardation in mobility was observed below 10 µM Au(III) chelate concentration (suggesting intercalation which causes mobility retardation as the drug binds between the bases and increases the length and the size of the DNA molecule), and a sudden shift to a more advanced migration at 50 and 100 µM (suggesting groove binding, which does not affect the size or the length of the DNA molecule). This suggested intercalative binding at lower concentrations of added compound and groove binding at higher compound concentration. The spectroscopic titration produced a broad Hill curve which also suggests intercalative and groove binding modes. Some computational molecular docking data, however, will be required to confirm this. Viscosity measurements, however, suggested intercalation as the main binding mode. Although the replicates for viscosity measurements were too few to conclude that there is only one binding mode.

The cytotoxicity of the two chelates was investigated by screening them against two human breast cancer cell lines, MDA-MB-231 and MCF-7, and one normal human cell line, HEK-293. According to the results, [Au($PrMe_2$Indz)]PF_6 was more selective toward MDA-MB-231 and MCF-7 than [Au(PrOHIndz)]PF_6. [Au(PrOHIndz)]PF_6, however, displayed greater cytotoxicity than cisplatin against both breast cancer cell lines. [Au($PrMe_2$Indz)]PF_6 exhibited higher cytotoxicity toward MDA-MB-231 than any other cell line, it can therefore be considered for a hit to lead compound optimization as a potential chemotherapeutic agent for triple-negative breast cancer (TNBC) cell lines.

5.7. References

(1) Shoute, L.C. and Loppnow, G.R., 2018. Characterization of the binding interactions between EvaGreen dye and dsDNA. *Physical Chemistry Chemical Physics*, *20*(7), pp.4772-4780.

(2) Sagar, S., Esau, L., Moosa, B., Khashab, N.M., Bajic, V.B. and Kaur, M., 2014. Cytotoxicity and apoptosis induced by a plumbagin derivative in estrogen positive MCF-7 breast cancer cells. *Anti-Cancer Agents in Medicinal Chemistry (Formerly Current Medicinal Chemistry-Anti-Cancer Agents)*, *14*(1), pp.170-180.

(3) Kerr, L.D., 1995. [42] Electrophoretic mobility shift assay. In *Methods in Enzymology* (Vol. 254, pp. 619-632). Academic Press.

(4) Shahabadi, N. and Heidari, L., 2014. Synthesis, characterization and multi-spectroscopic DNA interaction studies of a new platinum complex containing the drug metformin. *Spectrochimica Acta Part A: Molecular and Biomolecular Spectroscopy*, *128*, pp.377-385.

(5) Peng, B., Chen, X., Du, K.J., Yu, B.L., Chao, H. and Ji, L.N., 2009. Synthesis, characterization and DNA-binding studies of ruthenium (II) mixed-ligand complexes containing dipyrido [1, 2, 5] oxadiazolo [3, 4-b] quinoxaline. *Spectrochimica Acta Part A: Molecular and Biomolecular Spectroscopy*, *74*(4), pp.896-901.

(6) Chen, L.M., Liu, J., Chen, J.C., Tan, C.P., Shi, S., Zheng, K.C. and Ji, L.N., 2008. Synthesis, characterization, DNA-binding and spectral properties of complexes [Ru (L) 4 (dppz)] 2+(L= Im and MeIm). *Journal of Inorganic Biochemistry*, *102*(2), pp.330-341.

(7) İnci, D., Aydın, R., Vatan, Ö., Huriyet, H., Zorlu, Y., Çoşut, B. and Çinkılıç, N., 2019. Cu (II) tyrosinate complexes containing methyl substituted phenanthrolines: Synthesis, X-ray crystal structures, biomolecular interactions, antioxidant activity, ROS generation and cytotoxicity. *Applied Organometallic Chemistry*, *33*(1), p.e4652.

(8) Kiraz, S., İnci, D., Aydın, R., Vatan, Ö., Zorlu, Y. and Cavaş, T., 2019. Antiproliferative activity of copper (II) glutamine complexes with N, N-donor ligands: Synthesis, characterization, potentiometric studies and DNA/BSA interactions. *Journal of Molecular Structure*, *1194*, pp.245-255.

(9) Sarwar, T., Rehman, S.U., Husain, M.A., Ishqi, H.M. and Tabish, M., 2015. Interaction of coumarin with calf thymus DNA: deciphering the mode of binding by in vitro studies. *International Journal of Biological Macromolecules*, *73*, pp.9-16.

(10) Kellett, A., Molphy, Z., Slator, C., McKee, V. and Farrell, N.P., 2019. Molecular methods for assessment of non-covalent metallodrug–DNA interactions. *Chemical Society Reviews*, *48*(4), pp.971-988.

(11) Phadte, A.A., Banerjee, S., Mate, N.A. and Banerjee, A., 2019. Spectroscopic and viscometric determination of DNA-binding modes of some bioactive dibenzodioxins and phenazines. *Biochemistry and Biophysics Reports*, *18*, p.100629.

(12) Chacon, E., Acosta, D. and Lemasters, J.J., 1997. Primary cultures of cardiac myocytes as in vitro models for pharmacological and toxicological assessments. In *In Vitro Methods in Pharmaceutical Research* (pp. 209-223). Academic Press.

(13) Śmiłowicz, D., Slootweg, J.C. and Metzler-Nolte, N., 2019. Bioconjugation of Cyclometalated Gold (III) Lipoic Acid Fragments to Linear and Cyclic Breast Cancer Targeting Peptides. *Molecular Pharmaceutics*, *16*(11), pp.4572-4581.

Chapter 6

Conclusions and Future Work

Four novel bis(indazole-imine) ligands have been synthesized in this work: H_2PrmeIndz, H_2PrMe$_2$Indz, H_2BuIndz and H_2PrOHIndz (Figure 6.1). These ligands are characterized by two indazole rings connected through a diimine bridge. Their structures are varied by changing the length of the diimine bridge and the substituents on the diimine bridge. Coordination of the Au(III) ion to the ligands results in concomitant deprotonation of two NH protons yielding a square-planar d^8 complex with a +1 charge. Chelation of the H_2PrmeIndz ligand, however, yielded a cation with the $AuCl_4^-$ anion which is not suitable for cells and could not be studied further, while chelation of H_2BuIndz was unsuccessful.

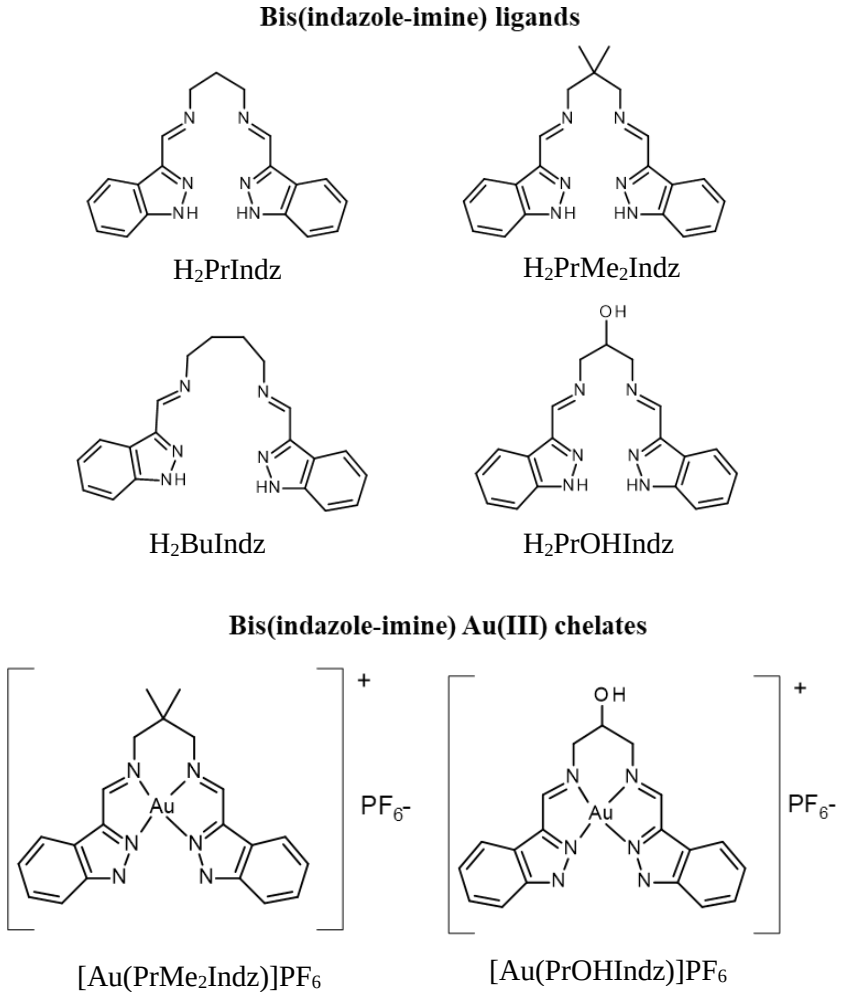

Figure 6.1. Bis(indazole-imine) ligands and Au(III) chelates synthesized in this work.

Both the ligands and metal chelates were characterized by NMR (^{1}H and ^{13}C), FTIR, UV-vis and MS. The ^{1}H and ^{13}C NMR spectra of the metal chelates showed an overall downfield shift compared to those of the ligands due to the Au(III) ion withdrawing electron density from the electron-rich ligands. Due to the deprotonation of the NH protons during metal coordination, the NH signals were absent in the ^{1}H NMR spectra of chelates.

The two Au(III) chelates were studied by X-ray crystallography. Both chelates had a d^8 electronic configuration and a square-planar geometry. The average Au-$N_{indazole}$ and Au-N_{imine} bond lengths were 1.99 Å and 2.01 Å, respectively while the average $N_{indazole}$-Au-$N_{indazole}$ and N_{imine}-Au-N_{imine} bond angle were 95.91° and, 103.47 ° respectively. Au-N_{imine} bond lengths appeared to be longer than the Au-$N_{indazole}$ bond lengths due to the indazole groups being anionic σ-donors with C-N-C bond angles that are more acute than the C=N-C bond angle of the imine group. Each chelate undergoes the π-stacking interactions with the adjacent molecule in the crystal lattice, indicating their potential as possible DNA intercalators.

Density functional theory (DFT) calculations were performed on two Au(III) chelates to determine their structural properties and to compare them to X-ray crystallography results. Gaussian 16W and the HSEHIPBE/SDD level of theory were used for DFT calculations. The simulations were carried out for geometry optimizations, electronic transitions, NMR spectral data as well as vibrational spectra. DFT simulations produced accurate results that correlated well with the experimental data.

Geometry optimization results showed a good correlation between the experimental and the calculated results. Comparison of the calculated and the experimental FTIR showed a good correlation between the two results although the frequencies of the calculated results were overestimated in general. The ^{1}H and ^{13}C NMR chemical shifts of the calculated data were underestimated overall. The calculated UV-vis spectra indicated an overall hypsochromic shift relative to the experimental spectrum.

Due to the design of the reported Au(III) chelates and their geometry being square-planar, the chelates were hypothesized to be intercalators meaning that they bind the DNA through π-π stacking interactions between DNA bases. Several DNA binding studies were conducted to determine the binding mode of the Au(III) chelates. These included gel electrophoresis, titration absorbance, and viscosity measurements.

Gel electrophoresis and absorption studies were consistent with each other and suggested a possibility of two binding modes which are intercalation and groove binding. Gel images showed a retarded mobility at 10 µM Au(III) chelate concentration, which shifted to a more advanced migration at 50 and 100 µM. this suggested intercalative binding at lower concentrations of added compound and groove binding at higher compound concentration. This is consistent with a broad Hill curve in the spectroscopic data. Some computational molecular docking data, however, will be required to confirm this. Viscosity measurements, however, suggested intercalation as the main binding mode. The replicates for viscosity measurements, however, were too few, to conclude that there is only one binding mode. In other words, the experiment did not go high enough in the mole ratio to reach the region where the viscosity begins to stop rising as groove binding becomes dominant. Hence it is not easy to confirm if there are one or two binding modes.

The Au(III) chelates were screened against two human breast cancer cell lines, MDA-MB-231 and MCF-7, and one normal human cell line, HEK-293. [Au($PrMe_2$Indz)]PF_6 proved to be more selective toward the two breast cancer cell lines than [Au(PrOHIndz)]PF_6. [Au(PrOHIndz)]PF_6, however, displayed greater cytotoxicity than cisplatin against both breast cancer cell lines. [Au($PrMe_2$Indz)]PF_6 exhibited higher cytotoxicity toward MDA-MB-231 than any other cell line; it can therefore be considered for a hit to lead compound optimization as a potential chemotherapeutic agent for triple-negative breast cancer (TNBC) cell lines.

As part of future work it will be necessary to establish new methods that will assist with the successful synthesis of the other two Au(III) chelates: [Au(PrIndz)]PF_6 and [Au(PrBuIndz)]PF_6. Either PF_6^- or Cl^- counterions will be suitable for the chelates. This will increase the library of bis(indazole-imine) Au(III) chelates. The chelates will have to be well characterized and the DNA binding mode, as well as cell cytotoxicity, be determined. It will also be handy to find ways to crystalized the ligands to determine their structural properties and be compared with DFT simulations.

The suggestion that there could be two DNA binding modes involved with the Au(III) chelates needs to be examined further to reach a firm conclusion. This can be achieved by exploring other DNA binding experiments like thermal melting and fluorescence titration. [Au($PrMe_2$Indz)]PF_6 displays selectivity towards MDA-MB-231 which means that it can be considered for a hit to lead compound optimization as a potential chemotherapeutic agent for triple-negative breast cancer (TNBC) cell lines.

The key strategy going forward will be to enhance the therapeutic index from ca. 2 to approximately 10–20. The structural modifications to the compound required to achieve this are, however, currently unknown and require numerous compound analogs to generate appropriate QSAR data to guide the process.

Appendices

Appendix A

NMR spectra of bis(indazole-imine) ligands and Au(III) chelates

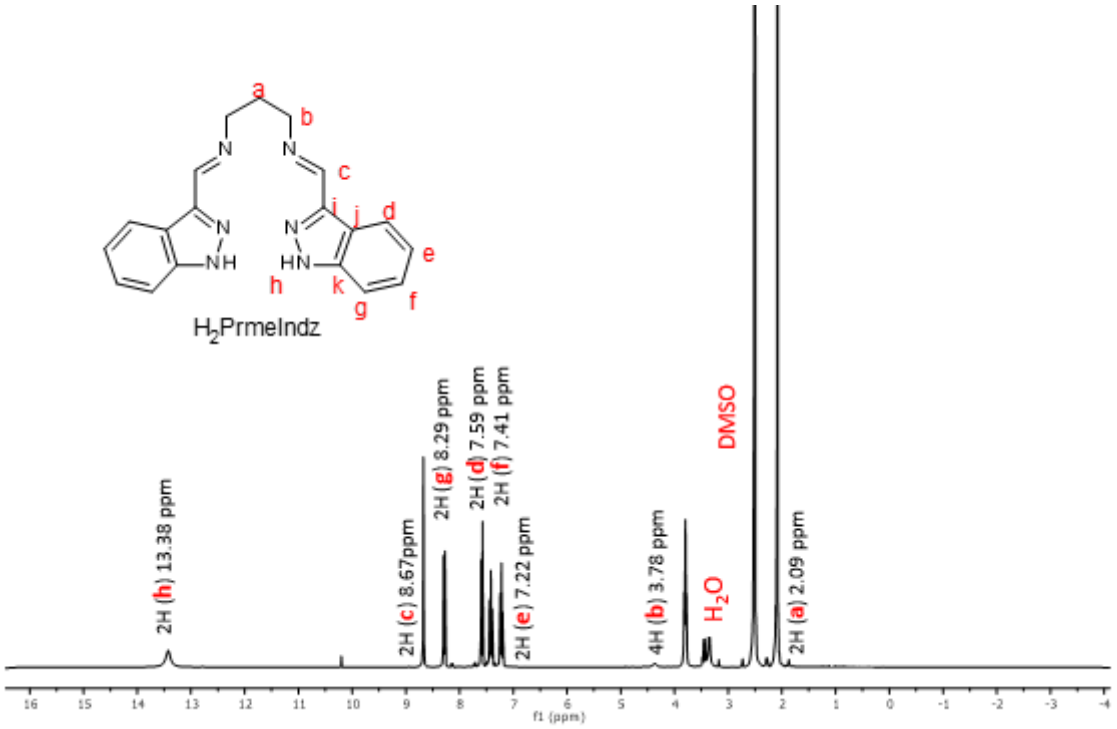

Figure A1: ^{1}H NMR spectrum of $H_2PrIndz$.

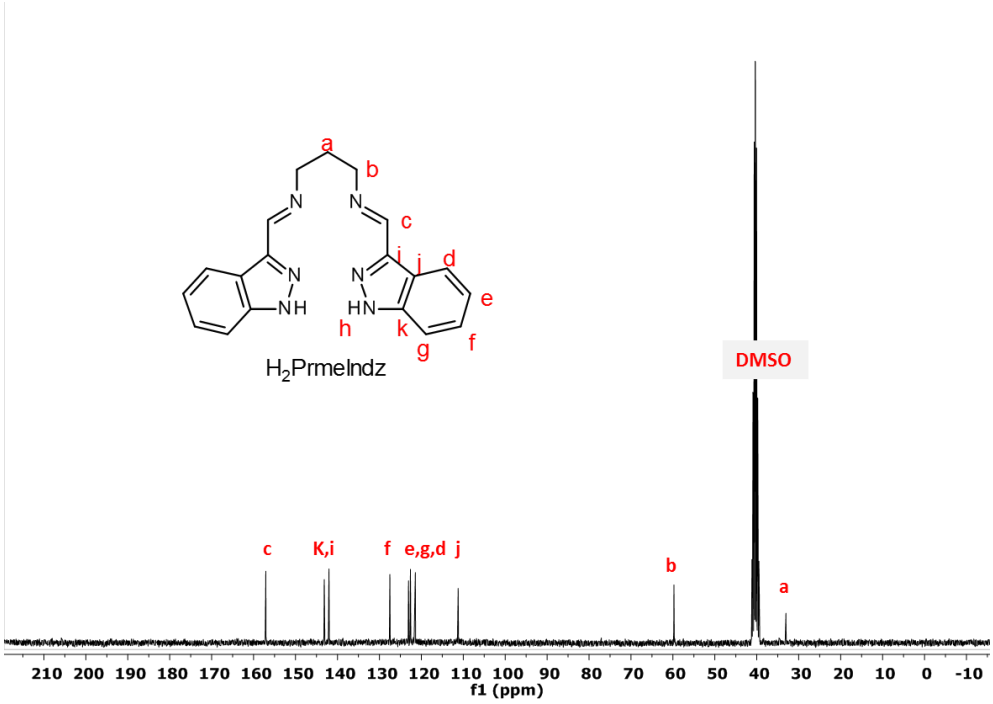

Figure A2: ^{13}C NMR spectrum of $H_2PrIndz$.

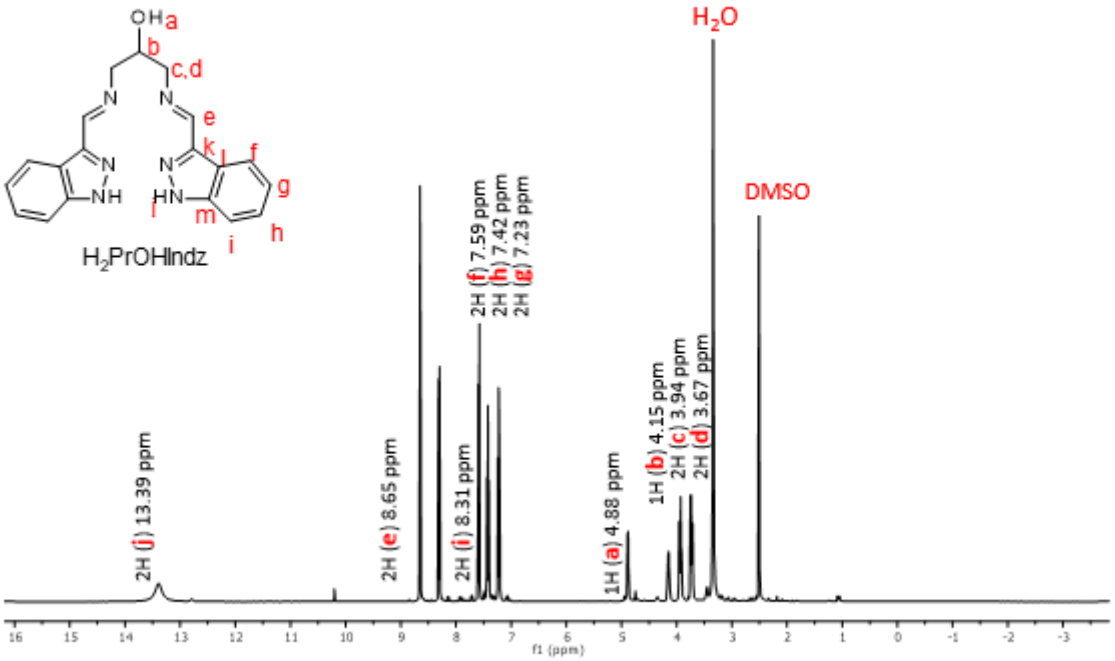

Figure A3: ^{1}H NMR spectrum of H_2PrOHIndz.

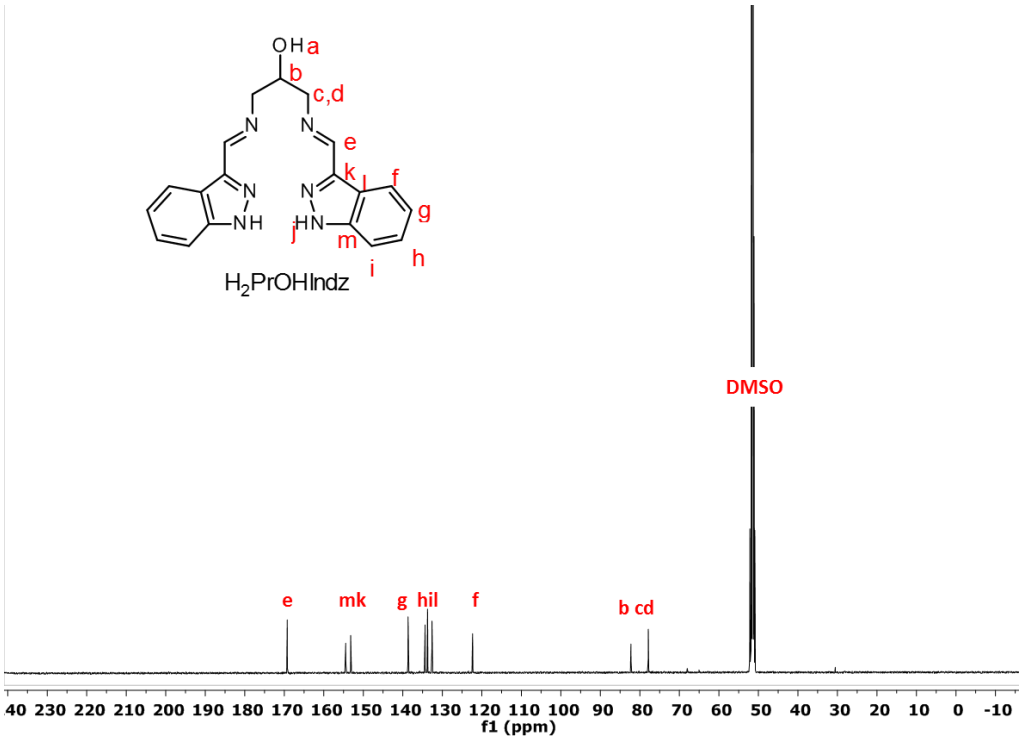

Figure A4: ^{13}C NMR spectrum of H_2PrOHIndz.

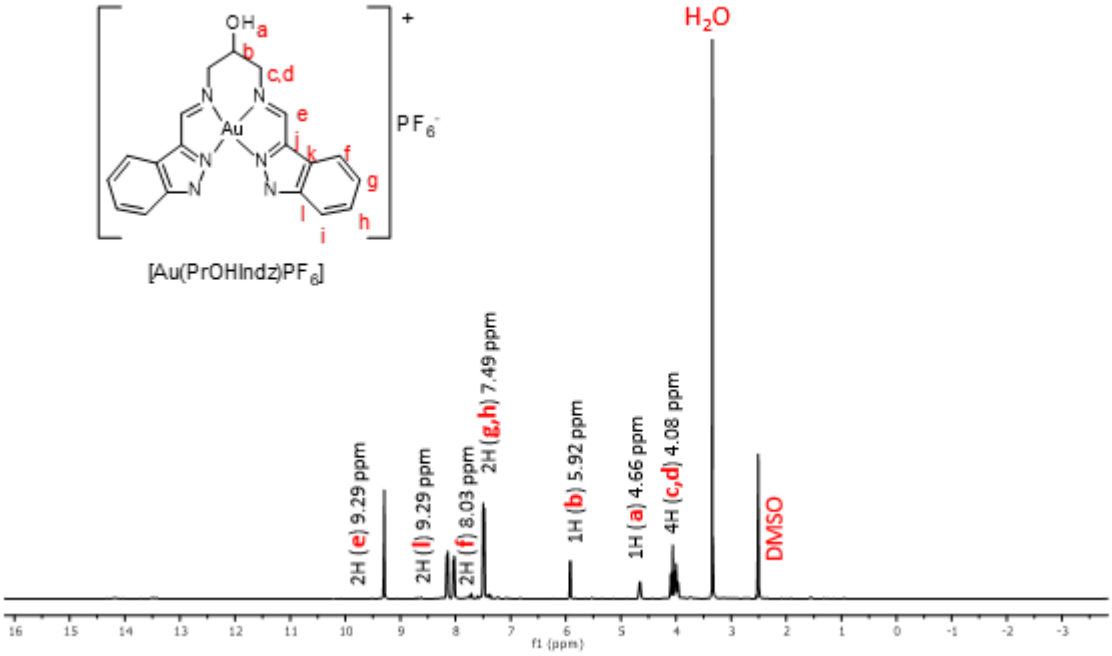

Figure A5: ^{1}H NMR spectrum of [Au(PrOHIndz)]PF_6.

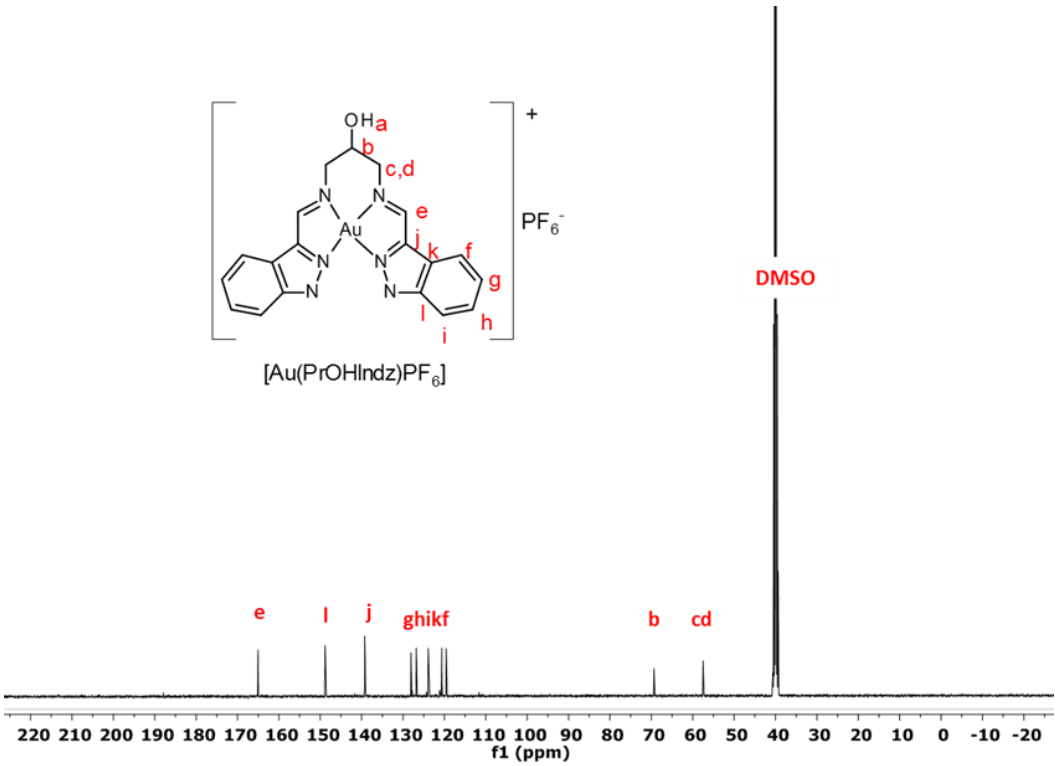

Figure A6: ^{13}C NMR spectrum of [Au(PrOHIndz)]PF_6.

Appendix B

Beer-Lambert law curves of bis(indazole-imine) ligands

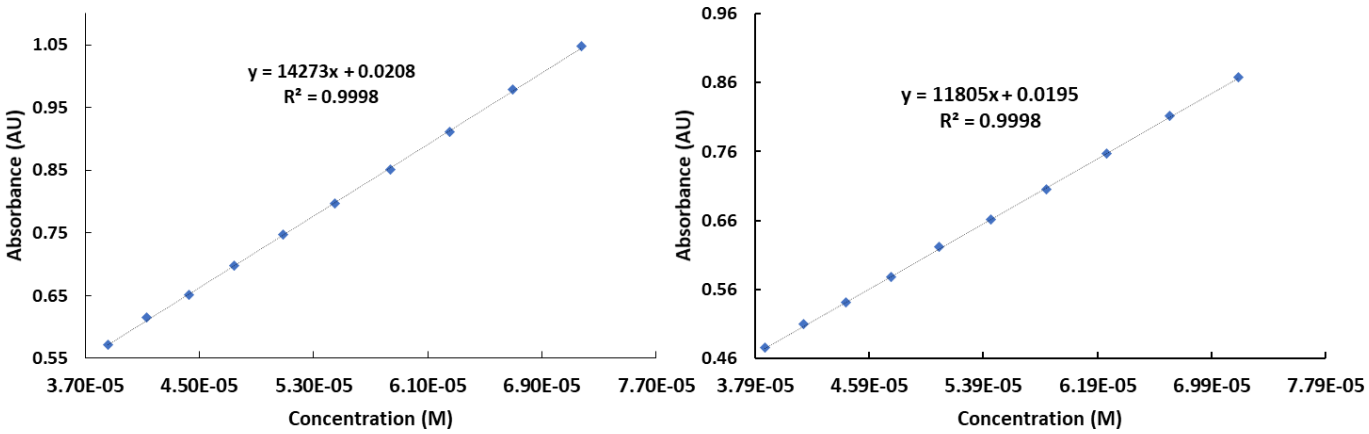

Figure B1: Beer-Lambert law curves for H_2PrIndz at 281nm (right) and 300 nm (left). R^2 gives the correlation coefficient while the slope affords the molar absorptivity constant.

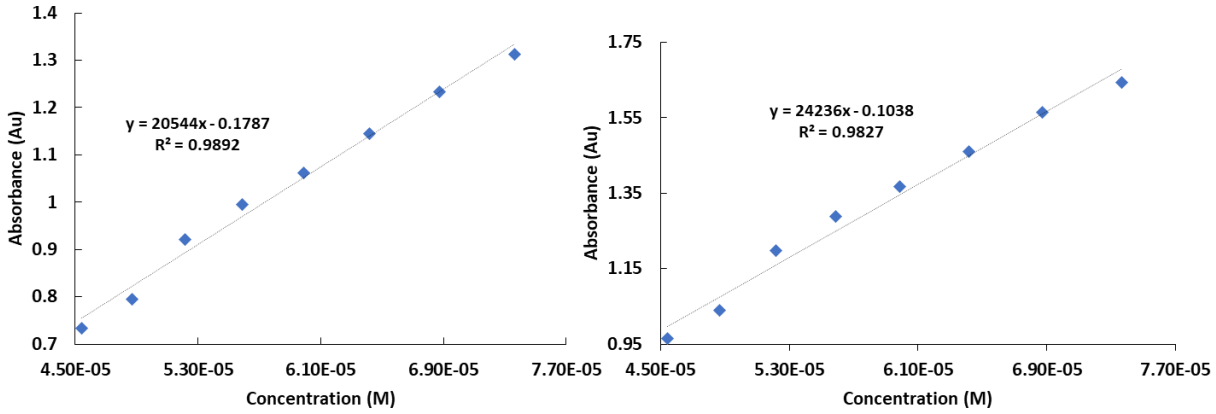

Figure B2: Beer-Lambert law curves for H_2PrMe$_2$Indz at 281nm (right) and 300 nm(left). R^2 gives the correlation coefficient while the slope affords the molar absorptivity constant.

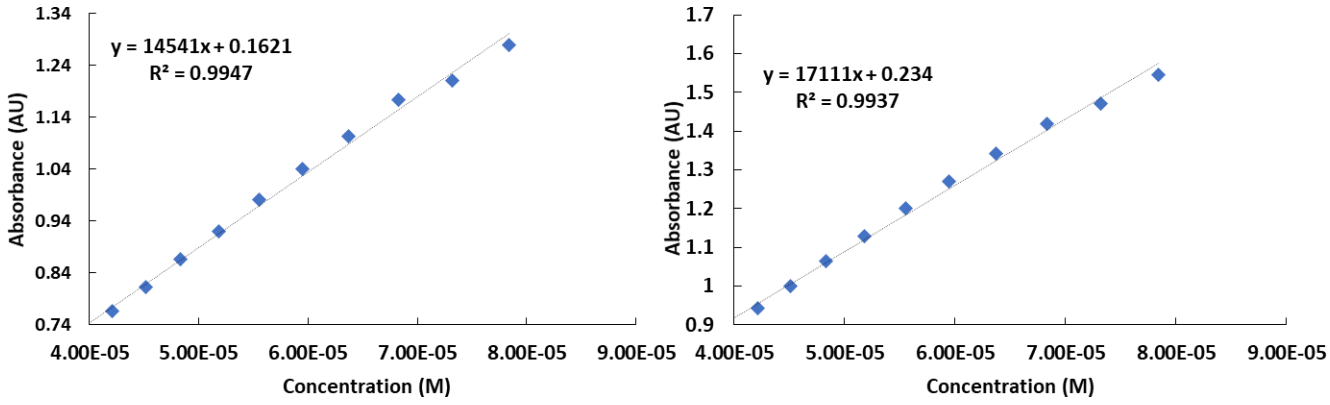

Figure B3: Beer-Lambert law curves for H_2BuIndz at 281 nm (right) and 300 nm (left). R^2 gives the correlation coefficient while the slope affords the molar absorptivity constant.

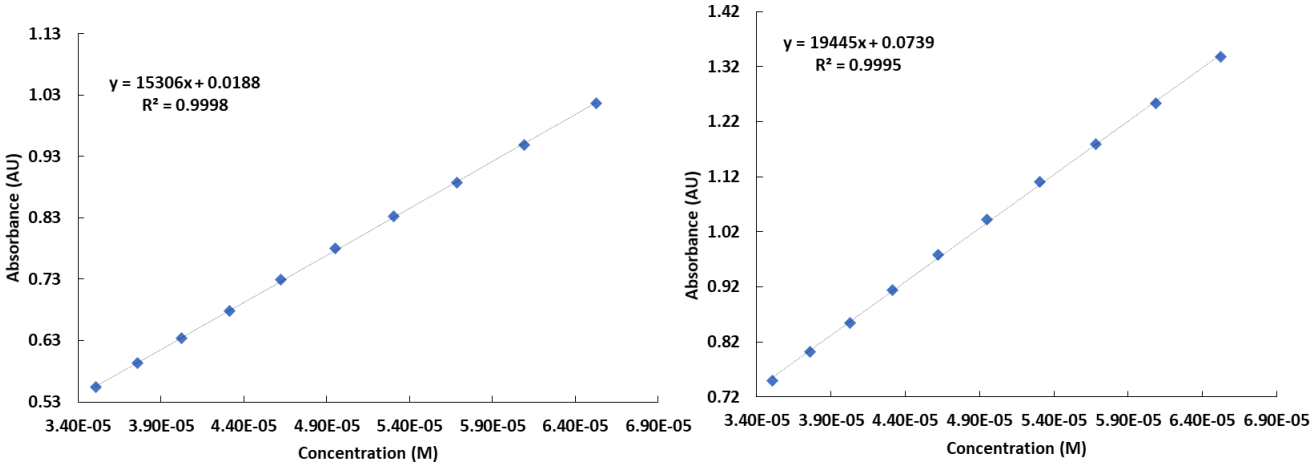

Figure B4: Beer-Lambert law curves for H2PrOHIndz at 280 nm (right) and 300 nm (left). R^2 gives the correlation coefficient while the slope affords the molar absorptivity constant.

Appendix C

Mass spectra of of bis(indazole-imine) ligands

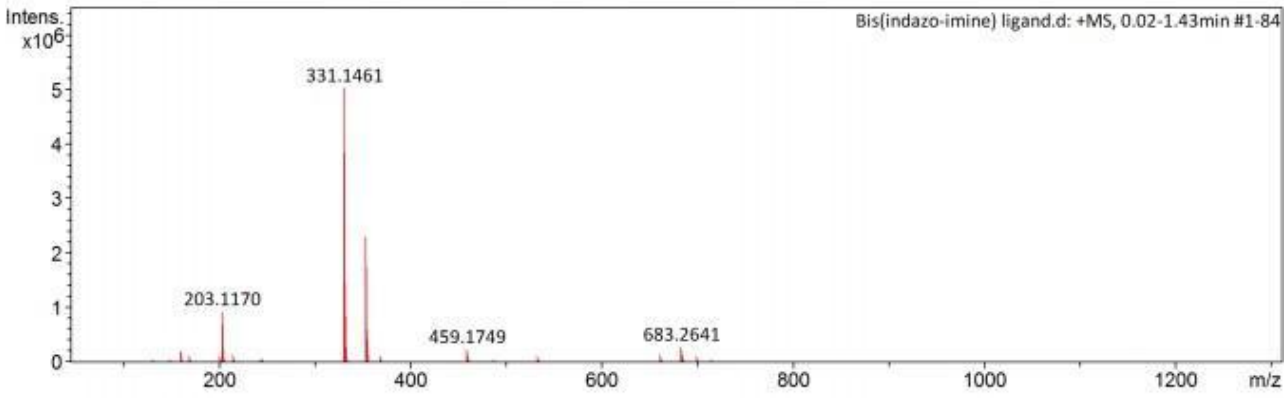

Figure C1: Mass spectrum of H_2PrIndz.

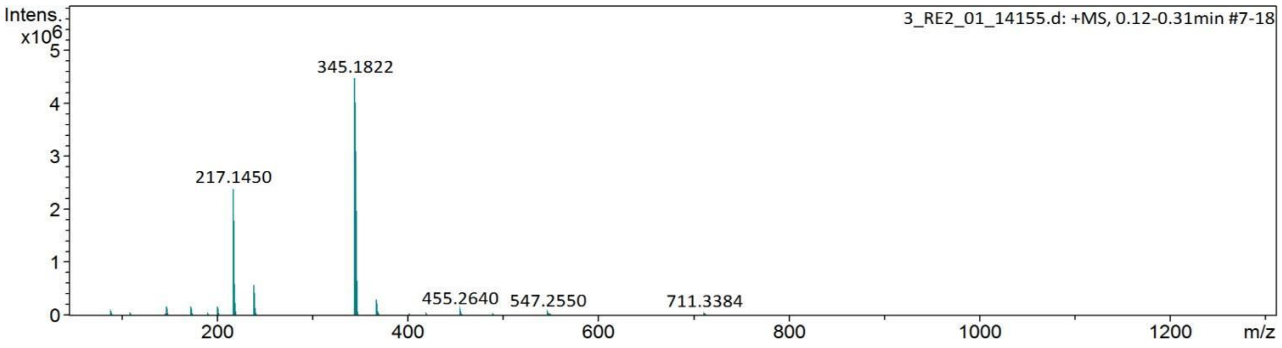

Figure C2: Mass spectrum of H_2BuIndz.

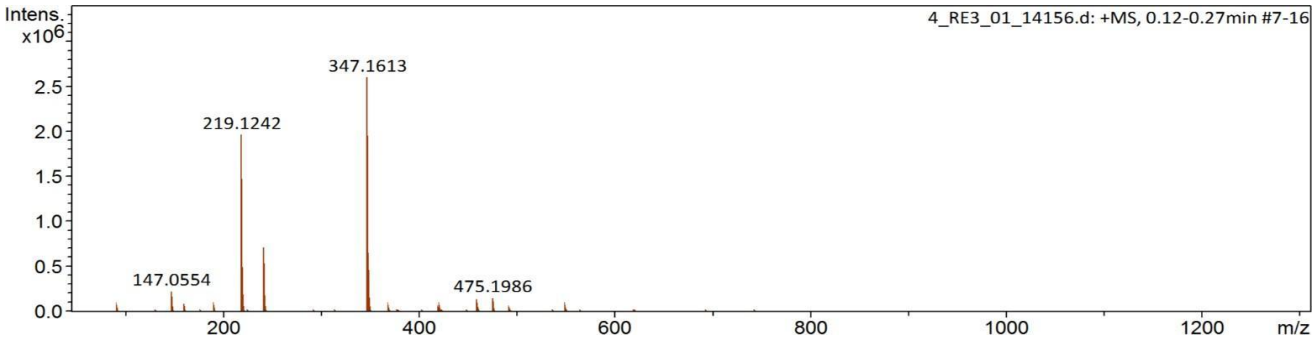

Figure C3: Mass spectrum of H_2PrOHIndz.

Appendix D

FTIR spectra of bis(indazole-imine) ligands and Au(III) chelates

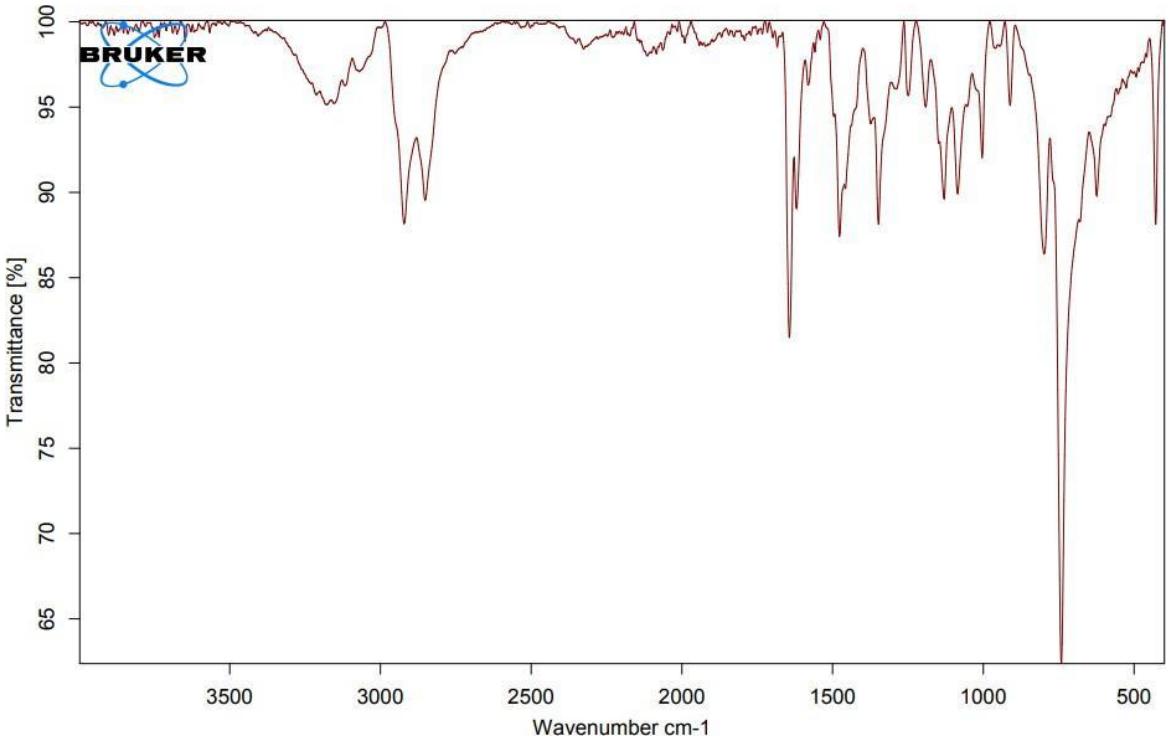

Figure D1: IR spectrum of H_2PrIndz.

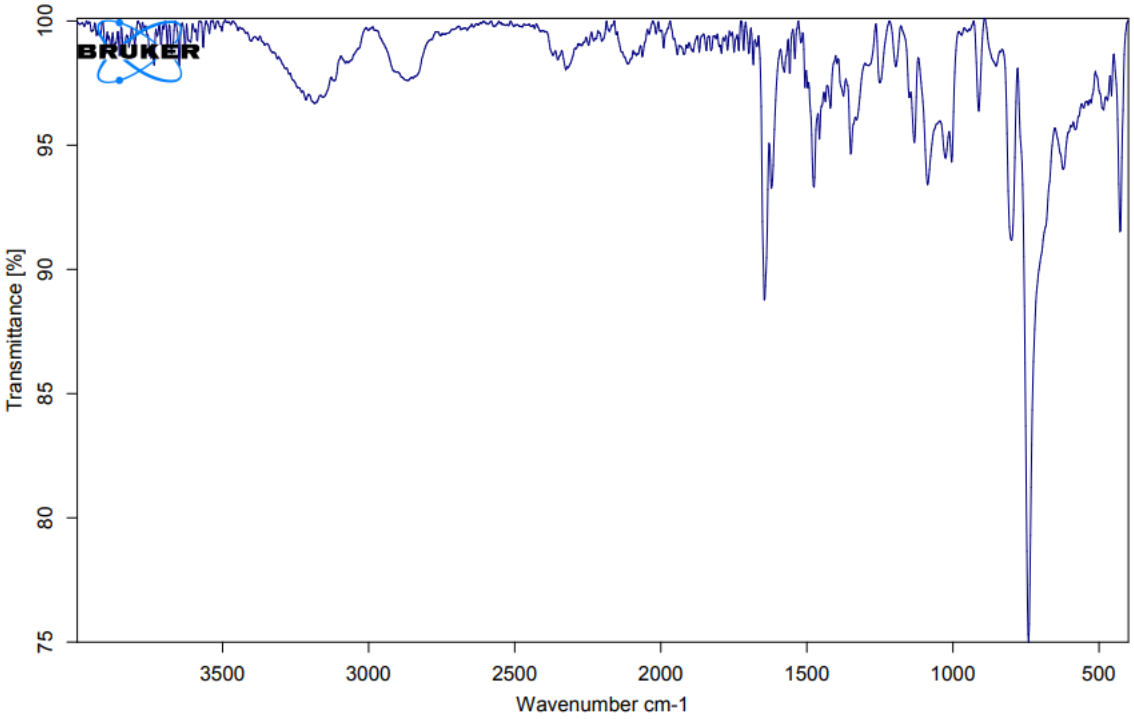

Figure D2: IR spectrum of H_2BuIndz.

Appendix E

DFT-calculated data for [Au(PrOHIndz)]PF_6

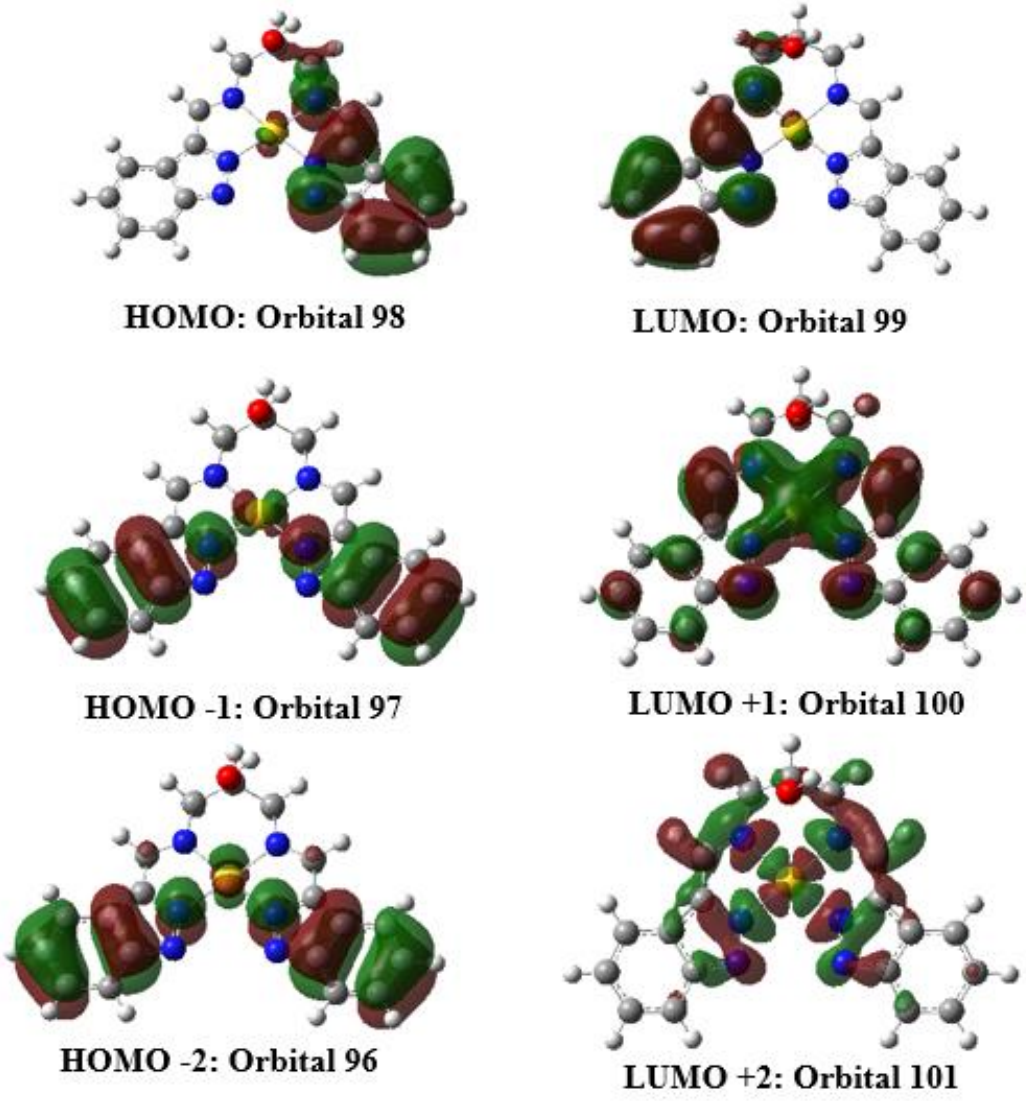

Figure E1: Image displaying molecular orbitals involved in most of the electronic transitions of [Au(PrOHIndz)]PF_6.

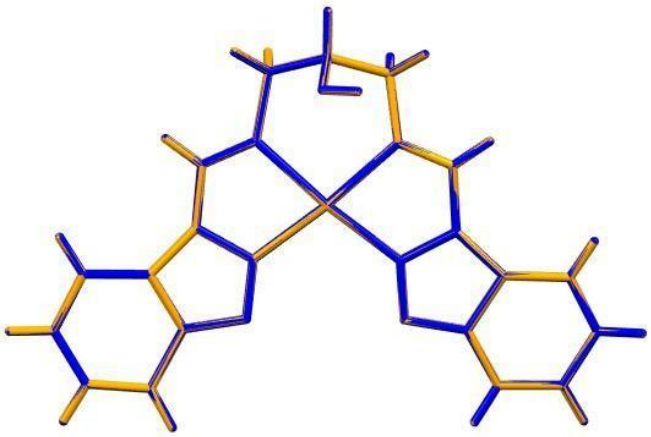

RMSD = 0.0012 Å

Figure E2: The least-square fit for the DFT-calculated structure (orange) and the X-ray structure (blue) of [Au(PrOHIndz)]PF_6.

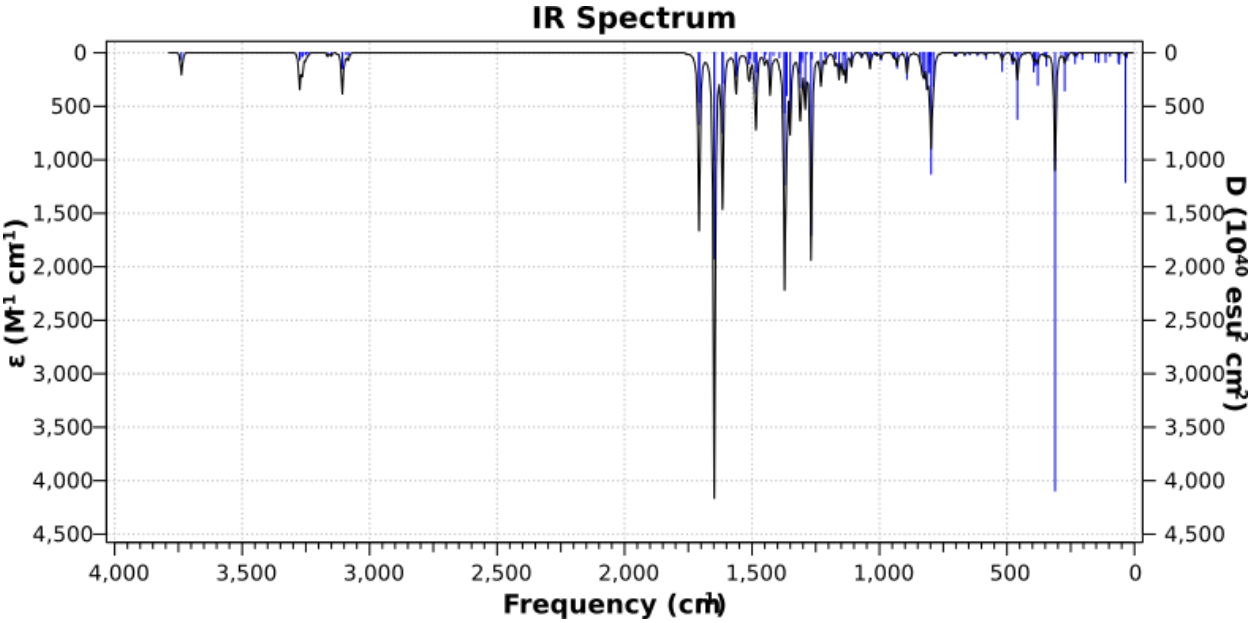

Figure E3: DFT-calculated IR spectrum of [Au(PrOHIndz)]PF_6.

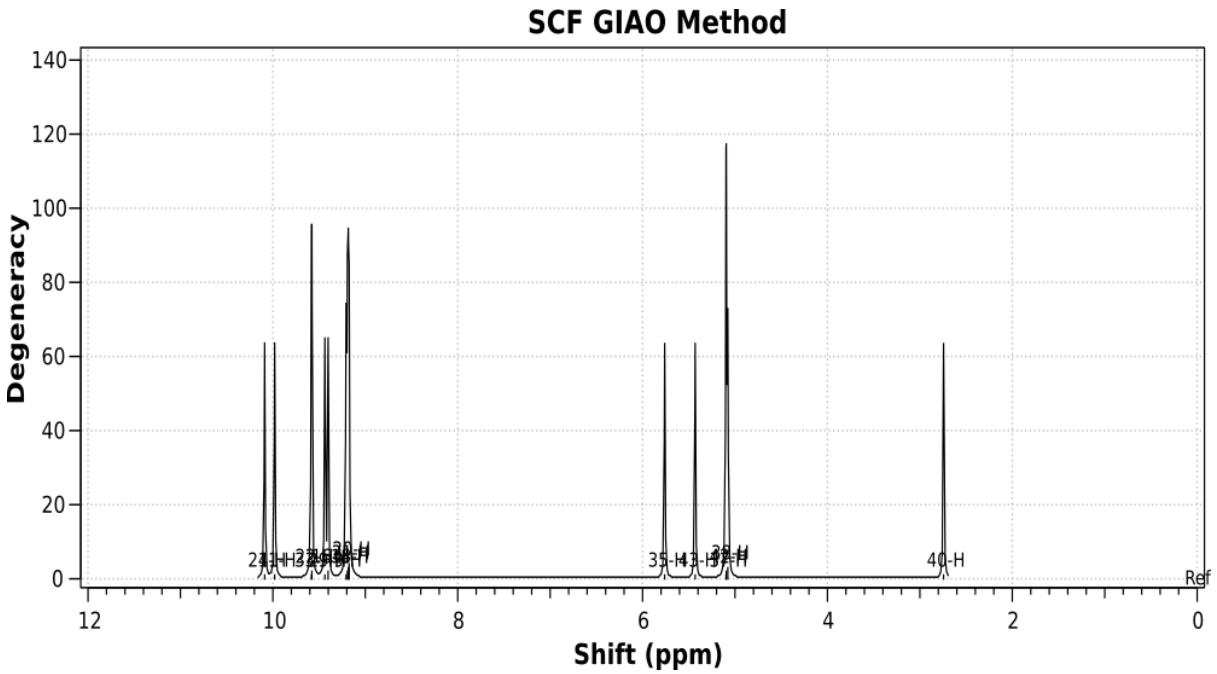

Figure E4: DFT-calculated ^{1}H NMR spectrum of [Au(PrOHIndz)]PF_6.

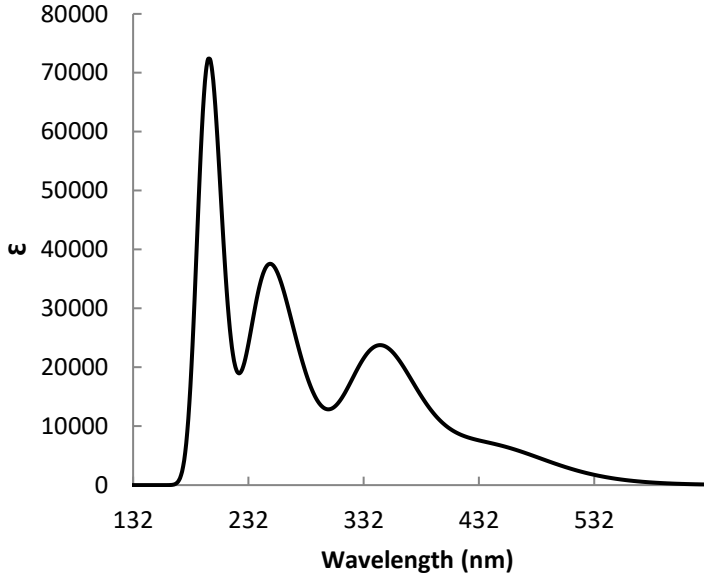

Figure E5: DFT-calculated UV-vis spectrum of [Au(PrOHIndz)]PF_6.

Appendix F

Biological data for [Au(PrOHIndz)]PF_6

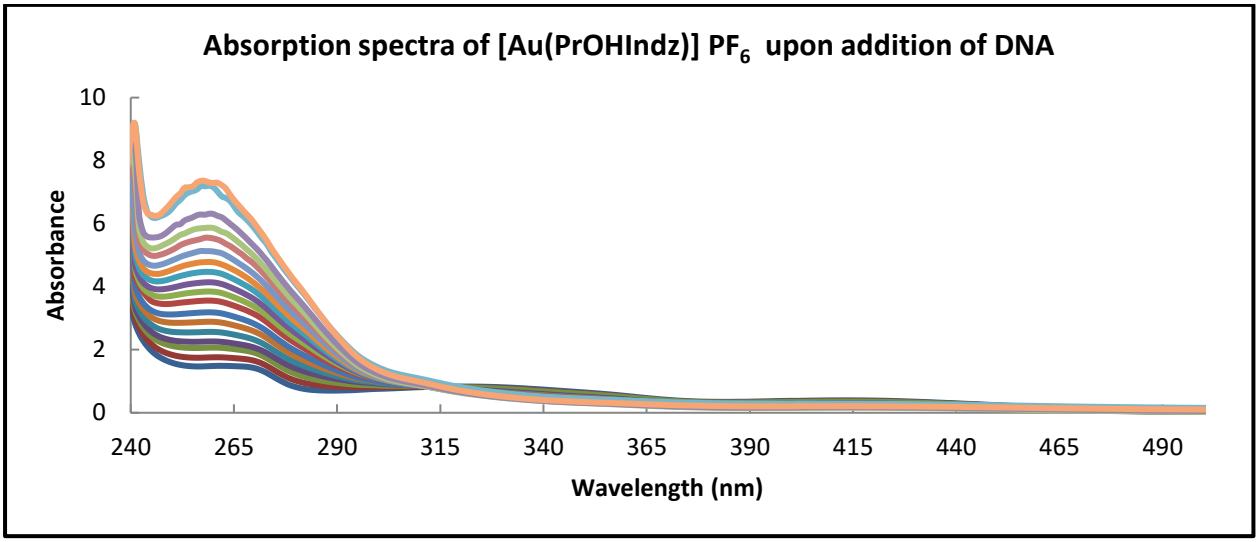

Figure F1: Sequential absorption spectra of [Au($PrMe_2$Indz)]PF_6 in the presence and absence of ctDNA. The experiment was performed in 0.100 M pH 7.0 TRIS-HCl Buffer with 10% DMSO at 37 °C.

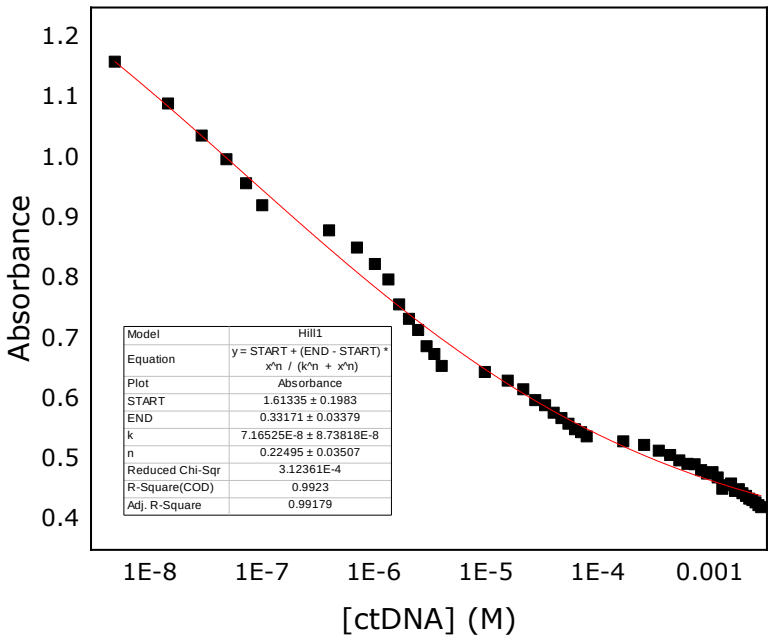

Figure F2: Non-linear least-squares fit of the Hill function to the spectroscopic data at 333 nm for the titration of [Au(PrOHIndz)]PF_6 with ctDNA at 37 °C.